

POLITECNICO DI MILANO

Scuola di Ingegneria dell'Informazione



POLO TERRITORIALE DI COMO

Master of Science in Computer Engineering

**IDENTIFICATION OF A MIMO
SYSTEM FOR ACTIVE VIBRATION
CONTROL IN HELICOPTERS**

Supervisor:

Prof. Luigi Piroddi

Assistant supervisors:

Prof. Marco Lovera

Prof. Gianluca Ghiringhelli

Master thesis by:

Francesco Boi

Student Id: 781719

Academic Year: 2014/2015

POLITECNICO DI MILANO
Scuola di Ingegneria dell'Informazione



POLO TERRITORIALE DI COMO

Corso di Laurea Magistrale in Ingegneria Informatica

**IDENTIFICAZIONE DI UN SISTEMA
MIMO PER IL CONTROLLO
ATTIVO DELLE VIBRAZIONI NEGLI
ELICOTTERI**

Relatore:

Prof. Luigi Piroddi

Correlatori:

Prof. Marco Lovera

Prof. Gianluca Ghiringhelli

Tesi specialistica di:

Francesco Boi

Matricola: 781719

Anno Accademico: 2014/2015

To my family.

Sommario

L'obiettivo principale di questo lavoro di tesi è stato l'identificazione un modello MIMO della risposta alle vibrazioni di una cabina di elicottero. Il modello stimato verrà utilizzato per progettare un sistema di controllo attivo delle vibrazioni per l'attenuazione del disturbo generato dal rotore principale. Il sistema da identificare è costituito da una serie di attuatori e accelerometri posizionati nella fusoliera di un elicottero Agusta A109.

Degli esperimenti sono stati eseguiti eccitando un singolo attuatore e registrando le risposte dei sensori alle vibrazioni generate. Da questi dati, tramite un algoritmo di identificazione a sottospazi il modello è stato identificato. La capacità del modello di riprodurre i segnali di output partendo dal segnale di eccitazione è stata testata. Il modello ha prodotto buoni risultati per attuatori e sensori posizionati dallo stesso lato dell'elicottero. Le performance sono invece meno buone considerando attuatori e accelerometri su lati opposti, a causa della maggiore attenuazione a cui i segnali sono soggetti. Paragonando le risposte in frequenza del modello con quelle calcolate dai dati si è notata una maggiore accuratezza del modello per alte frequenze.

Nonostante il progetto del sistema di controllo vada oltre gli obiettivi preposti, tale problema è stato indagato considerando una classica configurazione in retroazione. Per semplificare il problema del controllo, un disaccoppiatore SVD è stato utilizzato in modo da ottenere un numero di sistemi SISO indipendenti. In questo modo un sistema di controllo può essere progettato per ciascuna componente frequenziale del disturbo. Sul sistema semplificato l'algoritmo Higher Harmonic Control (HHC) è stato applicato. Alcune simulazioni sono state effettuate su un piccolo sottosistema per validare il sistema di controllo considerato: queste hanno mostrato una buona attenuazione del disturbo nonostante le inaccurately del modello. I risultati ottenuti insieme alla sua semplicità e facilità di implementazione, sembrano validare questa tecnica come una valida alternativa per il controllo attivo delle vibrazioni negli elicotteri.

Abstract

In this thesis the identification of a MIMO model of the vibration response of a helicopter cabin was carried out. The estimated model will be used to design an active vibration control system to reduce the vibrations generated by the main rotor. The system to be identified consists of a set of piezoelectric actuators and accelerometers located on a fuselage of an A109 Agusta helicopter.

First, a set of experiments was performed where each actuator was individually excited and the responses of the sensors to the induced vibrations were recorded. Using the recorded data, a subspace identification algorithm was employed to identify the model of interest.

To test the model, we passed the recorded input to the model and evaluated its ability to reproduce the recorded output. The model produced a good performance, especially when actuators and sensors were positioned on the same side of the helicopter. The model's performance deteriorated when actuators and sensors were located on opposite sides of the helicopters, due to the larger attenuation the signals are subject to. Additionally, the frequency responses of the model were compared to the ones calculated from the recorded data. The results showed that the model is more accurate for high frequencies.

Although a full scale control system goes beyond the scope of this work, a feedback control system has been proposed, based on the estimated model. Using an SVD decoupler, the MIMO system can be reduced to a set of independent SISO systems. This allowed creating a simple control system capable of attenuating individual frequency components using the appropriate subset of sensors and actuators. This simplified system was controlled by the Harmonic Control (HHC) algorithm. To validate the control system, some software simulations were performed on a subset of channels. The results showed a significant disturbance attenuation despite the inaccuracies of the model. These results, together with the simplicity and ease of implementation, indicate that this method provides a valid option for vibration reduction techniques.

Acknowledgements

Foremost, I would like to express my sincere gratitude to Prof. Luigi Piroddi and Prof. Marco Lovera for the continuous support during this study, for the patience they showed and their precious guidance, and to Prof. Gianluca Ghiringhelli for his important contribution to this work.

I would like to thank Edoardo Vigoni for his important assistance and all the other people at the Laboratory of the Department of Aerospace Engineering for their technical support.

Special thanks go to my mother, my father and my brother for all the support.

Contents

1	Introduction and motivations	19
1.1	Background	19
1.2	Sources of vibrations in helicopters	20
1.3	Review of vibration reduction techniques	21
1.3.1	Passive vibration control techniques	21
1.3.2	Active vibration control techniques	22
1.3.2.1	Higher Harmonic Control System	22
1.3.2.2	Individual Blade Control	22
1.3.2.3	Active Control of structural response	24
1.4	State of the art	24
1.5	Friendcopter project	26
1.5.1	Description of the set-up	26
1.5.2	Choice of actuators and their location	27
1.5.3	Choice of sensors and their location	29
1.5.4	Disturbance frequencies	29
1.5.5	Type of control	30
1.6	Current project description	30
1.6.1	Acquisition system	32
1.6.2	Problem statement and objective of the work	32
2	Subspace model identification	33
2.1	Reachability and Observability matrices	33
2.2	Realization problem	34
2.2.1	Data matrices	34
2.2.2	LQ decomposition	37
2.2.3	MOESP algorithm	37
2.2.4	SVD and additive white noise	40
2.3	PI-MOESP algorithm	41

CONTENTS

2.4	PO-MOESP algorithm	43
2.5	N4SID algorithm	45
2.6	Implementation of subspace identification algorithms in Matlab . . .	49
2.6.1	System Identification Toolbox	49
2.6.2	SMI Toolbox	49
3	Estimation of the model	51
3.1	Excitation signals	51
3.2	Analysis of the data	52
3.3	SISO models identified with the SMI Toolbox	54
3.3.1	Selection of the model order	54
3.3.2	Poles of the models	56
3.3.3	Frequency response	59
3.4	Identification of the global model	60
3.5	Identification of the global model with normalized measurements . . .	64
3.6	Identification of the global model with filtered data	67
3.7	Comparison between the frequency responses of the global models . .	70
4	Control design	73
4.1	Definition of a controller	73
4.1.1	Feedforward versus feedback disturbance attenuation	74
4.1.2	Centralized versus decentralized control	77
4.2	Diagonalization	77
4.2.1	Relative Gain Array	78
4.2.2	Singular Values Decomposition	79
4.3	Decoupler	80
4.3.1	SVD decoupling and control	82
4.4	Higher Harmonic Control Algorithm	83
4.5	Modified HHC algorithm	86
4.6	Simulation of the control technique on a small subsystem	88
4.6.1	First simulation: influence of the R weighting matrix	89
4.6.2	Second simulation	91
4.6.3	Third simulation	92
4.7	Comments on the results	94
5	Conclusions	95
5.1	Comments on the models estimated	95
5.2	Comments on the control system	96
5.3	Further developments	97

CONTENTS

Appendices	99
A Numerical results of the global model	100
B Numerical results of the model identified with normalized measurements	103
C Numerical results of the model identified with filtered data	106
Bibliography	109

Nomenclature

A1, ..., A18: Eighteen accelerometers placed inside the fuselage

ACSR: Active Control of Structural Response

AD01, ..., AD08: Eight actuators on the right rear strut

AS01, ..., AS08: Eight actuators on the left rear strut

DRGA: Dynamic Relative Gain Array

HHC: Higher Harmonic Control

IBC: Individual Blade Control

LTI: Linear Time Invariant

MIMO: Multi Input Multi Output

MOESP: Multivariable Output Error State Space algorithm

NSRGA: Non-Squared Relative Gain Array

PI-MOESP: Past Input Instrumental Variable MOESP algorithm

PI-MOESP: Past Output Instrumental Variable MOESP algorithm

RGA: Relative Gain Array

SISO: Single Input Single Output

SVD: Singular Values Decomposition

TD01, ..., TD12: Twelve actuators on the right wing of the anti-torque plate

TS01, ..., TS12: Twelve actuators on the side wing of the anti-torque plate

CONTENTS

vaf: Variance accounted for

List of Tables

1.1	Table of the accelerometer sensitivities	31
A.1	Simulation results of the global model for the actuators on the left rear strut in terms of the <i>vaf</i> criterion	100
A.2	Simulation results of the global model for the left actuators on the anti-torque plate in terms of the <i>vaf</i> criterion	101
A.3	Simulation results of the global model for the actuators on the right rear strut in terms of the <i>vaf</i> criterion	101
A.4	Simulation results of the global model for the right actuators on the anti-torque plate in terms of the <i>vaf</i> criterion	102
B.1	Simulation results of the scaled global model for the actuators on the left rear strut in terms of the <i>vaf</i> criterion	103
B.2	Simulation results of the scaled global model for the left actuators on the anti-torque plate in terms of the <i>vaf</i> criterion	104
B.3	Simulation results of the scaled global model for the actuators on the right rear strut in terms of <i>vaf</i> criterion	104
B.4	Simulation results of the scaled global model for the right actuators on the anti-torque plate in terms of the <i>vaf</i> criterion	105
C.1	Simulation results of the scaled and filtered global model for the actuators on the left rear strut in terms of the <i>vaf</i> criterion	106
C.2	Simulation results of the scaled and filtered global model for the left actuators on the anti-torque plate in terms of the <i>vaf</i> criterion	107
C.3	Simulation results of the scaled and filtered global model for the actuators on the right rear strut in terms of the <i>vaf</i> criterion	107
C.4	Simulation results of the scaled and filtered global model for the right actuators on the anti-torque plate in terms of the <i>vaf</i> criterion	108

List of Figures

1.1	Vibration profile of a helicopter as a function of cruise speed	20
1.2	Scheme of an HHC system	23
1.3	Scheme of an IBC system	24
1.4	Scheme of an ACSR system	25
1.5	Noise reduction at microphones during a flight test in the Sikorsky system	25
1.6	Helicopter fuselage employed during the <i>Friendcopter</i> project.	26
1.7	Aerodynamic brake	27
1.8	Example of an anti-torque plate.	27
1.9	Actuators location	28
1.10	Noise spectrum inside the cabin	29
1.11	Locations of the left accelerometers on the left side of the cabin	31
2.1	Plot of singular values in case of noisy measurements with a visible gap.	41
2.2	Plot of singular values in case of noisy measurements without a visible gap.	41
2.3	Output error identification scheme	42
2.4	Innovation model identification scheme	43
3.1	Data acquired at different sensors with the same actuator excited	52
3.2	Data acquired at the same sensors when different actuators are excited	53
3.3	Plot of singular values of a SISO model for order selection	54
3.4	Simulation errors in terms of the <i>vaf</i> criterion for the SISO models of the actuators on the right rear strut for varying model orders	55
3.5	Simulation errors in terms of the <i>vaf</i> criterion averaged on different models for varying model orders	56
3.6	Comparison between the frequency response of the SISO models and the frequency response calculated from the data	57
3.7	Poles of SISO models sharing the same outputs.	58

LIST OF FIGURES

3.8	Poles of SISO models sharing the same inputs.	58
3.9	Bode plots of SISO models with the same input and symmetric outputs	59
3.10	Plot of the singular values for the order selection of the global model	61
3.11	Simulation results of the global model for the actuators on the left rear strut in terms of the <i>vaf</i> criterion	62
3.12	Simulation results of the global model for the left actuators on the anti-torque plate in terms of the <i>vaf</i> criterion	62
3.13	Simulation results of the global model for the actuators on the right rear strut in terms of the <i>vaf</i> criterion	63
3.14	Simulation results of the global model for the right actuators on the anti-torque plate in terms of the <i>vaf</i> criterion	63
3.15	Simulation results of the scaled global model for the actuators on the left rear strut in terms of the <i>vaf</i> criterion	65
3.16	Simulation results of the scaled global model for the left actuators on the anti-torque plate in terms of the <i>vaf</i> criterion	65
3.17	Simulation results of the scaled global model for the actuators on the right rear strut in terms of the <i>vaf</i> criterion	66
3.18	Simulation results of the scaled global model for the right actuators on the anti-torque plate in terms of the <i>vaf</i> criterion	66
3.19	Frequency response of the filter used to filter the data	67
3.20	Simulation results of the scaled and filtered global model for the actuators on the left rear strut	68
3.21	Simulation results of the scaled and filtered global model for the left actuators of the anti-torque plate	68
3.22	Simulation results of the scaled and filtered global model for the actuators on the right rear strut	69
3.23	Simulation results of the scaled and filtered global model for the right actuators on the anti-torque plate	69
3.24	Comparison among the frequency responses of the global models and the corresponding SISO models	71
4.1	Example of a feedforward control scheme	74
4.2	FxLMS feedforward control scheme	75
4.3	General block diagram of a feedback system	76
4.4	Block diagram of the system with a decoupler	81
4.5	SVD expansion of the general feedback control scheme	82
4.6	Block diagram after the SVD simplification.	83
4.7	Result of the first control simulation at the accelerometer 3	90

LIST OF FIGURES

4.8	Result of the first control simulation at the accelerometer 11	91
4.9	Results of the second control simulation	92
4.10	Results of the third control simulation	93

Chapter 1

Introduction and motivations

A basic description of the vibrations in a helicopter is given in this chapter and some of the passive and active systems for vibration attenuation are discussed. The problem of vibration attenuation is then discussed, with reference to the system employed in this work.

1.1 Background

Helicopters play an essential role in today's society. Thanks to their peculiarities they are employed in several extreme conditions such as rescue operations, air medical services or military missions. However the high noise level produced is one of the most important factors affecting the passengers' and crew's comfort and can potentially compromise the success of the mission. In the helicopter cabin, the sound pressure level of the noise is on average from 20 to 30 dB higher than those of fixed wing aircrafts [7]. Moreover, the noise attenuation inside modern helicopter cabins is still unsatisfactory compared to modern commercial jet airplanes. In addition to this, the tonal components are typically in the frequency range between 500 Hz and 4500 Hz to which the human ear is most sensitive.

The high levels of vibrations are also responsible for the degradation of the structural integrity as well as an increase in the fatigue of the mechanical components of the helicopter and a reduction of the effectiveness of the on-board computer systems. All these aspects have as a further consequence the increase of the maintenance costs. Therefore, considerable efforts have been taken for the last few decades to reduce the level of noise and vibrations in helicopters.

1.2 Sources of vibrations in helicopters

Vibrations in the helicopter originate from the main rotor, the tail rotor, the engines and other machinery [14]. The main rotor, that generates the aerodynamic forces necessary to fly the aircraft, is rigidly mounted on the roof structure of the helicopter via connecting members called struts through which vibrations are transmitted to the cabin roof. The frequencies of the disturbance created by the main rotor are integer multiples of the rotor frequency. Main rotor vibrations arise especially in forward flight.

Another source of vibration is represented by the blades. They are a critical component of the helicopter and a major responsible of the vibrations produced, due to the particular aerodynamic loads they are subjected to.

The intensity of the vibrations also depends on the speed of the helicopter (a typical profile is shown in Figure 1.1). Severe vibrations occur in two distinct flight conditions:

- low speed transition flight: generally during the landing and taking off manoeuvres;
- high speed flight.

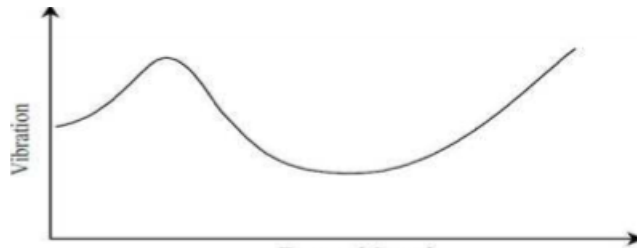


Figure 1.1: Vibration profile of a helicopter as a function of cruise speed.

At low speed, the severe vibration level is primarily due to abrupt changes in the blades' load. This happens when a rotor blade passes in close proximity of the vortices created by a previous blade. This condition is generally referred to as Blade Vortex Interaction (BVI). In moderate-to-high speed cruise, the BVI-induced vibration is reduced and the vibrations are caused mainly by the main rotor.

1.3 Review of vibration reduction techniques

A number of techniques have been developed to reduce noise and vibration inside helicopter cabins. They can be broadly divided into "passive" and "active" vibration control techniques. The main difference between the two categories is in the employment of active devices such as actuators and loudspeakers.

1.3.1 Passive vibration control techniques

A first approach, usually performed during the vehicle design phase, involves designing blades and fuselages in such a way that their natural vibration frequencies lie away from the rotor harmonic frequencies. This tuning helps avoiding blade and fuselage resonances with the rotor harmonics. This method, however, requires extensive modelling and testing of the blade and fuselage structural characteristics throughout the aircraft development phase [11].

Other passive techniques use mechanical components that absorb the energy of the vibrations, such as tuned-mass absorbers and tuned-mass dampers. A typical dynamic absorber is a single degree of freedom system with a relatively small mass on a spring. It is attached to a structure in order to reduce the dynamic response of the structure. The frequency of the absorber is tuned to a particular structural frequency so that when that frequency is excited, it will resonate out of phase with the structural motion. A tuned-damper works in a similar manner but it has as additional mechanical component a damper. With this technique, each mode of vibration requires a separate absorber. Vibration absorbers and dampers are tuned to the frequencies to be removed and are placed at specific locations in the fuselage.

Despite its simplicity, the reduction obtained with such methods is limited (both in the amount of energy absorption and frequency operation range) and involves an additional weight. Another drawback is that, due to their fixed design, tuned-mass absorbers and dampers are not able to adapt to operating condition changes [11].

Rotor isolation is another common vibration reduction technique. Isolating materials, such as pads of rubber or springs are placed between the vibrating system and its supporting structure to reduce the force transmitted from the vibrating system to the supporting structure.

Although tuned mass absorbers and isolators are passive devices, both can be implemented as semi-active systems as well. In both cases though, these vibration reduction techniques can only achieve local effects.

1.3.2 Active vibration control techniques

Active vibration reduction techniques were introduced to overcome the limitations imposed by passive control techniques and to increase the reduction of both noise and vibrations. A typical active noise and vibration control system consists of four main components: a set of sensors, a set of actuators, a power supply unit and a controller. The acoustic noise signals or vibrations are measured by the sensors mounted on the fuselage. The signals are processed by the controller and used to generate a signal to drive the actuators. The signal is used by the actuators to produce a vibration field as close as possible to the vibration field to be removed but opposite in phase, producing a destructive interference as result. A classification of the existing active methods can be carried out according to the actuators location:

- Higher Harmonic Control System (HHC)
- Individual Blade Control (IBC)
- Active Control of Structural Response (ACSR)

The HHC and IBC methods aim at attenuating the vibrations by means of actuators placed on the rotor. In this way, the vibrations are attenuated before they propagate to the fuselage. On the contrary, in the ACSR method, only the vibrations that are transmitted to the cabin are attenuated. All these systems rely on the Higher Harmonic Control algorithm that will be presented in Chapter 4 [2].

1.3.2.1 Higher Harmonic Control System

The higher harmonic control system aim at reducing the vibrations that affect the main rotor before they propagate to the cabin [6] [2]. Transducers are mounted at key locations in the fuselage to measure the residual vibrations while the actuators are typically mounted in the non-rotating swash plate. The actuators excite the blades in order to create blade oscillations which, when properly phased, reduce the vibrations induced by the rotor during flight conditions. Typical actuators for this system are hydraulic or electromagnetic actuators. A scheme of this type of systems is shown in Figure 1.2.

1.3.2.2 Individual Blade Control

The Individual blade control technique (IBC) is, in many aspects, similar to that of HHC, except that using different locations of the actuators are employed [2]. While the HHC technique uses actuators placed in the non-rotating frame, the IBC

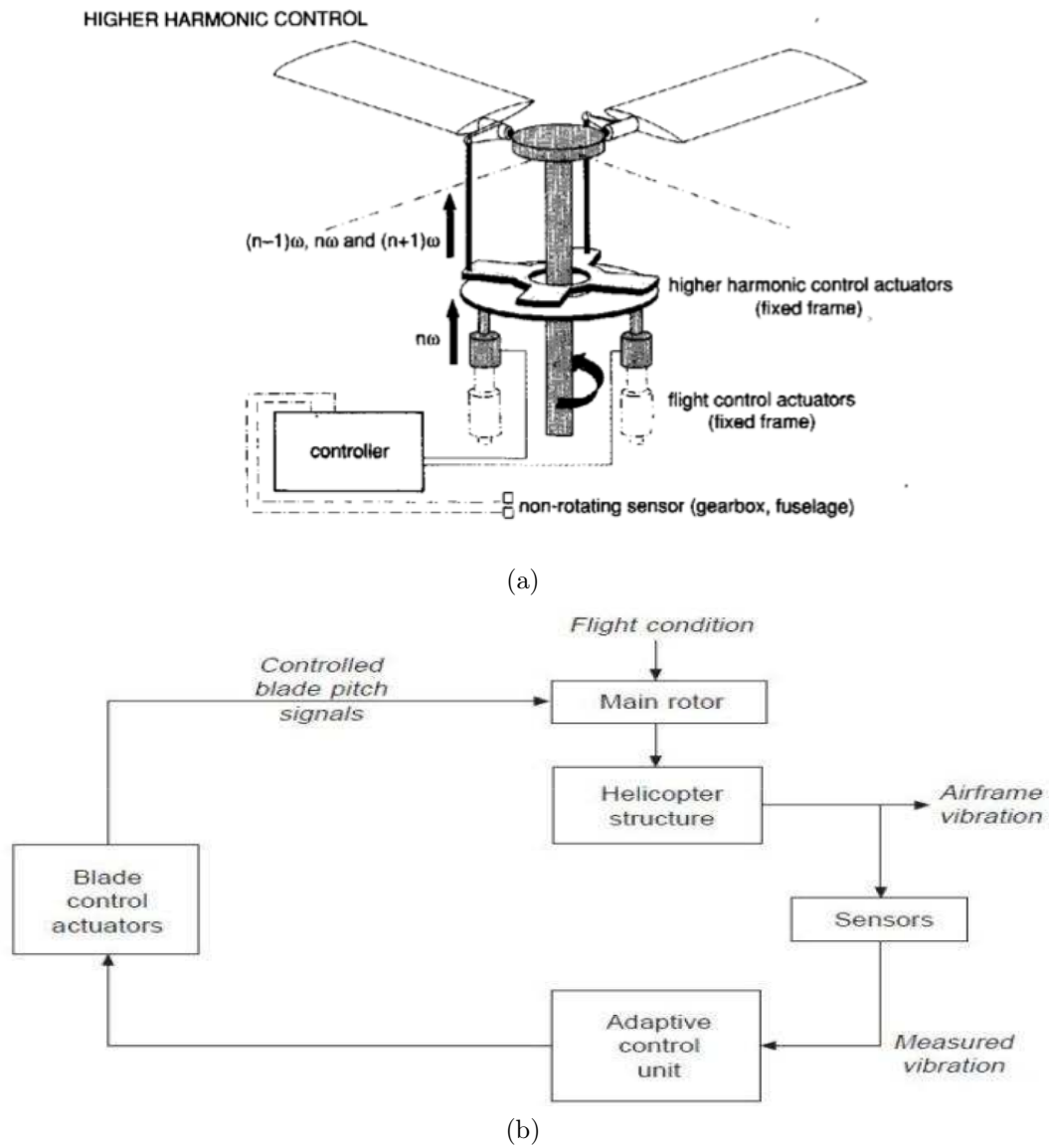


Figure 1.2: Scheme of an HHC system[6]

approach employs actuators located in the rotating frame, allowing to control each blade independently. A scheme of the IBC is shown in Figure 1.3. The actuators can be placed between the hub and the blades or directly on the blades, according to different implementation of the system.

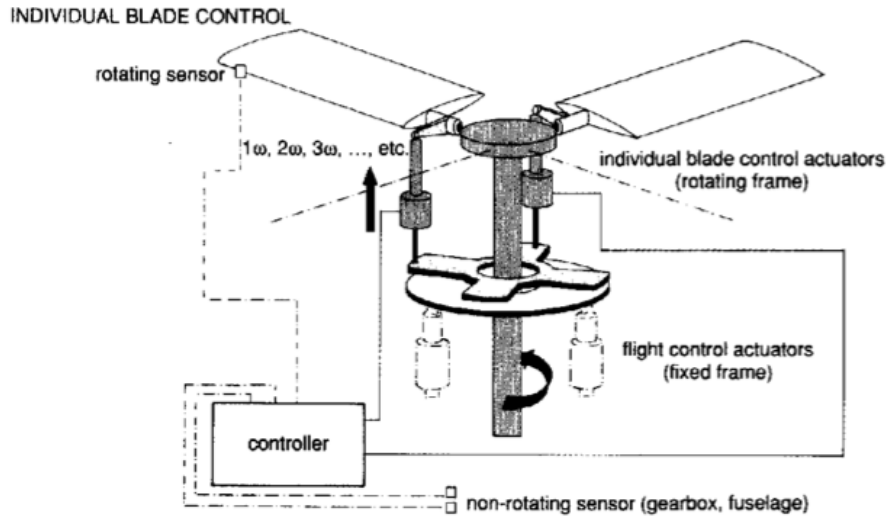


Figure 1.3: Scheme of an IBC system [6]

1.3.2.3 Active Control of structural response

Unlike the HHC and IBC techniques, that aim at achieving a global reduction of the vibration by placing the actuators in the rotor system, the ACSR approach, pioneered by Westland helicopters, is designed to attenuate the vibration in the fuselage. Currently, ACSR is one of the most successful helicopter vibration reduction methods. Vibration sensors are placed at key locations in the fuselage, where minimal vibration is desired (for example at the pilot and passenger seats). An ACSR controller uses the sensors' input to calculate the actuators' response needed to reduce the vibrations. Recently, the ACSR technology has been incorporated in modern production helicopters such as the Westland/Augusta AW101. A scheme of this technique is shown in Figure 1.4.

1.4 State of the art

Some control systems have already been implemented in helicopters showing good results also during in-flight tests. An example is given in [16] where a system aimed at attenuating the primary gear-mesh tone is presented. In that work a set of proof-mass actuators and microphones were used. The algorithm used to drive the actuators was the HHC algorithm (discussed in Chapter 4). The results are presented

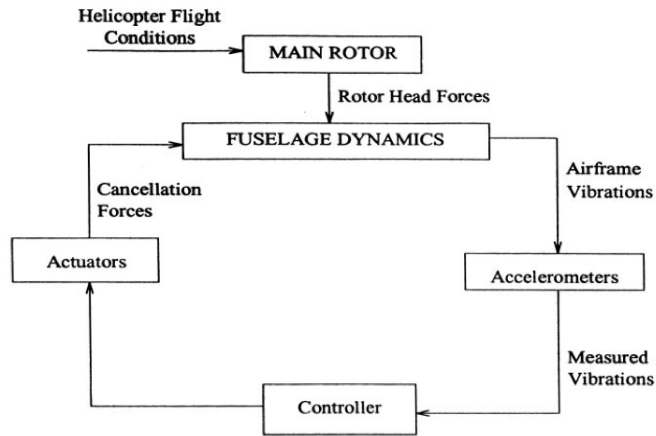


Figure 1.4: Scheme of an ACSR system [4]

in Figure 1.5 showing a significant noise attenuation for a system mounted on a S-76 helicopter.

Helicopters implementing active noise/vibration control are already commercially available. Some of these are the S-76C++ and the S-76D of S-76 Sikorsky series. Notably, the latter has a vibration control system that attenuates the perceived noise level not only in the cabin but also externally.

Another example of commercial implementation of active control systems is given by the AW101 helicopter of the Agusta-Westland. This helicopter, designed for military, maritime and civil roles, implements an ACSR vibration control system.

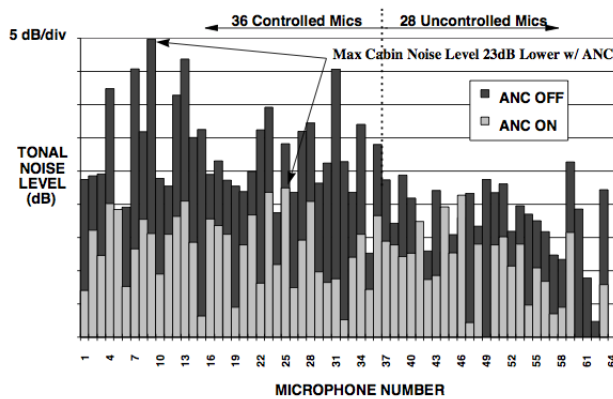


Figure 1.5: Gear-mesh reductions at microphones during the second flight test in [16].

1.5 Friendcopter project

An attempt to design an active control system for noise reduction in a helicopter cabin was performed also by the Aerospace Department of Politecnico di Milano. In this project, named *Friendcopter*, the following set-up was used.

1.5.1 Description of the set-up



Figure 1.6: Helicopter fuselage employed during the *Friendcopter* project.

The set-up present in the aerospace engineering laboratory shown in Figure 1.6 is an actual fuselage of an Agusta A109 helicopter, lacking of many devices (e.g. the blades, the tail rotors, pumps, internal equipments, etc.) but equipped with the main components of the main rotor and structural links. To have a more realistic situation, more similar to the on-flight conditions, an aerodynamic brake (shown in Figure 1.7) was mounted [17].

Some of the omitted devices (e.g. pumps, tail rotor) are also sources of noise. However, the current set-up allows to reproduce the common disturbance tones generated by the main rotor gearbox [17]. The gearbox is connected to the fuselage with a set of rigid struts and an aluminium anti-torque plate mounted above the cabin roof. In this way all the loads generated by the rotor are transmitted to the anti-torque plate instead of the struts. A typical shape of the anti-torque plate is shown in Figure 1.8. The generated vibrations are transmitted to the fuselage mainly through the anti-torque plate and the rear struts.

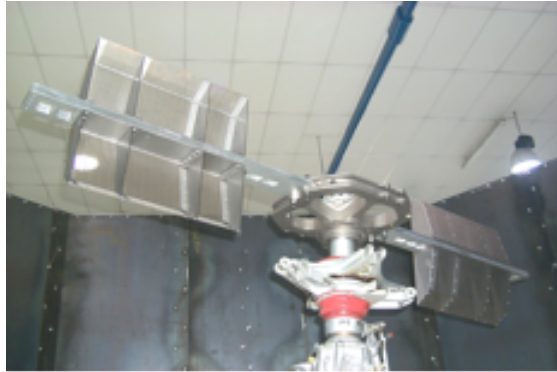


Figure 1.7: Aerodynamic brake.

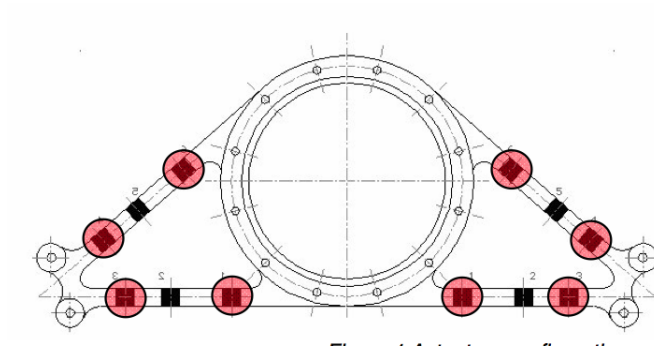
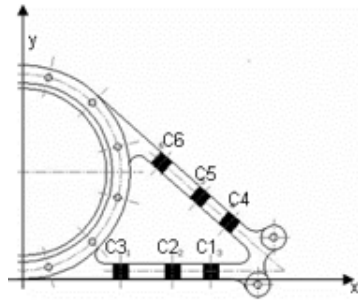


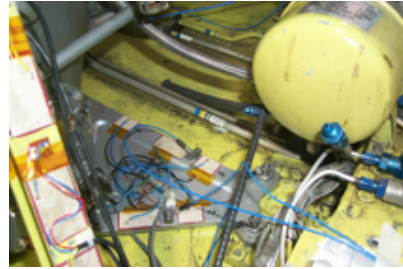
Figure 1.8: Example of an anti-torque plate.

1.5.2 Choice of actuators and their location

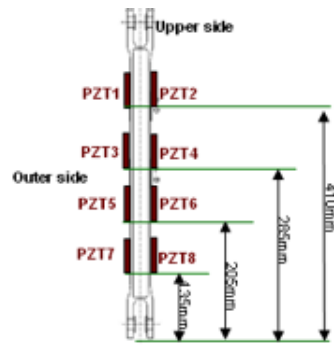
The type of actuators employed were piezoelectric patches that are not bulky and do not affect the mechanical structure significantly. Their locations were selected by the aerospace engineers of the laboratory after performing a laser scanner analysis [17]. Following the results of these tests, 16 patches were placed on the two rear struts (8 on the left one and 8 on the right one) and 24 on the anti-torque plate (12 on the left side and 12 on the right side) for a total of 40 actuators. No actuator was placed on the front struts because no significant vibration field was detected in the part of the roof corresponding to their structural attachments to the cabin. The actuators location is shown in Figure 1.9.



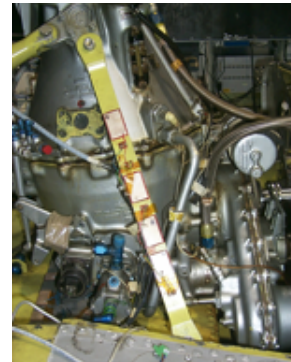
(a) Actuators on one side of the anti-torque plate



(b) Actuators on one side of the anti-torque plate



(c) Actuators on the rear struts



(d) Actuators on the rear struts

Figure 1.9: Actuators location [17].

1.5.3 Choice of sensors and their location

During the *Friendcopter* project, the type of sensors chosen were accelerometers. In this project 6 accelerometers were used, 3 per side and they were placed all on the cabin roof. Considering just one side of the cabin, 2 accelerometers were placed at the points of the structural attachment of the anti-torque plate, and the remaining one at the point of structural attachment of the rear strut.

1.5.4 Disturbance frequencies

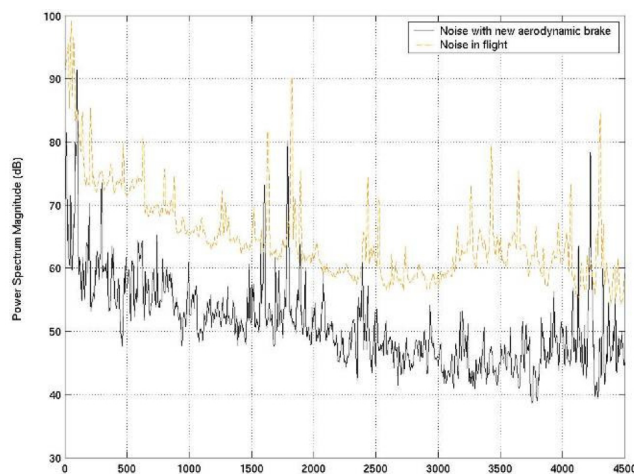


Figure 1.10: Noise spectrum inside the cabin. [17].

The frequency response inside the cabin due to the rotor motion was identified and is shown in Figure 1.10. It is possible to distinguish among three types of noise: large amplitude, low frequency (< 200 Hz) rotor harmonics that are far from the speech frequency range, broadband noise and higher frequency tones that are considered to be the most annoying for the human ear. In this specific case the higher frequency tones are at 1599 Hz, 1785 Hz, 2400 Hz, and 4250 Hz [17]. The attenuation of these high frequency tones is generally the main objective of active vibration control in helicopters.

1.5.5 Type of control

During the *Friendcopter* project an active vibration attenuation system was developed. The system was a semi-decentralized feedforward controller: each group of actuators was controlled independently, so that there was a controller for the actuators on the left rear strut, a controller for the actuators on the left side of the anti-torque plate, a controller for the right rear strut and a controller for the actuators on the right side of anti-torque plate.

The algorithm used was the normalized FxLMS with a FIR filter of 100 coefficients [17]. The idea for this configuration was based on experimental analysis that showed that the actuators on the left part of the helicopter do not have much authority on the sensors located on the right part of the cabin and vice versa. Although this might be true for the actuators on the rear struts, all the output signals are not negligible when an actuator on the anti-torque plate is excited. With such a configuration only an attenuation of the main peaks was obtained, allowing however higher broadband noise levels.

The semi-decentralized control approach is not a good choice for this category of problems because the actuators might fight each other. In other words, in such a configuration the vibrations created by a group of actuators might be seen as vibrations to be attenuated by another group of actuators.

1.6 Current project description

In the current work the same set-up was used, apart from the accelerometers whose number was augmented to 9 per side, for a total of 18. They were placed in the area of the roof to be monitored, where high vibration levels are present. Due to the lack of reference points in the roof, the sensors are not perfectly symmetric between the left and right side. A large number of accelerometers was used under the assumption that the higher the number of measurements, the higher the attenuation of the disturbance that can be achieved, although this is not always guaranteed. The sensitivity of the accelerometers used is shown in the table 1.1.

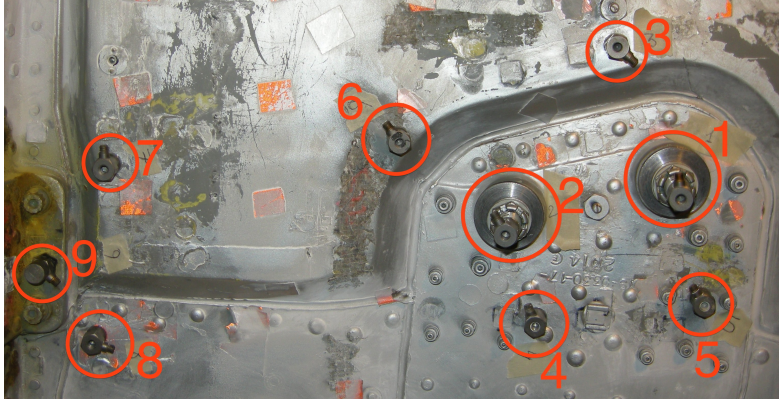


Figure 1.11: Locations of the accelerometers on the left side of the cabin. The accelerometers 1 and 2 are the ones corresponding to the anti-torque plate structural attachment while the accelerometer 9 is the one corresponding to the rear strut structural attachment. The others are the ones that have been added in the current project.

Accelerometer	Model	Serial Number	Sensibility[mv/g]
1	333B32	14492	100.1
2	333B32	13967	105
3	352C33	69539	100.1
4	352C33	69541	99.8
5	333B32	31666	99.0
6	352C33	69535	100.1
7	352C33	69540	100.1
8	333B32	14479	102.2
9	352C33	69538	99.0
10	352C33	69533	99.7
11	352C33	69534	102.3
12	352C33	70273	100
13	333B32	13974	98.2
14	333B32	14779	101.6
15	352C33	69532	99.4
16	352C33	69543	99.0
17	352C33	69530	107.3
18	352C33	69536	101.1

Table 1.1: Table of the accelerometer sensitivities.

1.6.1 Acquisition system

The acquisition system employed consists of two PCI's (PCI-6251, PCI-MIO-16E-1) that are used to acquire the signals of the accelerometers and to generate the excitation signals for the actuators. The generated signals are sent to a reconstruction filter with cut-off frequency set to 5 kHz and to a power amplifier whose gain was set to 20. The accelerometers are connected to the 478A16 signal conditioners that provide the voltage supply needed by the sensors. The software used to perform the experiments and to set the devices correctly is NI LabVIEW SignalExpress. The sampling frequency was set to 10 kHz and the cut-off frequency of the anti-aliasing filters was set to 5 kHz. Both the anti-aliasing filters and the reconstruction filters are KEMO 8 BenchMaster 21M. All the data are analysed using MATLAB and the same program was used to estimate the model.

1.6.2 Problem statement and objective of the work

The final goal of this study is to attenuate the acoustic noise and vibrations at least in a specific and reduced volume of the helicopter fuselage. Specifically, it would be desirable to reduce the noise in the volume where the passengers are supposed to sit. This is partially achieved with active techniques as the ones seen in this chapter. Most of them need however a reliable model of the system to be controlled. The estimation of such a model is the main objective of this thesis. The particularity of this work is the large number of input and output channels of the system that makes the identification process more difficult. No example is documented in the literature of such a large system for noise and vibration reduction purposes. The identification was carried out with different techniques to obtain satisfactory results.

The problem of control was sketched out, which is also quite complex in view of the size of the MIMO system. Particularly in this work, a way to simplify the MIMO system was investigated and a control algorithm specific for active vibration reduction in helicopters has been simulated in order to understand if such a control can be applied to the system.

Chapter 2

Subspace model identification

In this chapter the underlying theory for the subspace identification methods used for a discrete LTI (state space) system with exogenous input and without a feedback loop is presented. Particularly the ordinary MOESP (and its variants PI-MOESP and PO-MOESP) and the N4SID methods are presented.

Shortly, also their implementation in the Matlab environment is discussed.

2.1 Reachability and Observability matrices

Consider a discrete-time LTI system described by the model in equation (2.1):

$$x(t+1) = Ax(t) + Bu(t) \tag{2.1a}$$

$$y(t) = Cx(t) + Du(t) \tag{2.1b}$$

where $x(t) \in \mathbb{R}^n$, $u(t) \in \mathbb{R}^m$ and $y(t) \in \mathbb{R}^p$ are respectively the state vector, the control signals and the output signal; t represents the discrete time variable. The matrix $A \in \mathbb{R}^{n \times n}$ is the dynamic matrix, $B \in \mathbb{R}^{n \times m}$ is the input matrix, $C \in \mathbb{R}^{p \times n}$ is the output matrix and $D \in \mathbb{R}^{p \times n}$ is the feedthrough matrix.

Such a system (the pair (A, C)) is said to be observable if two different initial states do not exist such that their corresponding output motions are identical. In other words, a system is observable if, starting from its output $y(t)$, it is possible to see the effect of each state variation. A system is observable if and only if the observability matrix \mathcal{O} defined in the expression (2.2) is full rank or equivalently,

its rank is equal to the system order n .

$$\mathcal{O} = \begin{bmatrix} C \\ CA \\ CA^2 \\ \vdots \\ CA^{n-1} \end{bmatrix}. \quad (2.2)$$

A state space system (the pair (A, B)) (from input $u(t)$) is reachable if starting from a null initial state we can always find an input signal which leads the system to any a-priori selected final state in finite time. Reachability from $u(t)$ indicates in practice that $u(t)$ affects all the system states. A system is reachable (from $u(t)$) if and only if the Reachability matrix \mathcal{R} defined in equation (2.3) is full rank or equivalently its rank is equal to the system order n .

$$\mathcal{R} = [B \quad AB \quad A^2B \quad \cdots \quad A^{n-1}B]. \quad (2.3)$$

2.2 Realization problem

Consider again the discrete-time LTI system described by the equations (2.1) assumed to be reachable and observable: in this case we say that (A, B, C) is minimal.

Suppose that the matrices of the system are unknown but that input and output data $\{u(t), y(t), t = 1, \dots, N-1\}$ are given. The problem is to identify the dimension n of the system and its matrices, up to a similarity transformation. This is a subspace identification problem for a deterministic LTI system. To perform this task some data matrices are defined.

2.2.1 Data matrices

Consider a LTI system at rest ($u(t) = 0, y(t) = 0$ for $t < 0$) and suppose the input and output data to be $(u(0), u(1), \dots, u(N-1)), (y(0), y(1), \dots, y(N-1))$ where N is sufficiently large. Then for $k > 0$ we get

$$[y(0) \quad \cdots \quad y(N-1)] = [g_{k-1} \quad \cdots \quad g_0] \begin{bmatrix} 0 & \cdots & 0 & u(0) & \cdots & u(N-k) \\ \vdots & \ddots & \ddots & u(1) & \cdots & u(N-k+1) \\ 0 & \ddots & \ddots & \vdots & & \vdots \\ u(0) & u(1) & \cdots & u(k-1) & \cdots & u(N-1) \end{bmatrix} \quad (2.4)$$

where $[g_{k-1} \ \cdots \ g_0]$ is the impulse response that can be calculated using the least square method if the right hand matrix is full rank.

Suppose the input and output data are given and that $k > n$ where n is the dimension of the state vector. Then we can build the block Henkel matrices defined below:

$$U_{0|k-1} = \begin{bmatrix} u(0) & u(1) & \cdots & u(N-1) \\ \vdots & \vdots & & \vdots \\ u(k-1) & u(k) & \cdots & u(k+N-2) \end{bmatrix} \in \mathbb{R}^{km \times N} \quad (2.5)$$

and

$$Y_{0|k-1} = \begin{bmatrix} y(0) & y(1) & \cdots & y(N-1) \\ \vdots & \vdots & & \vdots \\ y(k-1) & y(k) & \cdots & y(k+N-2) \end{bmatrix} \in \mathbb{R}^{kp \times N} \quad (2.6)$$

where the number of columns is usually fixed to a sufficiently large N . Combining iteratively the two equations of the state space system we get equation (2.7):

$$\begin{bmatrix} y(t) \\ \vdots \\ y(t+k-1) \end{bmatrix} = \begin{bmatrix} C \\ \vdots \\ C A^{k-1} \end{bmatrix} x(t) + \begin{bmatrix} D & & \\ \vdots & \ddots & \\ C A^{k-2} B & \cdots & C B D \end{bmatrix} \begin{bmatrix} u(t) \\ \vdots \\ u(t+k-1) \end{bmatrix}. \quad (2.7)$$

We define

$$y_k(t) = \begin{bmatrix} y(t) \\ y(t+1) \\ \vdots \\ y(t+k-1) \end{bmatrix} \in \mathbb{R}^{kp} \quad (2.8a) \quad u_k(t) = \begin{bmatrix} u(t) \\ u(t+1) \\ \vdots \\ u(t+k-1) \end{bmatrix} \in \mathbb{R}^{km} \quad (2.8b)$$

and the block Toeplitz matrix

$$\Phi_k = \begin{bmatrix} D & & \\ C B & D & \\ \vdots & \ddots & \ddots \\ C A^{k-2} B & \cdots & C B D \end{bmatrix} \in \mathbb{R}^{kp \times km}. \quad (2.9)$$

Then we can redefine equation (2.7) as

$$\mathbf{y}_k(t) = \mathcal{O}_k x(t) + \Phi_k \mathbf{u}_k(t) \quad (2.10)$$

for $t = 0, 1, \dots, k - 1$. Then the block Hankel matrices can be expressed as:

$$U_{0|k-1} = [\mathbf{u}_k(0) \quad \mathbf{u}_k(1) \quad \cdots \quad \mathbf{u}_k(N - 1)] \quad (2.11a)$$

$$Y_{0|k-1} = [\mathbf{y}_k(0) \quad \mathbf{y}_k(1) \quad \cdots \quad \mathbf{y}_k(N - 1)] . \quad (2.11b)$$

Combining equations (2.10) and (2.11) yields:

$$Y_{0|k-1} = \mathcal{O}_k X_0 + \Phi_k U_{0|k-1} \quad (2.12)$$

where $X_0 = [x(0) \quad x(1) \quad \cdots \quad x(N - 1)] \in \mathbb{R}^{n \times N}$ is the initial state matrix. Similarly we define

$$U_{k|2k-1} = [\mathbf{u}_k(k) \quad \mathbf{u}_k(k + 1) \quad \cdots \quad \mathbf{u}_k(N + k - 1)] \quad (2.13a)$$

$$Y_{k|2k-1} = [\mathbf{y}_k(k) \quad \mathbf{y}_k(k + 1) \quad \cdots \quad \mathbf{y}_k(N + k - 1)] . \quad (2.13b)$$

Then for $t = k, k + 1, \dots, k + N - 1$ we have:

$$Y_{k|2k-1} = \mathcal{O}_k X_k + \Phi_k U_{k|2k-1} \quad (2.14)$$

where $X_k = [x(k) \quad x(k + 1) \quad \cdots \quad x(k + N - 1)] \in \mathbb{R}^{n \times N}$. The block Hankel matrices $U_{0|k-1}$ and $Y_{0|k-1}$ are usually called the past inputs and past outputs, respectively, whereas the block Hankel matrices $U_{k|2k-1}$ and $Y_{k|2k-1}$ are called the future inputs and future outputs, respectively.

Now we make some assumptions that will be used later:

- $rank(X_0) = n$
- $rank(U_{0|k-1}) = km$ where $k > n$
- $span(X_0) \cap span(U_{0|k-1}) = 0$

where $span(\cdot)$ denotes the space spanned by the row vectors of a matrix. The first assumption ensures that the state vector is sufficiently excited. The second one ensures that the input sequence satisfies the persistently exciting (PE) condition of order k . The third assumption means that the row vectors of X_0 and $U_{0|k-1}$ are linearly independent or in other words that there is no feedback (data are obtained from open loop experiment).

2.2.2 LQ decomposition

The solution of the identification problem exploits the orthogonal decomposition of a matrix. In this case the LQ decomposition is considered.

Suppose we have rectangular data matrices with a large number of columns. Applying the LQ decomposition we get a block lower triangular matrix with a zero block at the upper right corner. The LQ decomposition, obtained by taking the transpose of the QR, is considered and it amounts to:

$$\begin{bmatrix} U_{0|k-1} \\ Y_{0|k-1} \end{bmatrix} = \begin{bmatrix} L_{11} & 0 \\ L_{21} & L_{22} \end{bmatrix} \begin{bmatrix} Q_1^T \\ Q_2^T \end{bmatrix} \quad (2.15)$$

where $L_{11} \in \mathbb{R}^{km \times km}$, $L_{21} \in \mathbb{R}^{kp \times km}$ and $L_{22} \in \mathbb{R}^{kp \times kp}$, with L_{11}, L_{22} lower triangular and $Q_1 \in \mathbb{R}^{N \times km}$, $Q_2 \in \mathbb{R}^{N \times kp}$ are orthogonal.

It can be proven that $\text{rank}(L_{22}) = n$, where n is the order of the system so that now we have the first piece of information needed to identify the model. As a consequence computing the Singular Value Decomposition (SVD) of L_{22} , the order of the system is given by the number of the singular values bigger than zero. This is also the rank of the observability matrix. Knowing the rank and the observability matrix, we can estimate the matrices A, C while the information of matrices B, D is included in the matrices L_{11}, L_{21} .

2.2.3 MOESP algorithm

The Multivariable Output Error State Space algorithm, commonly known as MOESP algorithm developed by Verhaegen and Dewilde exploits the orthogonal projection, expressed as $\hat{E}\{.\mid.\}$ [8].

From the LQ decomposition equation we obtain two matrix equations:

$$U_{0|k-1} = L_{11}Q_1^T \implies Q_1^T = L_{11}^{-1}U_{0|k-1} \quad (2.16a)$$

$$Y_{0|k-1} = L_{21}Q_1^T + L_{22}Q_2^T \implies Y_{0|k-1} = L_{21}L_{11}^{-1}U_{0|k-1} + L_{22}Q_2^T. \quad (2.16b)$$

Using the previous assumptions, it can be noticed that L_{11} is nonsingular so that the equivalence in the first equation is obtained. Using this result the equivalence in the second equation is obtained.

From the orthogonality of Q_1 and Q_2 we obtain that the first term of the right hand side of the second equation is spanned by the row vectors of $U_{0|k-1}$ and the second term is orthogonal to it. Hence the orthogonal projection of the row space of $Y_{0|k-1}$ onto the row space of $U_{0|k-1}$ is given by equation (2.17)

$$\hat{E}\{Y_{0|k-1} \mid U_{0|k-1}\} = L_{21}Q_1^T = L_{21}L_{11}^{-1}U_{0|k-1} \quad (2.17)$$

and the orthogonal projection of the row space of $Y_{0|k-1}$ onto the complement $U_{0|k-1}^\perp$ of the row space $U_{0|k-1}$ is given by

$$\hat{E}\{Y_{0|k-1}|U_{0|k-1}^\perp\} = L_{22}Q_2^T. \quad (2.18)$$

Combining equation (2.12) and (2.16) it follows that

$$\mathcal{O}_k X_0 + \Phi_k L_{11} Q_1^T = L_{21} Q_1^T + L_{22} Q_2^T \quad (2.19)$$

where the right hand side is an orthogonal sum while the left hand side is not, so the equivalence between single terms does not hold. Post multiplying by Q_2 (recalling that $Q_1^T Q_2 = 0$, $Q_2^T Q_2 = I_{kp}$) yields:

$$\mathcal{O}_k X_0 Q_2 = L_{22}. \quad (2.20)$$

Under the previous assumptions and supposing $rank(\mathcal{O}_k) = n$ then the product $X_0 Q_2$ has full row rank n and $rank(\mathcal{O}_k) = n = rank(L_{22})$. Performing the SVD on L_{22} we get the order n :

$$L_{22} = [U_1 \ U_2] \begin{bmatrix} \Sigma_1 & 0 \\ 0 & 0 \end{bmatrix} \begin{bmatrix} V_1^T \\ V_2^T \end{bmatrix} = U_1 \Sigma_1 V_1^T \quad (2.21)$$

where $U_1 \in \mathbb{R}^{kp \times n}$ and $U_2 \in \mathbb{R}^{kp \times (kp-n)}$. Then substituting the result in equation (2.21) we get:

$$\mathcal{O}_k X_0 Q_2 = U_1 \Sigma_1 V_1^T. \quad (2.22)$$

We define the extended observability matrix as

$$\mathcal{O}_k = U_1 \Sigma_1^{\frac{1}{2}} \quad (2.23)$$

and $n = dim(\Sigma_1)$. At this point, recalling the definition of the observability matrix given in equation (2.2) and knowing the order of the model, we can extract the C matrix of the system:

$$C = \mathcal{O}_k(1 : p, 1 : n). \quad (2.24)$$

Matrix A is obtained by solving the following linear matrix equation:

$$\mathcal{O}_k(1 : p(k-1), 1 : n)A = \mathcal{O}_k(p+1 : kp, 1 : n). \quad (2.25)$$

Now we have to estimate the matrices B and D . From equation (2.21), it is possible to notice that $U_2^T L_{22} = 0$ and consequently from equation (2.20) we have that $U_2^T \mathcal{O}_k = 0$. Pre-multiplying equation (2.19) by U_2^T yields:

$$U_2^T \Phi_k L_{11} Q_1^T = U_2^T L_{21} Q_1^T \quad (2.26)$$

and post-multiplying by Q_1 yields:

$$U_2^T \begin{bmatrix} D & 0 & \cdots & 0 \\ CB & D & \cdots & 0 \\ \vdots & \vdots & \ddots & \vdots \\ CA^{k-2}B & CA^{k-3}B & \cdots & D \end{bmatrix} = U_2^T L_{21} L_{11}^{-1}. \quad (2.27)$$

This is a linear matrix equation with respect to B and D hence the least squares method can be adopted to find the two matrices. Let us define

$$U_2^T := [\mathcal{L}_1 \quad \mathcal{L}_2 \quad \cdots \quad \mathcal{L}_k] \quad (2.28a)$$

$$U_2^T L_{21} L_{11}^{-1} := [\mathcal{M}_1 \quad \mathcal{M}_2 \quad \cdots \quad \mathcal{M}_k] \quad (2.28b)$$

where $\mathcal{L}_i \in \mathbb{R}^{(kp-n) \times p}$, $i = 1, \dots, k$ and $\mathcal{M}_i \in \mathbb{R}^{(kp-n) \times m}$, $i = 1, \dots, k$. Thus we obtain the following linear system:

$$\mathcal{L}_1 D + \mathcal{L}_2 CB + \cdots + \mathcal{L}_{k-1} CA^{k-3}B + \mathcal{L}_k CA^{k-2}B = \mathcal{M}_1 \quad (2.29a)$$

$$\mathcal{L}_2 D + \mathcal{L}_3 CB + \cdots + \mathcal{L}_k CA^{k-3}B = \mathcal{M}_2 \quad (2.29b)$$

$$\vdots \quad (2.29c)$$

$$\mathcal{L}_{k-1} D + \mathcal{L}_k CB = \mathcal{M}_{k-1} \quad (2.29d)$$

$$\mathcal{L}_k D = \mathcal{M}_k \quad (2.29e)$$

Defining $\bar{\mathcal{L}}_i = [\mathcal{L}_i \quad \cdots \quad \mathcal{L}_k] \in \mathbb{R}^{(kp-n) \times (k+1-i)p}$, $i = 2, \dots, k$ then we get the following overdetermined linear equation:

$$\begin{bmatrix} \mathcal{L}_1 & \bar{\mathcal{L}}_2 \mathcal{O}_{k-1} \\ \mathcal{L}_2 & \bar{\mathcal{L}}_3 \mathcal{O}_{k-2} \\ \cdots & \cdots \\ \mathcal{L}_{k-1} & \bar{\mathcal{L}}_k \mathcal{O}_1 \\ \mathcal{L}_k & 0 \end{bmatrix} \begin{bmatrix} D \\ B \end{bmatrix} = \begin{bmatrix} \mathcal{M}_1 \\ \mathcal{M}_2 \\ \cdots \\ \mathcal{M}_{k-1} \\ \mathcal{M}_k \end{bmatrix}. \quad (2.30)$$

To obtain a unique least square solution for B and D the block matrix must have full column rank, so that $k(kp - n) \geq (p + n)$ holds: this condition is satisfied if $k > n$,

as it was assumed before. Finally, the initial state can be estimated from equation (2.12).

Summarizing, if we are given the data matrices $U_{0|k-1}$ and $Y_{0|k-1}$ we have the following algorithm procedures:

- compute the LQ decomposition as in equation (2.15);
- compute the SVD of matrix L_{22} found at the previous step as in equation (2.21) and let $n = \dim(\Sigma_1)$; define the extended observability matrix as $\mathcal{O}_k = U_1 \Sigma_1^{\frac{1}{2}}$;
- calculate the C and A matrices as in equation (2.24) and (2.25) respectively;
- solve the equation (2.30) using the least-square method to estimate B and D ;
- estimate the initial state vector from equation (2.12).

This algorithm is called ordinary MOESP (OM-MOESP) or simply MOESP and the assumption under which it was developed is that the measurements are not affected by noise. In the next section the effects of random noise in the measurements are presented. Then two variations of the classical MOESP are explained that can deal with noise affecting the system.

Note that to describe the MOESP algorithm the LQ decomposition was exploited. Exactly the same conclusions can be derived using the QR decomposition.

2.2.4 SVD and additive white noise

Until now we have assumed a complete noise-free dataset but in practice this is never the case. However, it has been proven that if a system is disturbed in its measurements by a white noise process, the problem can still be solved with ordinary MOESP. The presence of noise introduces new singular values so that the rank of L_{22} is not equal to the model order n anymore but it is bigger and the order of the system might be overestimated. However, generally the singular values related to noise are much smaller than the singular values related to the real system. Hence, recalling that $\sigma_1 \geq \sigma_2 \geq \dots \geq \sigma_n$ when plotting them we should note the presence of a gap as shown in Figure 2.1: in this case the order of the model corresponds to the number of singular values significantly bigger than zeros. When such a gap does not exist, an arbitrary choice about the system order must be made; an example of this situation is shown in Figure 2.2.

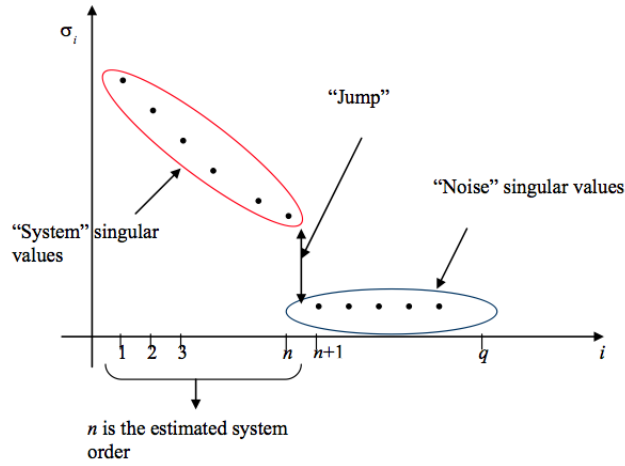


Figure 2.1: Plot of singular values of in case of noisy measurements with a visible gap.

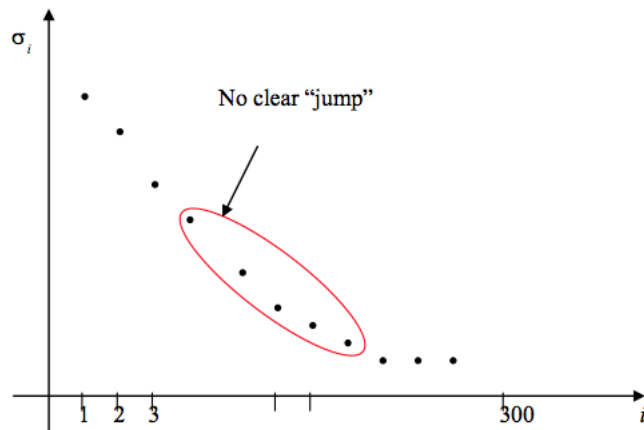


Figure 2.2: Plot of singular values in case of noisy measurements without a visible gap.

2.3 PI-MOESP algorithm

The ordinary MOESP can only deal with white noise on the measurements while real measurements might contain other types of random noise: hence when the measurements are disturbed by a coloured noise signal, a new algorithm is necessary: this is the case of the Past Input Instrumental Variable MOESP (PI-MOESP) proposed by Verhaegen and Dewilde [5].

The system is described by the following state space equations:

$$x(t+1) = Ax(t) + Bu(t) \quad (2.31a)$$

$$y(t) = Cx(t) + Du(t) + e(t) \quad (2.31b)$$

where $e(t)$ is a colored noise perturbation. Note that we assume that the state equation is not affected by noise. A scheme of the system is shown in Figure 2.3

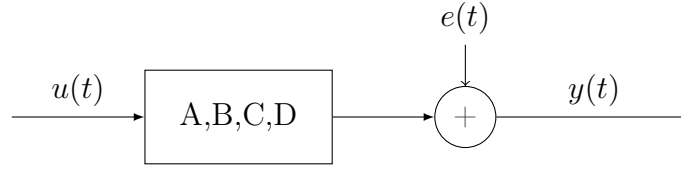


Figure 2.3: Output error identification scheme.

The data equation is now given by

$$Y_{k|2k-1} = \mathcal{O}_k X_0 + \Phi_k U_{k|2k-1} + E_{k|2k-1} \quad (2.32)$$

where $E_{k|2k-1}$ is the noise block Hankel matrix. For the estimation of A and C in the ordinary MOESP the data equation in (2.19) has been multiplied by Q_2 to obtain equation (2.20). Now a new variable \mathcal{Z} , uncorrelated with the noise signal but correlated with the state vector, is introduced in order to remove the influence of the noise on the output. A good choice for this variable is a matrix constructed from past input values so that $\mathcal{Z} = U_{0|k-1}$. Now it is possible to eliminate the undesired terms by multiplying the equation by the orthogonal complement of $U_{k|2k-1}$ (as in the MOESP) and by \mathcal{Z} . The data matrix is finally given by:

$$\begin{bmatrix} U_{k|2k-1} \\ \mathcal{Z} \\ Y_{k|2k-1} \end{bmatrix} = \begin{bmatrix} U_{k|2k-1} \\ U_{0|k-1} \\ Y_{k|2k-1} \end{bmatrix} = \begin{bmatrix} L_{11} & 0 & 0 \\ L_{21} & L_{22} & 0 \\ L_{31} & L_{32} & L_{33} \end{bmatrix} \begin{bmatrix} Q_1^T \\ Q_2^T \\ Q_3^T \end{bmatrix}. \quad (2.33)$$

Now the SVD analysis must be performed over the matrix L_{32} . Firstly the estimation of matrices A and C is performed using the same procedure as for the ordinary MOESP. Then as done for the previous algorithm it is possible to estimate in the same way the matrices B and D and the initial state x_0 .

2.4 PO-MOESP algorithm

So far, only the case of measurement noise was considered. However, if the system is also disturbed by an additive noise, the previous algorithms are no longer effective. In this case, another algorithm is available, which is commonly known as Past Output Instrumental Variable MOESP (PO-MOESP) [5]. The state space model is now given by

$$x(t+1) = Ax(t) + Bu(t) + w(t) \quad (2.34a)$$

$$y(t) = Cx(t) + Du(t) + e(t) \quad (2.34b)$$

where $e(t)$ is called measurement noise and $w(t)$ is called process noise. The corresponding scheme is shown in Figure 2.4. Let $w(t)$ and $e(t)$ be zero mean noise

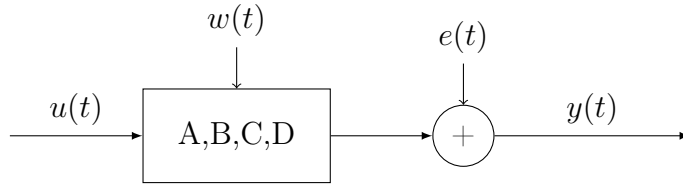


Figure 2.4: Innovation model identification scheme.

sequences that are statistically independent from the input $u(t)$. Let the pair (A, B) be controllable and the pair (A, C) be observable, let the system be stable and the input $u(t)$ persistently exciting. We can define the system in the following equivalent form:

$$\hat{x}(t+1) = A\hat{x}(t) + Bu(t) + Ke(t) \quad (2.35a)$$

$$\hat{y}(t) = C\hat{x}(t) + Du(t) \quad (2.35b)$$

$$y(t) = \hat{y}(t) + e(t) \quad (2.35c)$$

where the matrix K is called the Kalman gain. So now the problem is to estimate the system order n , the matrices of the system A, B, C, D , the kalman gain matrix K and the initial state vector. Now in the data equation another term is present:

$$Y_{k|2k-1} = \mathcal{O}_k X_k + \Phi_k U_{k|2k-1} + E_{k|2k-1} + G_k W_{k|2k-1} \quad (2.36)$$

where

$$G_k = \begin{bmatrix} 0 & 0 & \cdots & 0 \\ C & 0 & \cdots & 0 \\ CA & C & \cdots & 0 \\ CA^{k-2} & CA^{k-3} & \cdots & 0 \end{bmatrix}. \quad (2.37)$$

Again all the terms on the right hand side must be removed except $\mathcal{O}_k X_k$. As for the PI-MOESP if the number of samples is big enough, the noises are uncorrelated with the input and we can use the instrumental variable: now also the past output block Hankel matrix is introduced. First, data are projected on the orthogonal complement of $U(k|2k-1)$ to remove $\Phi_k U_{k|2k-1}$; then they are projected onto the instrumental variable to remove the two noise terms.

The instrumental variable \mathcal{Z} is now defined as follows:

$$\mathcal{Z} = \begin{bmatrix} U_{0|k-1} \\ Y_{0|k-1} \end{bmatrix}. \quad (2.38)$$

The result using the LQ factorization is:

$$\begin{bmatrix} U_{k|2k-1} \\ \mathcal{Z} \\ Y_{k|2k-1} \end{bmatrix} = \begin{bmatrix} U_{k|2k-1} \\ U_{0|k-1} \\ Y_{0|k-1} \\ Y_{k|2k-1} \end{bmatrix} = \begin{bmatrix} L_{11} & 0 & 0 & 0 \\ L_{21} & L_{22} & 0 & 0 \\ L_{31} & L_{32} & L_{33} & 0 \\ L_{41} & L_{42} & L_{43} & L_{44} \end{bmatrix} \begin{bmatrix} Q_1^T \\ Q_2^T \\ Q_3^T \\ Q_4^T \end{bmatrix}. \quad (2.39)$$

The SVD analysis is performed on $[L_{42} \ L_{43}]$ to get the order of the system; then the estimation of A and C is done in the same way of the previous algorithms. In this way the deterministic part of the system has been estimated.

Now the stochastic part needs to be estimated as well. The data equation of the innovation model is:

$$Y_{k|2k-1} = \mathcal{O}_k \hat{X}_k + \Phi_k U_{k|2k-1} + M_k E_{k|2k-1} \quad (2.40)$$

where

$$M_k = \begin{bmatrix} I_p & 0 & \cdots & 0 \\ C K & I_p & \cdots & 0 \\ C A & C & \cdots & 0 \\ C A^{k-2} K & \cdots & C K & I_p \end{bmatrix}. \quad (2.41)$$

First the state sequence \hat{X}_k needs to be estimated. Combining the equations of (2.35) we get:

$$\hat{x}(t+1) = \bar{A} \hat{x}(t) + \bar{B} u(t) + K y(t) \quad (2.42)$$

with $\bar{A} = A - KC$ and $\bar{B} = B - KD$. The state sequence can be written as a function of the initial state:

$$\hat{X}_k = \bar{A}^k \hat{X}_0 + \mathcal{C}_{u,k} U_{0|k-1} + \mathcal{C}_{y,k} Y_{0|k-1} \quad (2.43)$$

where

$$\mathcal{C}_{u,k} = \begin{bmatrix} \overline{A}^{k-1} \overline{B} & \overline{A}^{k-2} \overline{B} & \cdots & B \end{bmatrix} \quad (2.44a)$$

$$\mathcal{C}_{y,k} = \begin{bmatrix} \overline{A}^{k-1} K & \overline{A}^{k-2} K & \cdots & K \end{bmatrix}. \quad (2.44b)$$

Since \overline{A} is stable, the term $\overline{A}^k \hat{X}_0$ disappears as $k \rightarrow \infty$.

Let us call the projection operator onto the space spanned by \mathcal{Z} , $\Pi_{\mathcal{Z}}$. Substituting equation (2.43) onto equation (2.40), after some manipulation, \hat{X}_k can be estimated as:

$$\hat{X}_k = \mathcal{O}_k^\dagger (Y_{k|2k-1} \Pi_{\mathcal{Z}} - \Phi_k U_{k|2k-1}) \quad (2.45)$$

and a similar equation can be obtained for $\hat{X}_{k+1|2k}$.

Now that we have the state sequences we can solve the following equation

$$\begin{bmatrix} \hat{X}_{k+1|2k} \\ Y_{k+1|2k-1} \end{bmatrix} = \begin{bmatrix} \hat{A} & \hat{B} \\ \hat{C} & \hat{D} \end{bmatrix} \begin{bmatrix} \hat{X}_{k|k-1} \\ U_{k|k-1} \end{bmatrix} + \begin{bmatrix} \hat{W}_{k|2k-1} \\ \hat{V}_{k|2k-1} \end{bmatrix} \quad (2.46)$$

for $\hat{W}_{k|2k-1}$ and $\hat{V}_{k|2k-1}$. The covariance matrices are then estimated by

$$\begin{bmatrix} \hat{Q} & \hat{S} \\ \hat{S}^T & \hat{R} \end{bmatrix} = \frac{1}{N} \begin{bmatrix} \hat{W}_{k|2k-1} \\ \hat{V}_{k|2k-1} \end{bmatrix} \begin{bmatrix} \hat{W}_{k|2k-1} \\ \hat{V}_{k|2k-1} \end{bmatrix}^T \quad (2.47)$$

and with these estimates we can calculate the Kalman filter gain K as:

$$\hat{K} = (\hat{A} \hat{P} \hat{C}^T + \hat{S})(\hat{C} \hat{P} \hat{C}^T + \hat{R})^{-1} \quad (2.48a)$$

$$\hat{P} = \hat{A} \hat{P} \hat{A}^T + \hat{Q} - (\hat{A} \hat{P} \hat{C}^T \hat{S})(\hat{C} \hat{P} \hat{C}^T + \hat{R})^{-1} (\hat{A} \hat{P} \hat{C}^T + \hat{S})^T. \quad (2.48b)$$

2.5 N4SID algorithm

The N4SID algorithm is another method developed by Van Overschee and De Moor to solve the identification problem, that together with the previous ones belongs to the subspace algorithm class [8].

Let us define $U_p = U_{0|k-1}$ $Y_p = Y_{0|k-1}$ $X_p = X_0$ and $U_f = U_{k|2k-1}$ $Y_f = Y_{k|2k-1}$ $X_f = X_k$ where the subscripts p and f denote respectively the past and future. Recalling the two output equations, one has that:

$$Y_p = \mathcal{O}_k X_p + \Phi_k U_p \quad (2.49a)$$

$$Y_f = \mathcal{O}_k X_f + \Phi_k U_f. \quad (2.49b)$$

We define also $W_f, W_p \in \mathbb{R}^{(m+p) \times N}$ as

$$W_p = \begin{bmatrix} U_p \\ Y_p \end{bmatrix} = \begin{bmatrix} U_{0|k-1} \\ Y_{0|k-1} \end{bmatrix} \quad (2.50a)$$

$$W_f = \begin{bmatrix} U_f \\ Y_f \end{bmatrix} = \begin{bmatrix} U_{k|2k-1} \\ Y_{k|2k-1} \end{bmatrix}. \quad (2.50b)$$

Performing the LQ decomposition the following equation is obtained:

$$\begin{bmatrix} U_f \\ U_p \\ Y_p \\ Y_f \end{bmatrix} = \begin{bmatrix} L_{11} & 0 & 0 & 0 \\ L_{21} & L_{22} & 0 & 0 \\ L_{31} & L_{32} & L_{33} & 0 \\ L_{41} & L_{42} & L_{43} & L_{44} \end{bmatrix} \begin{bmatrix} Q_1^T \\ Q_2^T \\ Q_3^T \\ Q_4^T \end{bmatrix} \quad (2.51)$$

where $L_{11}, L_{22} \in \mathbb{R}^{km \times km}$, $L_{33}, L_{44} \in \mathbb{R}^{kp \times kp}$ are lower triangular and where $Q_1, Q_2 \in \mathbb{R}^{N \times km}$, $Q_3, Q_4 \in \mathbb{R}^{N \times kp}$ are orthogonal. For convenience let us rewrite this equations as follows:

$$\begin{bmatrix} U_f \\ W_p \\ Y_f \end{bmatrix} = \begin{bmatrix} R_{11} & 0 & 0 \\ R_{21} & R_{22} & 0 \\ R_{31} & R_{32} & R_{33} \end{bmatrix} \begin{bmatrix} \overline{Q}_1^T \\ \overline{Q}_2^T \\ \overline{Q}_3^T \end{bmatrix}. \quad (2.52)$$

Now from the second relation we have

$$R_{22} \overline{Q}_2^T = W_p - R_{21} \overline{Q}_1^T. \quad (2.53)$$

Thus

$$Q_2^T = R_{22}^\dagger (W_p - R_{21} \overline{Q}_1^T). \quad (2.54)$$

From the third relation of equation (2.52) we have that

$$Y_f = R_{31} \overline{Q}_1^T + R_{32} \overline{Q}_2^T. \quad (2.55)$$

Substituting equation (2.54) and using $\overline{Q}_1^T = R_{11}^{-1} U_f$ from the first relation of (2.52)

$$Y_f = (R_{31} - R_{32} R_{22}^\dagger R_{21}) R_{11}^{-1} U_f + R_{32} R_{22}^\dagger W_p \quad (2.56)$$

where the right hand side is a direct sum of of the oblique projections of Y_f onto $\text{span}(U_f)$ along $\text{span}(W_p)$ and of Y_f onto $\text{span}(W_p)$ along $\text{span}(U_f)$.

Using the assumptions made in the subsection 2.2.1:

$$\text{rank}(L_{42}) = \text{rank}(L_{43}) = \text{rank} \begin{bmatrix} L_{33} \\ L_{43} \end{bmatrix} = \text{rank} [L_{42} \quad L_{43}] = n. \quad (2.57)$$

Let the oblique projection of Y_f onto W_p along U_f be given by (using the results of equation (2.56)):

$$\xi = \hat{E}_{\parallel U_f} \{Y_f | W_p\} = R_{32} R_{22}^\dagger W_p \quad (2.58)$$

and let the SVD of ξ be given by

$$\xi = [U_1 \quad U_2] \begin{bmatrix} \Sigma_1 & 0 \\ 0 & 0 \end{bmatrix} \begin{bmatrix} V_1^T \\ V_2^T \end{bmatrix} = U_1 \Sigma_1 V_1^T. \quad (2.59)$$

Then recalling the results of the equation (2.14) we have the following:

$$n = \dim(\Sigma_1) \quad (2.60a)$$

$$\xi = \mathcal{O}_k X_f \in \mathbb{R}^{kp \times N} \quad (2.60b)$$

$$\mathcal{O}_k = U_1 \Sigma_1^{\frac{1}{2}} T \in \mathbb{R}^{kp \times n}, \quad |T| \neq 0 \quad (2.60c)$$

$$X_f = T^{-1} \Sigma_1^{\frac{1}{2}} V_1^T \in \mathbb{R}^{n \times N}. \quad (2.60d)$$

The estimates of the matrices A and C can be obtained from the extended observability matrix. We have also that:

$$\Phi_k = (R_{31} - R_{32} R_{22}^\dagger R_{21}) R_{11}^{-1} \quad (2.61)$$

hence from the definition of Φ_k

$$\begin{bmatrix} D & 0 & \cdots & 0 \\ CB & D & \cdots & 0 \\ \vdots & \vdots & \ddots & \vdots \\ CA^{k-2}B & CA^{k-3}B & \cdots & D \end{bmatrix} = (R_{31} - R_{32} R_{22}^\dagger R_{21}) R_{11}^{-1} \quad (2.62)$$

so that we can apply the same method used in the MOESP algorithm to compute the estimates of D, B . Using the estimate of the state vector given by the relation (2.60d), we can write:

$$\hat{X}_{k+1} = [x(k) \quad x(k+1) \quad \cdots \quad x(k+N-2) \quad x(k+N-1)]. \quad (2.63)$$

We define the following matrices with $N-1$ columns:

$$\bar{X}_{k+1} = [x(k+1) \ \cdots \ x(k+N-1)] \quad (2.64a)$$

$$\bar{X}_k = [x(k) \ \cdots \ x(k+N-2)] \quad (2.64b)$$

$$\bar{U}_{k|k} = [u(k) \ \cdots \ u(k+N-2)] \quad (2.64c)$$

$$\bar{Y}_{k|k} = [y(k) \ \cdots \ y(k+N-2)]. \quad (2.64d)$$

Then it follows that:

$$\begin{bmatrix} \bar{X}_{k+1} \\ \bar{Y}_{k|k} \end{bmatrix} = \begin{bmatrix} A & B \\ C & D \end{bmatrix} \begin{bmatrix} \bar{X}_k \\ \bar{U}_{k|k} \end{bmatrix}. \quad (2.65)$$

This is a system of linear equations for the system matrices that can be solved with the least square method:

$$\begin{bmatrix} \hat{A} & \hat{B} \\ \hat{C} & \hat{D} \end{bmatrix} = \left(\begin{bmatrix} \bar{X}_{k+1} \\ \bar{Y}_{k|k} \end{bmatrix} \begin{bmatrix} \bar{X}_k \\ \bar{U}_{k|k} \end{bmatrix}^T \right) \left(\begin{bmatrix} \bar{X}_k \\ \bar{U}_{k|k} \end{bmatrix} \begin{bmatrix} \bar{X}_k \\ \bar{U}_{k|k} \end{bmatrix}^T \right)^{-1}. \quad (2.66)$$

Summarizing we have the following algorithm:

- compute the LQ decomposition as in equation (2.52) and calculate ξ from equation (2.58);
- compute the state vector as defined in (2.60d) X_k and define \hat{X}_{k+1} , \hat{X}_k , $\hat{Y}_{k|k}$, $\hat{U}_{k|k}$ as in equation (2.64);
- compute the matrices A , B , C , D by solving the regression equation (2.65) using the least square method.

2.6 Implementation of subspace identification algorithms in Matlab

The software chosen to estimate the state space model using the input-output data is Matlab. A short overview on the implementation of subspace methods is given here.

2.6.1 System Identification Toolbox

The System Identification toolbox provides Matlab functions and Simulink blocks to construct mathematical models of dynamic systems from measured input-output data [9]. The estimation can be performed both using time-domain data and frequency-domain data. The algorithm implemented to perform the state space model estimation is the *n4sid* algorithm.

In the case of this work study the problem is to build a global discrete state space model using different experiments in which only one actuator per time was excited. To do this an iterative method that allows to update at each step the current information available with the information given by the next experiment is needed. In this toolbox there is not such a functionality that is why another toolbox has been preferred

2.6.2 SMI (Subspace Model Identification) Toolbox

The SMI toolbox was developed by Delft University and consists of functions for the implementation of the subspace identification algorithms [5]. Particularly the PO-MOESP and PI-MOESP algorithms are implemented.

For both the algorithms the identification is divided into three steps:

- estimation of A and C (and K for the PO-MOESP algorithm);
- estimation of B and D ;
- estimation of the initial state x_0 .

This toolbox allows to build models iteratively starting from different experiments. In fact, the available data consist of different experiments in which only one actuator was excited and all the signals of the accelerometer were saved. The identification is hence performed, by feeding the algorithm with all the output signals of the current experiment, the input signals and the current estimation of the matrix R coming

from the QR decomposition as seen before. The samples are used to build the data Hankel matrices while the estimation of the R matrix is updated at each step with the new data. The size of the data matrices is defined by the number of samples and the input parameter s . This parameter should be chosen larger than the expected system order, although the optimal value has to be found by trial. Particularly it influences the time horizon of the model and consequently also the frequency response of the model. In particular, with a small value of this parameter the frequency response of the model might result inaccurate at low frequencies.

When all the data batches have been used and the order of the system has been chosen, the matrices A and C (and also the K matrix when using the PO-MOESP) can be calculated. A similar iterative procedure is used for the second step of the estimation. Finally the estimation of the initial state vector is performed using the estimated matrices of the system. The estimation of the initial state does not require an iterative procedure. The identification of the model under study was carried out with the PO-MOESP algorithm.

Chapter 3

Estimation of the model

In this chapter the procedures used to identify a global model are explained, presenting the underlying reasonings and the obtained results. A preliminary analysis was performed by estimating some SISO models in order to check the properties of the system. Then different global models were estimated using different techniques in order to improve the results.

3.1 Excitation signals

The first thing to do was to choose the type of excitation signal for the identification step. For this kind of problems typically frequency rich signals are used. Among these, there are the chirp (or sweep) signals and noise signals.

A chirp signal is a periodic signal whose frequency changes with time. A linear sinusoidal chirp signal is given by eq. (3.1)

$$y(t) = \sin[\phi_0 + 2\pi(f_0t + \frac{k}{2}t^2)] \quad (3.1)$$

where $k = \frac{f_1-f_0}{t_1}$ is the rate at which the frequency increases. With this type of signal, the frequency variation must be very slow (less than 10 Hz per second) hence the simulation requires a lot of time. Being the frequency range significantly big (from 1500 Hz to 5000 Hz approximately) and having a huge number of actuators this solution is infeasible due to the limitations of the acquisition system.

The other type of signals used for identification purposes are random noise signals. Different kinds of such signals exist, the most used of which is the white gaussian random noise which has a normal distribution. However in this work a uniform white noise signal, that has a uniform distribution, was used to overcome some practical

problems: in this way we are sure that no sample of the excitation signal generated via software exceeds the output voltage range of the device.

The experiments were performed by exciting each time a single actuator and recording the signals of all the sensors.

3.2 Analysis of the data

The data showed some interesting facts. First of all, all the outputs have small amplitudes (1 V maximum), compared to the amplitude of the excitation signal ($\pm 7.5V$), especially the ones resulting from the experiments in which the actuators on the rear struts were excited. This happens because the path that the mechanical wave has to cover is longer than in the case of an actuator on the anti-torque plate. This is especially true for the sensors located at the physical attachments of the anti-torque plate (A1, A2, A10, A11). On the contrary, for the accelerometers located at the physical attachments of the rear struts (A9 and A18), the amplitudes are very similar. An example of these situations is given in Figure 3.2. For the same reason when an actuator on the right or left side is excited, the signals measured with the sensors on the same side have generally bigger amplitudes than the ones measured at the opposite side. An example is given in Figure 3.1.

The amplitudes of the output signals in some cases might be comparable to the noise so that the identification procedure for the specific input-output channel becomes difficult.

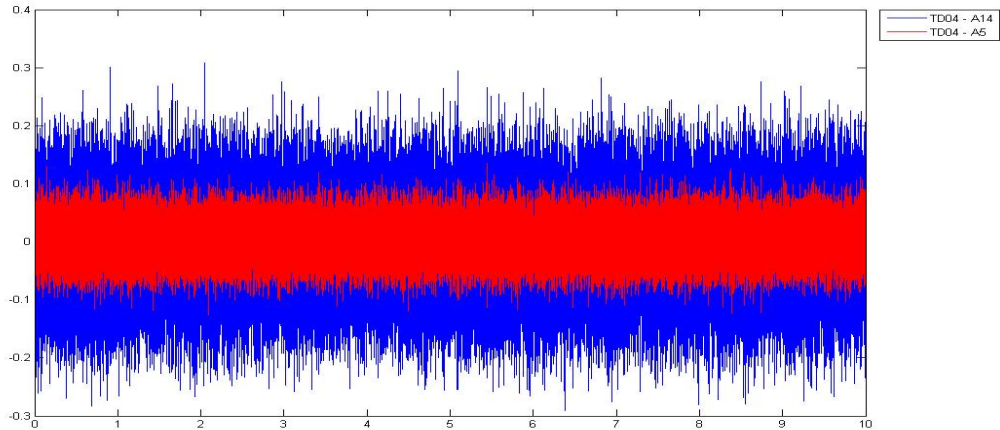
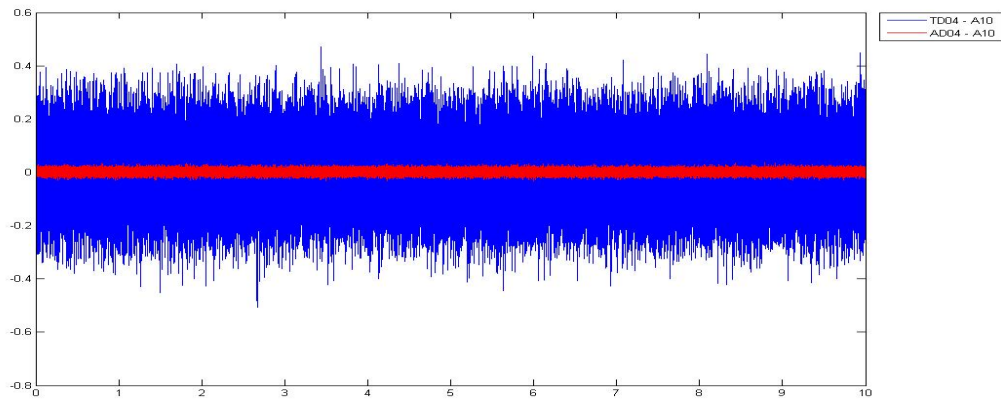
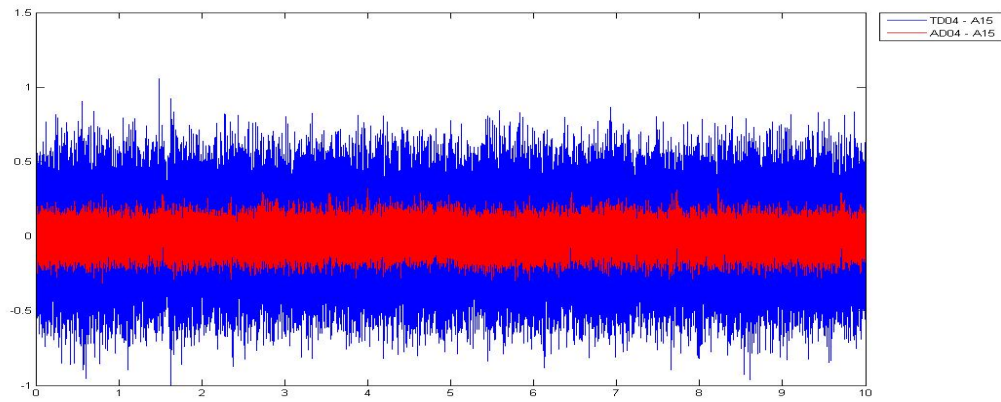


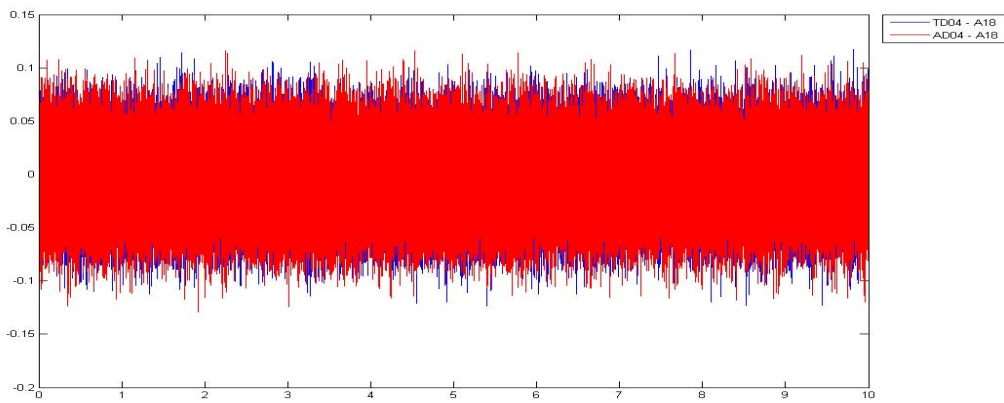
Figure 3.1: Data acquired at sensors A5 (in red) and A14 (in blue) when the actuator TD04 is excited.



(a) Accelerometer 10



(b) Accelerometer 15



(c) Accelerometer 18

Figure 3.2: Data acquired at the same sensors when the actuators TD04 (in blue) and AD04 (in red) are excited.

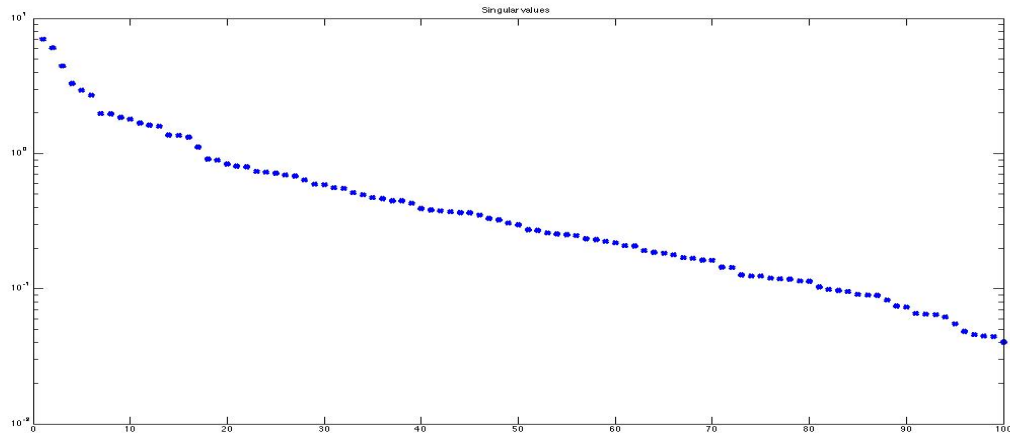


Figure 3.3: Plot of singular values of the SISO model having as input the actuator AD01 and as output the accelerometer 18. Note that there is not any clear gap between the singular values.

3.3 SISO models identified with the Subspace Model Identification Toolbox

Some SISO models having as input an actuator on the rear struts and as outputs the accelerometers on the same side, were estimated with the PO-MOESP algorithm implemented in the Subspace Model Identification (SMI) Toolbox. The models were estimated by letting the order vary from 1 to 50. The number of samples used for the identification step is 30000 and the same number of samples was used for the validation step.

3.3.1 Selection of the model order

The order selection procedure described in Chapter 2 is not always reliable due to the lack of a clear gap in the plot of the singular values. This happens also in our case, as shown in Figure 3.3.

For this reason, another procedure was adopted to select the order: the simulation errors were calculated and plotted for varying model orders. As the model order increases, the simulation error becomes smaller. When the simulation error stops decreasing significantly for high values of the order or it is considered sufficiently small, then the order is selected arbitrarily by the user. The metric used to calculate the simulation error is the *variance accounted for (vaf)* defined in equation (3.2):

$$vaf = \left(1 - \frac{\text{var}(e)}{\text{var}(y)}\right) 100 \quad (3.2)$$

where e is the error obtained by simulating the model using the excitation signal of the experiment and calculating the difference between the simulated output and the true output; y in the formula stands for the measured output. This metric is a sort of percentage measure: if the model is a perfect representation of the system, the simulation error is zero and its variance is zero too so that the value of the *variance accounted for* is 100. When the estimation is not good, the variance of the error increases while the *vaf* value decreases and it can assume also negative values. Of course the identification process and the validation process must be performed on different portions of data.

Some plots of the simulation error for the actuators on the right rear strut and the accelerometers on the right side are shown in Figure 3.4. It is possible to notice how for some models a low order can be selected since their performances are really good, while some others need a higher order. However note that the performances of the SISO models are really good, especially considering that the output signals obtained by exciting the actuators on the rear struts have small amplitudes, and for an order between 15 and 20 all of them have a *vaf* value higher than 70.

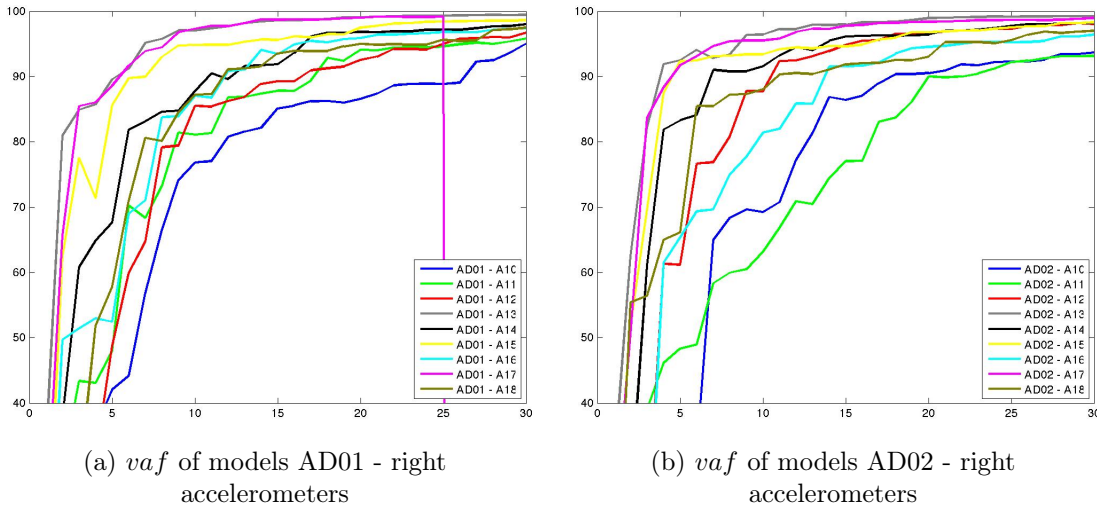


Figure 3.4: Simulation errors in terms of the *vaf* criterion calculated for varying model orders for the SISO models having as input an actuator on the right strut and as output an accelerometer on the right side.

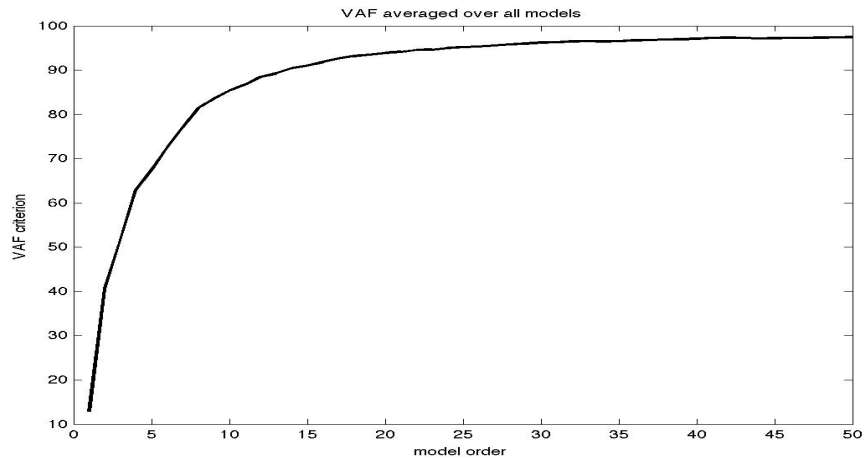


Figure 3.5: Simulation errors in terms of the *vaf* criterion calculated for varying models orders averaged on stable SISO models having as input an actuator on the right strut and as output an accelerometer on the right side.

Figure 3.5 reports the average *vaf* over the stable models having as input an actuator on the right rear strut and as output an accelerometer on the right side.

Looking at these figures, the order for these models was selected to 19. A stability analysis was performed to be sure that for the chosen order, all the models were stable.

To validate this choice, the frequency responses of the models were compared to the frequency responses calculated from the data: some examples are shown in Figure 3.6. As it is possible to notice from the plots, they have the same trend, especially for high frequencies (above 1000 Hz). Note also that for the accelerometer 18, corresponding to the attachment of the right rear strut, the responses are more similar than for the accelerometer 10.

3.3.2 Poles of the models

The poles of the models having the same input were compared to check if they share some common characteristics. Some examples are given in Figure 3.7. The same was performed for the models sharing the same input and having different outputs (Figure 3.8). In both cases it is possible to notice that only few poles are clustered and most of them are at high frequencies. For this reason, we expect that the frequency responses are significantly different, even for the models sharing an input or an output.

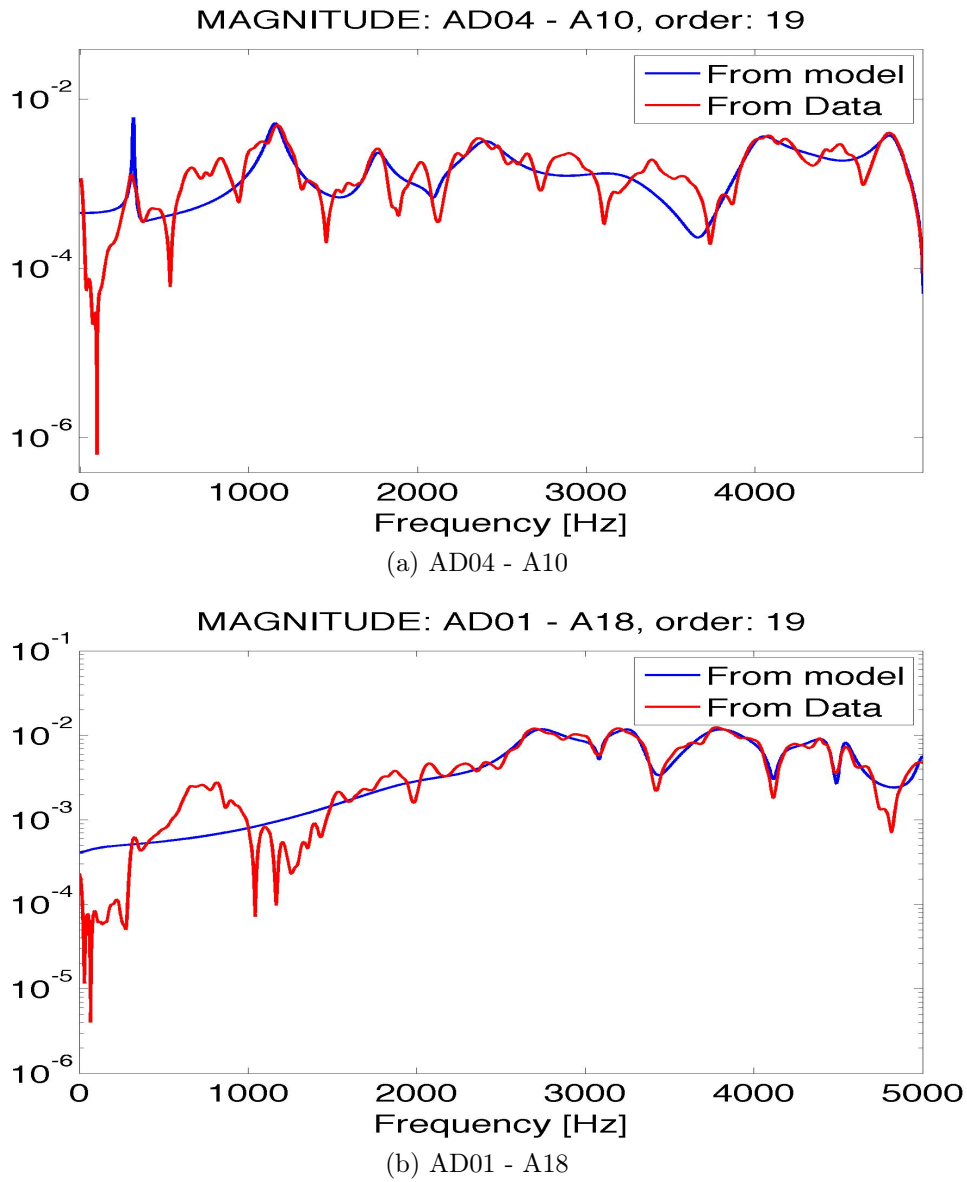


Figure 3.6: Comparison between the frequency responses of some SISO models (in blue) and the frequency responses calculated from the data (in red). The models considered have as inputs the actuators AD01 and AD04, and as outputs the accelerometers 10 and 18.

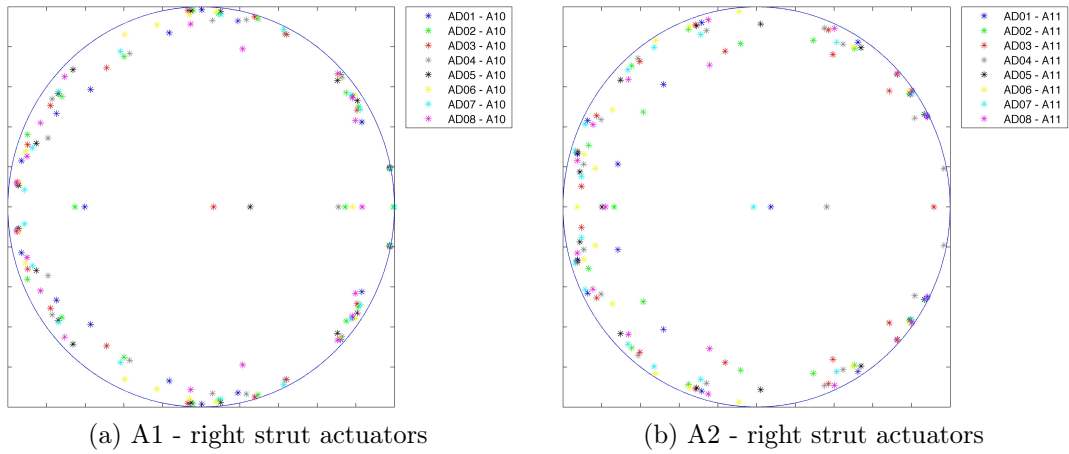


Figure 3.7: Poles of the SISO models having as input an actuator on the right rear strut and as output the same right accelerometers.

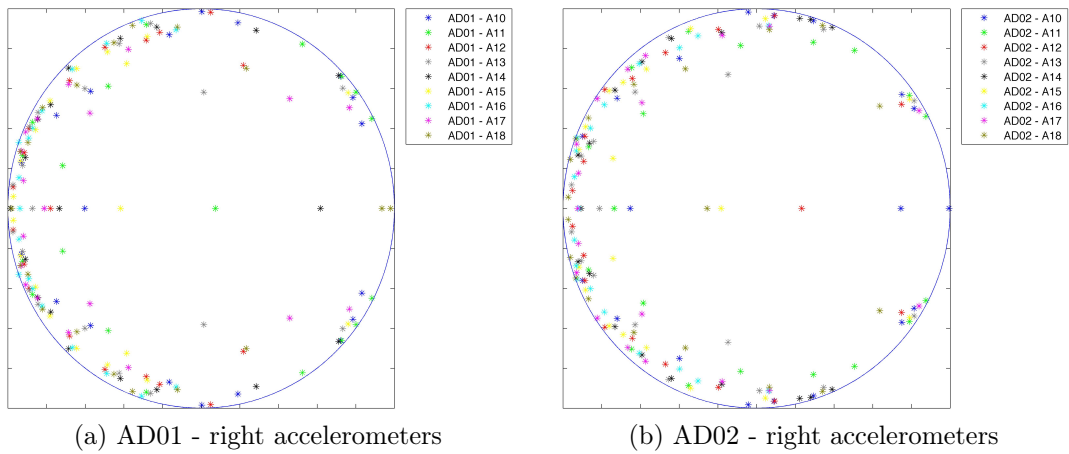
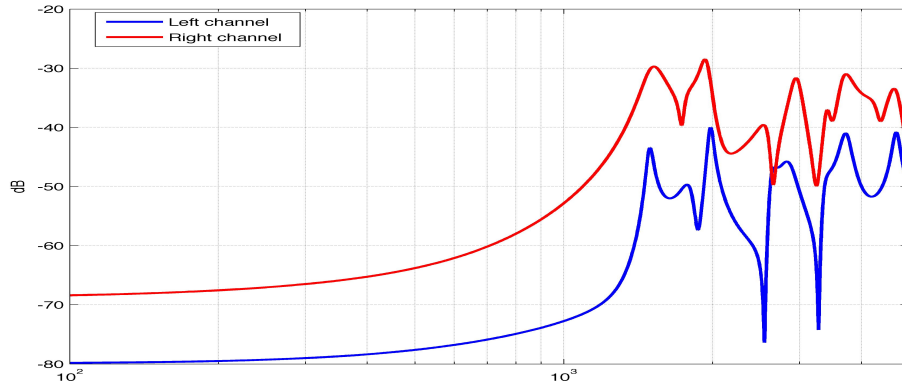


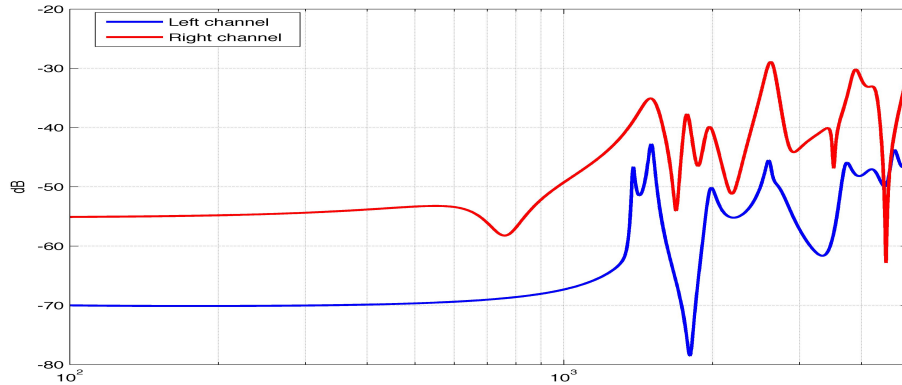
Figure 3.8: Poles of the SISO models having as output an accelerometer on the right side of the cabin and as input the same actuator on the right rear strut.

3.3.3 Frequency response

To check if the system has any property of symmetry the magnitudes of the Bode plots were compared: particularly in each case two SISO models were considered, sharing the same actuator and having as output an accelerometer on the right side of the cabin and the symmetric left accelerometer. An example is shown in Figure 3.9.



(a) TD01 - A2, A11



(b) TD01 - A1, A10

Figure 3.9: Comparison between the magnitudes of the Bode plot for two SISO models having as input the same actuator (TD01) and as output one accelerometer on the right side ((a) A11, (b) A10, in red) and the symmetric left accelerometer ((a) A2, (b) A1, in blue).

Some remarks are in order. First of all the responses are flat for low frequencies and start to grow around 1000 Hz: this depends on the size of the data matrices used for the identification process whose size depends on the chosen number of samples and on the parameter s already discussed in Section 2.6.2. Then there is a strong

attenuation between the left and right accelerometers, as already noted from the data acquired. The two responses tend to have the same shape for middle frequencies and then differ increasingly more for high frequencies. From this analysis it is possible to state that the structure is not symmetric and this can be connected to the intrinsic asymmetry of the rotary system of the helicopter and to the fact that the locations of the accelerometers is not perfectly symmetric. For this reasons, no property of symmetry can be assumed.

3.4 Identification of the global model

Finally, the first attempt to identify a complete model considering all the accelerometers and all the actuators was performed. Being the system so large and its estimation requiring a lot of time, it is not possible to identify the model for varying orders and evaluate each time the simulation error to select the order. However it is still possible to look at the plot of the singular values, shown in Figure 3.10. Again, there is no significant gap in the plot: that is why the order was chosen arbitrarily by keeping the same value used for the identification of the SISO models.

Different estimations were performed using different numbers of samples and different values of the input parameter s (discussed in Section 2.6.2).

The values of the number of samples considered are 10000, 20000, 30000 while the considered values for the parameter s are 50 and 80. Bigger values of both these parameters are not possible due to the limited computing power available. Although the results are quite similar, the best model was the one estimated with 30000 samples and having a value for s equal to 80.

The simulation results in terms of the *vaf* criterion are visually shown in Figures 3.11, 3.12, 3.13 and 3.14 that correspond to the different groups of actuators (the numerical results are shown in Appendix A): the first figure is for the actuators on the left rear strut, the second for the left actuators on the anti-torque plate, the third for the actuators on the right strut and the fourth for the right actuators on the anti-torque plate.

Looking at the results it is possible to notice that the simulation errors are far worse than the ones seen in the cases of the SISO models. The complete model gives best simulation results for the actuators on the anti-torque plate than it does for the actuators on the rear struts, since the corresponding frequency responses have higher amplitudes. As expected, with some exceptions, the simulation errors are smaller when the excited actuator and the accelerometer are on the same side of the cabin. This is because the output signals of the accelerometers on the opposite side are

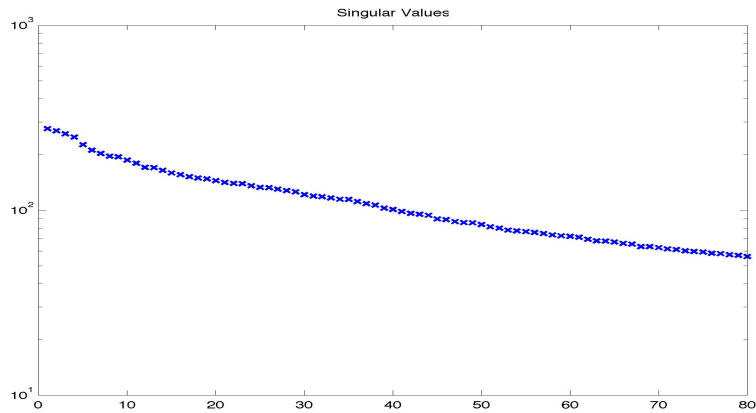


Figure 3.10: Plot of the singular values for the order selection of the global model.

more attenuated.

Another observation is that when e.g. one excites the actuators on the left rear strut, the accelerometer at the rear strut (on the same side of the excited actuator) give better simulation results than the accelerometers of the anti-torque plate (on the same side). On the contrary, when an actuator on the left side of the anti-torque plate is excited, the simulation error is smaller for the accelerometer at the left physical attachment of the anti-torque plate than for the accelerometers at the rear strut on the same side.

The averaged value of the simulation result in terms of the *vaf* criterion is -11 . The negative value is due to the fact that some channels have as simulation results big negative values.

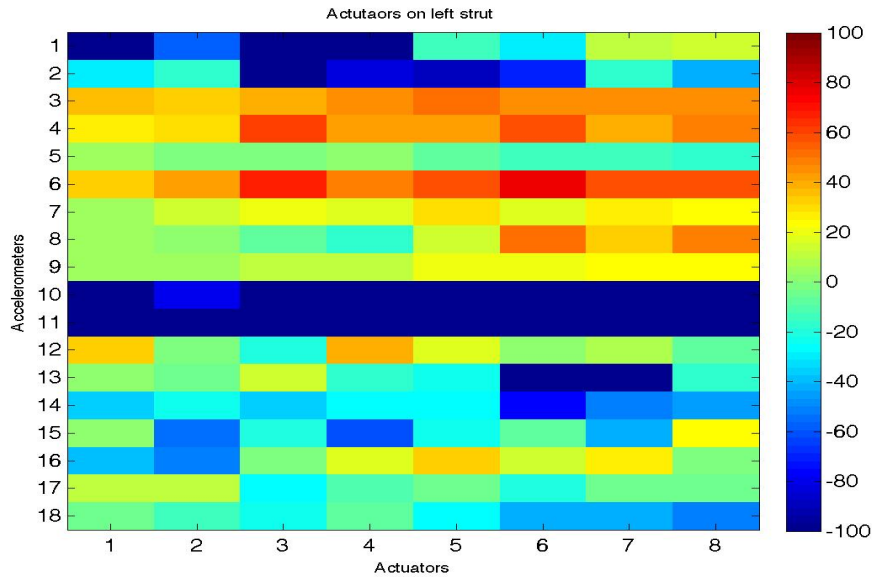


Figure 3.11: Visualisation of the simulation results of the global model for the actuators on the left rear strut in terms of the vaf criterion.

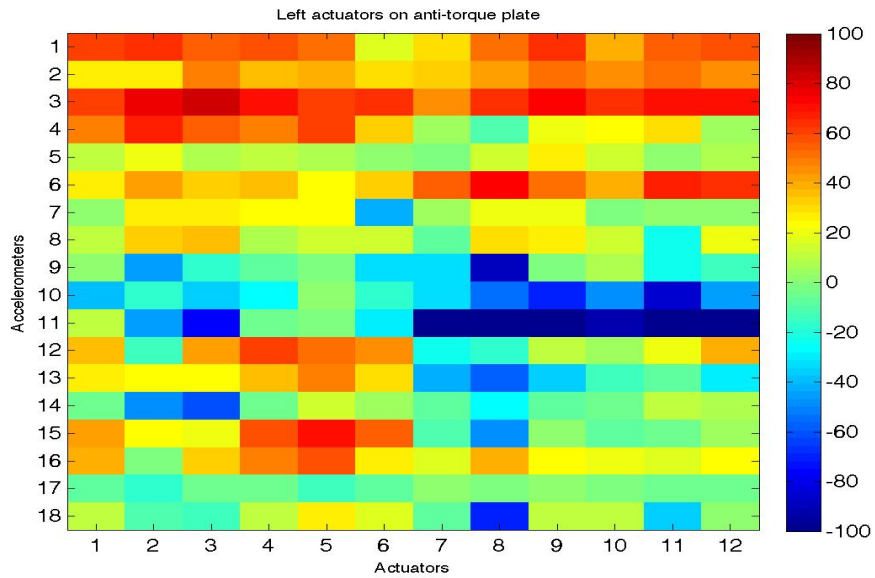


Figure 3.12: Visualisation of the simulation results of the global model for the actuators on the left side of the anti-torque plate in terms of the vaf criterion

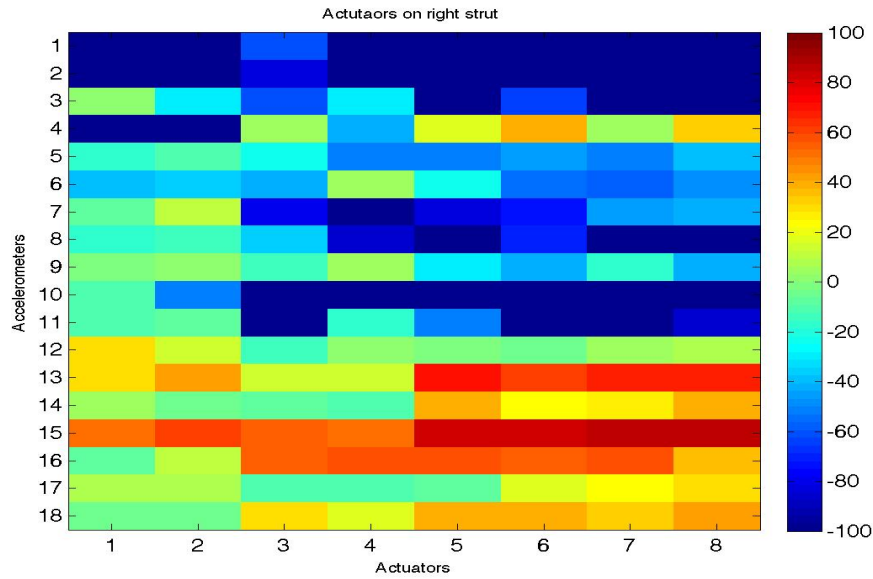


Figure 3.13: Visualisation of the simulation results of the global model for the actuators on the right rear strut in terms of the vaf criterion

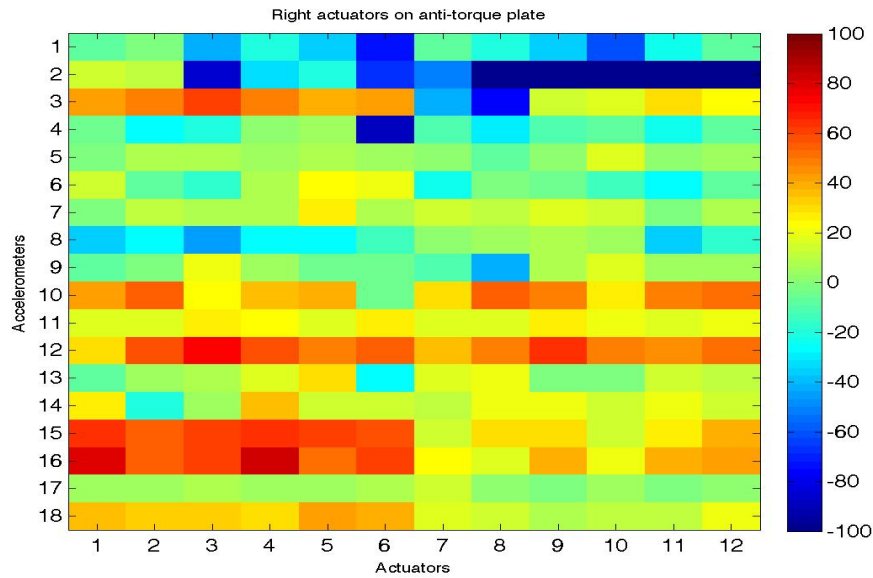


Figure 3.14: Visualisation of the simulation results of the global for the actuators on the right side of the anti-torque plate in terms of the vaf criterion.

3.5 Identification of the global model with normalized measurements

The procedure for the identification of the model is based on the minimization of a sum of squared errors. In the system considered, as seen before, there are some output signals whose amplitudes are significantly bigger than the others. Consider for example the function to be minimized as a sum of two terms as in equation (3.3):

$$E(t) = e_1(t)^2 + e_2(t)^2 \tag{3.3}$$

Now suppose that the average amplitude of $e_1(t)$ is ten times bigger than the amplitude of $e_2(t)$: it is clear that when minimizing $E(t)$, the effort of the algorithm will be put mostly on the minimization of the first squared term, which is 100 times bigger than the second one. That is why a second estimation was performed, with the same setting of the parameters of the previous estimation but with a normalization of the output signals: particularly the output signals were scaled between ± 1 and the identification step was performed on the scaled data. The scaling factors of each input-output channel were memorized in a matrix. When simulating the model, the outputs must be multiplied by the corresponding scaling factor. As done for the previous model, the model was simulated and the results are visually shown in Figures 3.15, 3.16, 3.17 and 3.18 (the numerical results are shown in Appendix B).

The average simulation error in terms of the *vaf* criterion is now around 22, which has improved significantly with respect to the previous case: in fact almost all big negative values have disappeared.

Also in this case the simulation errors are smaller when the excited actuator and the accelerometer are on the same side of the cabin and better simulation results are achieved for the accelerometers located in correspondence of the structural element on which the excited actuator is positioned.

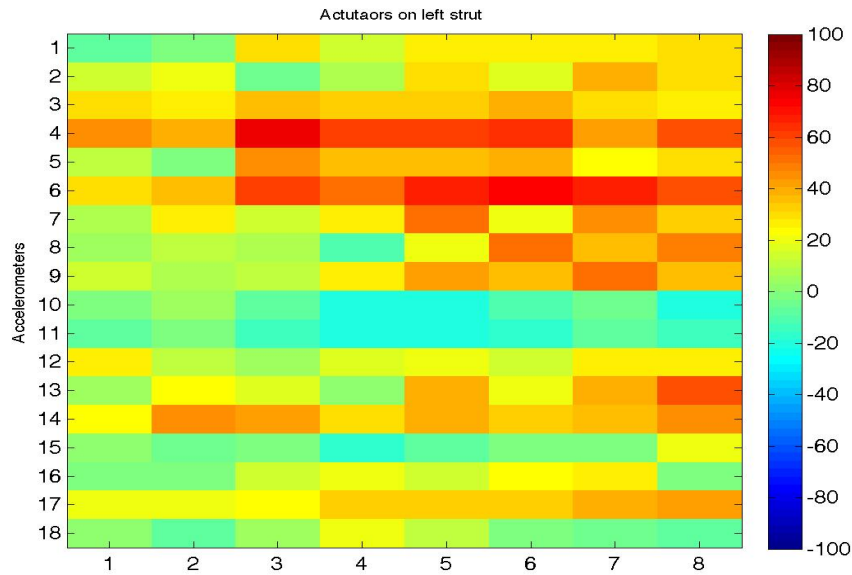


Figure 3.15: Visualisation of the simulation results of the global model estimated after scaling the output signals for the actuators on the left rear strut in terms of the *vaf* criterion.

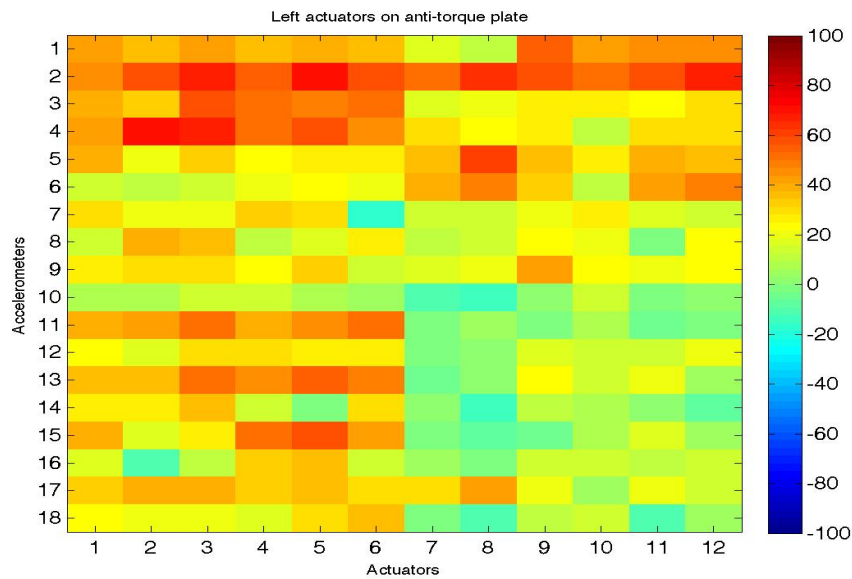


Figure 3.16: Visualisation of the simulation results of the global model estimated after scaling the output signals for the actuators on the left side of the anti-torque plate in terms of the *vaf* criterion.

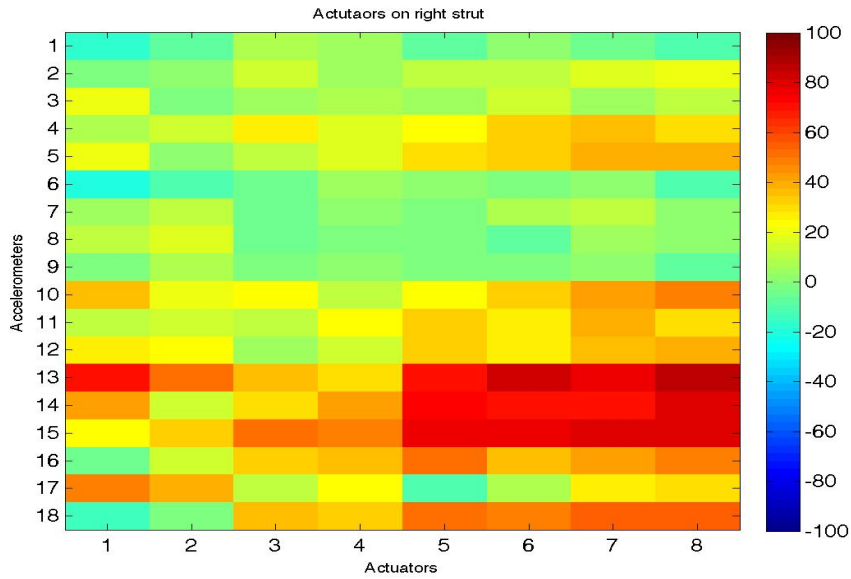


Figure 3.17: Visualisation of the simulation results of the global model estimated after scaling the output signals for the actuators on the right rear strut in terms of the *vaf* criterion.

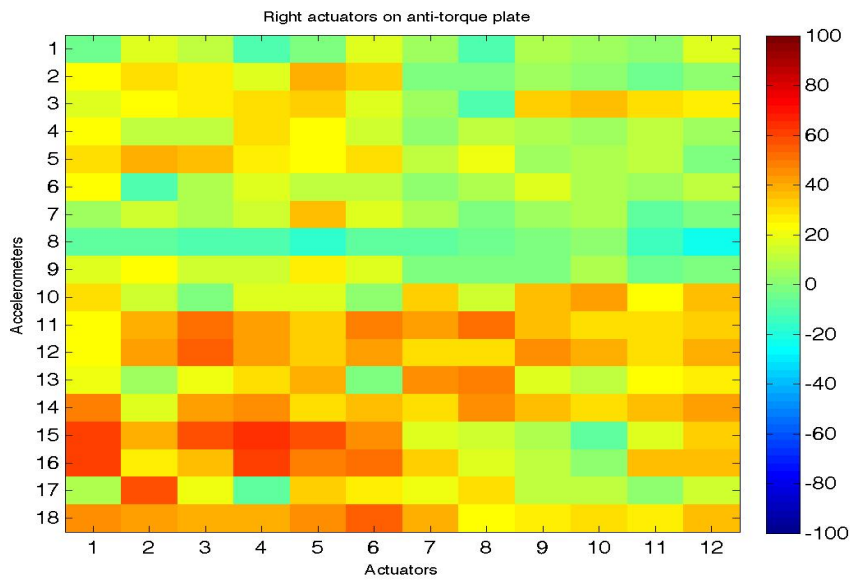


Figure 3.18: Visualisation of the simulation results of the global model estimated after scaling the output signals for the actuators on the right side of the anti-torque plate in terms of the *vaf* criterion.

3.6 Identification of the global model with filtered data

Since the disturbance signal has specific frequency components, the model is required to be precise not at all frequencies but only in a small neighborhood of these frequencies. For this reason, not only were the output data scaled but both input and output signals were filtered. Two possibilities are available: identify a model for each frequency component using many band-pass filters or identify just one model for all the frequency components by filtering the data with a multiband filter. In this case only one frequency of the disturbance has been considered.

As example, an identification of the model in a neighborhood of 1800 Hz was performed. In this case the digital filter used to filter the input and output data is a IIR band-pass filter of bandwidth equal to 100 Hz centered at 1800 Hz. The frequency response of the filter is shown in Figure 3.19. Having reduced the frequency range, the order of the model was also reduced and set to 15 (this was established empirically by identifying some SISO filtered models) and the parameter s was set to 80. The number of samples used for the identification step was kept the same. The simulation results of the model are visually shown in Figures 3.20, 3.21, 3.22 and 3.23 (the numerical results are shown in Appendix C).

As one can see, the results have greatly improved and now the average value of the simulation error in terms of the vaf criterion is 48. Only few negative values are present and the simulation errors are small even when the accelerometers and actuators are on opposite side of the cabin.

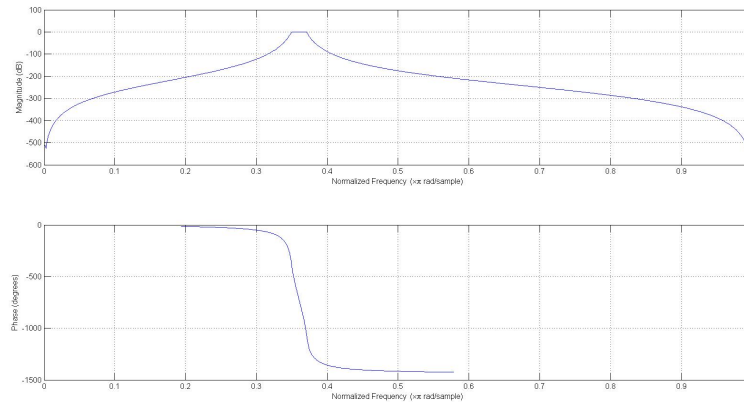


Figure 3.19: Frequency response of the filter used to filter the data.

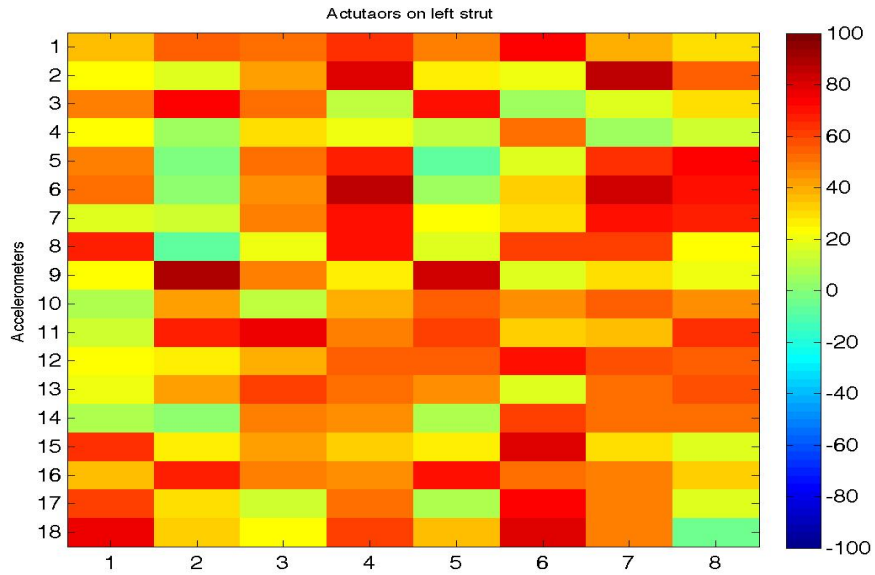


Figure 3.20: Visualisation of the simulation results of the global model estimated after scaling and filtering the signals for the actuators on the left rear strut in terms of the *vaf* criterion.

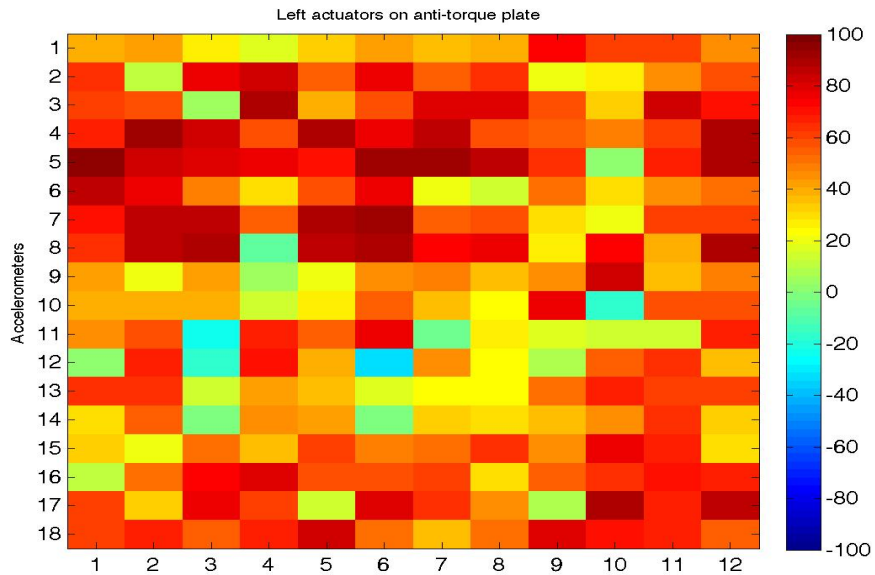


Figure 3.21: Visualisation of the simulation results of the global model estimated after scaling and filtering the signals for the actuators on the right side of the anti-torque plate in terms of the *vaf* criterion.

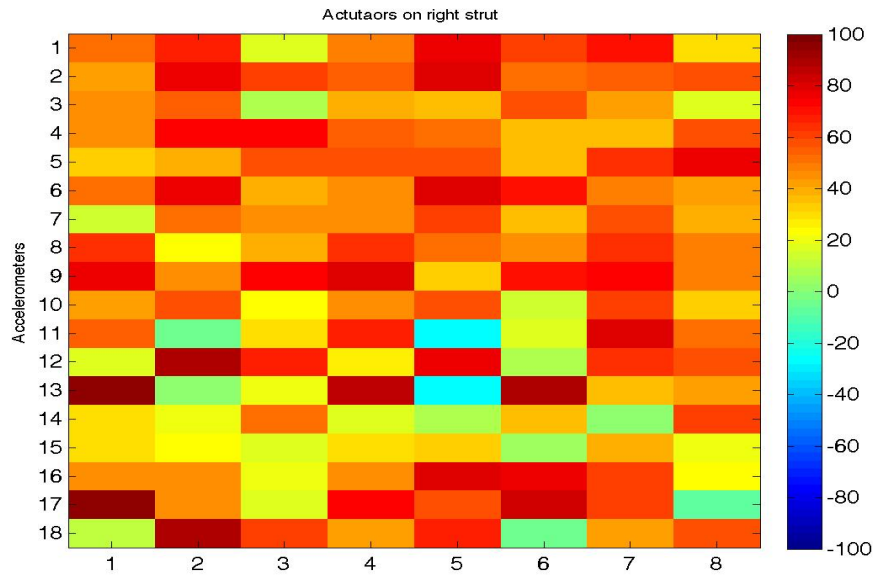


Figure 3.22: Visualisation of the simulation results of the global model estimated after scaling and filtering the signals for the actuators on the right rear strut in terms of the *vaf* criterion.

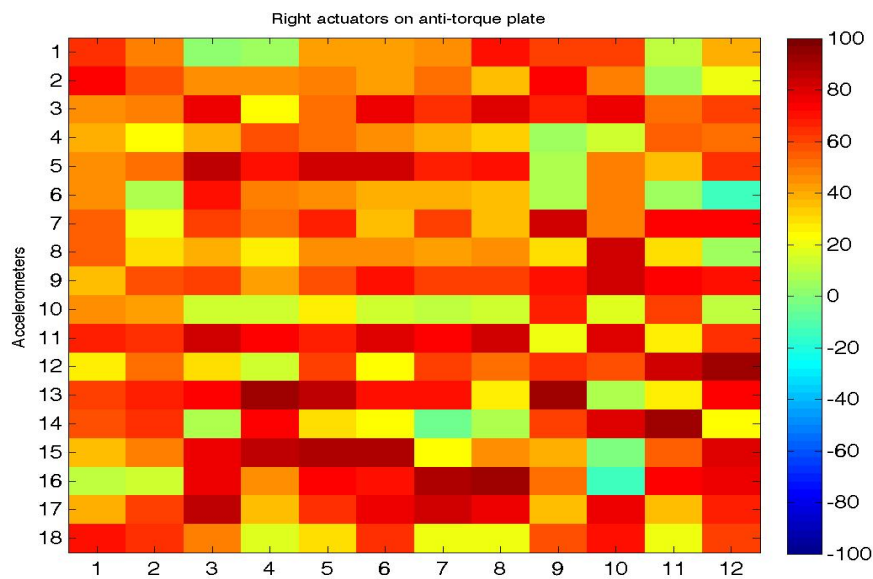
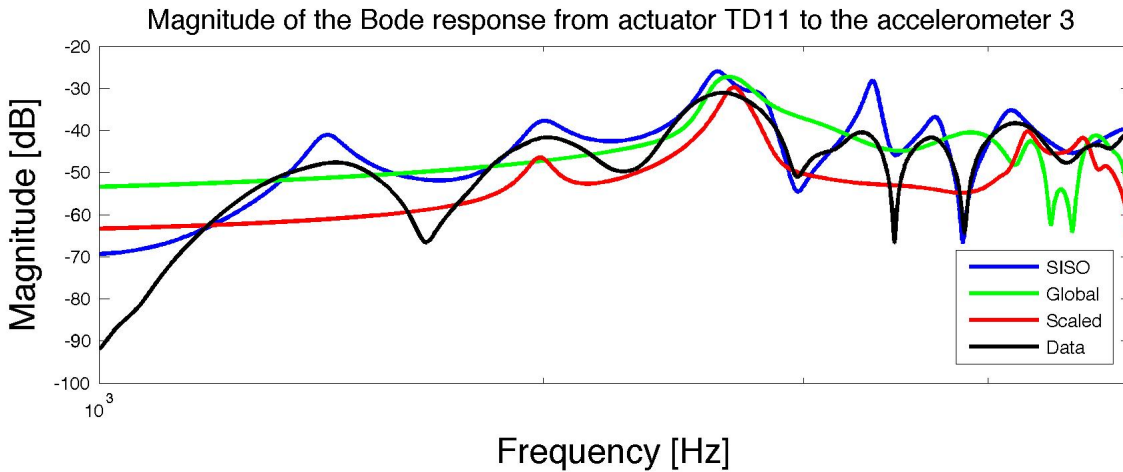


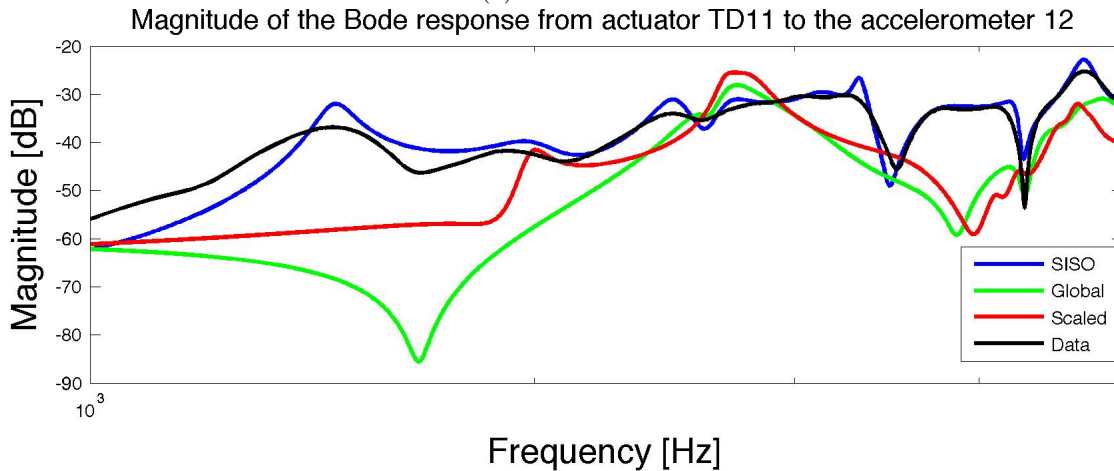
Figure 3.23: Visualisation of the simulation results of the global model estimated after scaling and filtering the signals for the actuators on the right side of the anti-torque plate in terms of the *vaf* criterion.

3.7 Comparison between the frequency responses of the global models and the SISO models

A comparison among the frequency responses calculated from the data, the frequency responses of the global model estimated directly from the data, the global model estimated with the normalization procedure and the corresponding SISO models was performed: an example is given in Figure 3.24. As one can notice, although the curves have the same trend, they are significantly different and this is especially true when the actuator and the accelerometer are on opposite sides. In fact in this case, due to the lower amplitudes of the signals, the global models are more inaccurate. Another important thing to notice is that all the responses are flat for low frequencies but the one corresponding to the SISO model starts to grow earlier than the ones of the global models: this is due to the choice of the input parameters used for the identification. Note also how the frequency response of the SISO model is very similar to the one calculated from the data when the accelerometer is on the same side of the excited actuator (Figure 3.24b). On the contrary, when the accelerometer is on the opposite side of the cabin (Figure 3.24a), even the frequency response of the SISO model tends to differ from the one calculated from data.



(a) TD11 - A3



(b) TD11-A12

Figure 3.24: The figure shows a comparison among the frequency responses of the global model estimated directly from data (in green), the global model estimated with the normalization procedure (in red) and the SISO model (in blue) for the input-output channel TS04-A2. Also the magnitude of the frequency response calculated from data is shown (in black).

Chapter 4

Control design

In this chapter the definitions of some general control techniques are recalled, pointing out the advantages and disadvantages of each one and discussing them in relation to the system. Particularly the techniques compared are feedforward versus feedback and centralized versus decentralized control. Then the motivations that led us to the choice of a decentralized control are discussed and some algorithms present in literature to obtain such a control are explained with particular emphasis on the Relative Gain Array algorithm and the SVD algorithm. Finally, the results of a simulation study are illustrated.

4.1 Definition of a controller

A controller is a dynamic system that generates the signals to pilot the actuators in order to control a given plant. A control system consists generally of three components:

- the physical system consisting of a set of actuators and sensors, the anti-aliasing filters, the DAC and ADC components and the power amplifier;
- an algorithm that is used to take decisions depending on the signals measured at the sensors according to the minimization of a cost function (the actual control law);
- a computer that performs the calculation.

In some applications also a previous knowledge of the plant to be controlled is needed. Different types of controllers exist in literature depending on the specific applications.

In the following two categories of control techniques are discussed in relation to the system under study.

4.1.1 Feedforward versus feedback disturbance attenuation

Feedforward and feedback control systems are two different methods employed in control theory in order to attenuate an undesired disturbance acting on the output. The difference between the two methods relies on the way the control signal is generated [12].

Consider a SISO system for simplicity. The former technique relies in the possibility to measure a reference signal strongly correlated to the primary disturbance acting on the plant. Based on this signal, and on the residual error signal measured at the error sensor, the coefficients of an adaptive filter are calculated according to a least mean square procedure. Using the reference signal, the adaptive filter generates the signal that, after being converted to the continuous domain, drives the secondary source. The secondary source converts the electrical signal to a mechanical wave that sums up with the primary disturbance at the error sensor, resulting in a destructive interference. The limiting condition of this technique is generally that the reference signal must be highly correlated with the primary noise and when using acoustic sensors such as microphones, the problem of acoustic feedback from the secondary source to the reference microphone can arise. A scheme of a feedforward system applied for noise reduction in helicopters is shown in Figure 4.1.

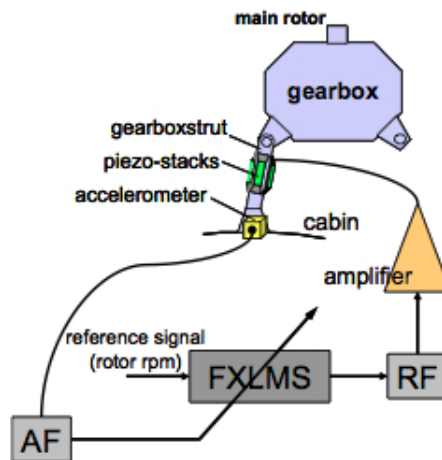


Figure 4.1: Example of a feedforward control scheme [3]

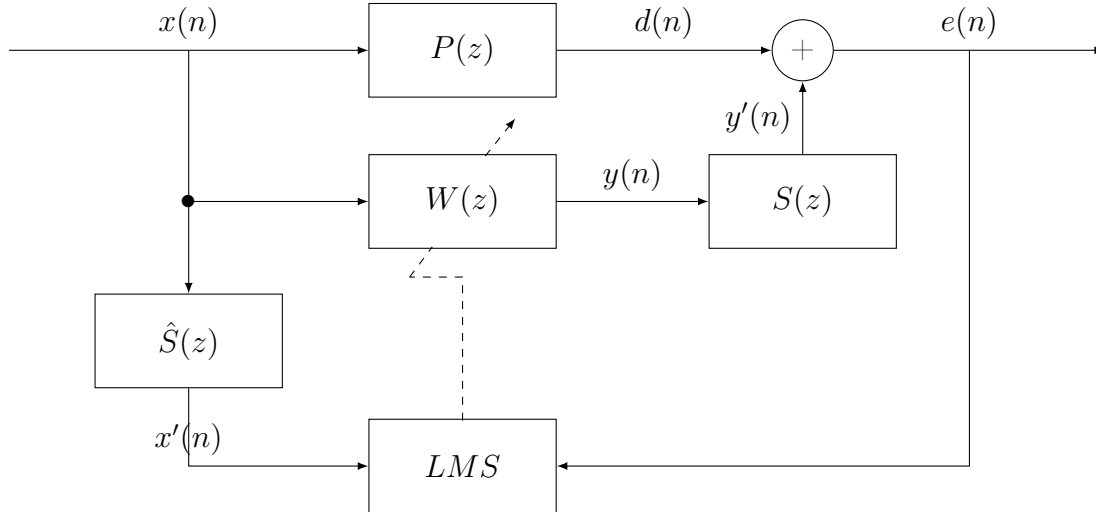


Figure 4.2: FxLMS feedforward control scheme.

One of the most common feedforward control technique, especially used for broadband active noise control applications, is the FxLMS algorithm whose block diagram is shown in Figure 4.2. The adaptive filter is indicated as $W(z)$ in the block diagram. The filter $P(z)$ represents the unknown primary path that is the relationship between the disturbance signal measured at the reference sensor and the disturbance acting on the error sensor. The secondary path $S(z)$ represents the relationship between the control signal and the mechanical wave produced at the summing junction and includes the D/A converter, the reconstruction filter, the power amplifier, the mechanical path from the secondary source to the summing junction and from the summing junction to the error microphone, the error microphone, the anti-aliasing filter and the D/A converter. $\hat{S}(z)$ is an estimate of the dynamics of the secondary path, introduced to compensate the intrinsic delay between the error signal $e(n)$ and the reference signal $x(n)$.

In a feedback system the control signal is derived in a different way: the error signal is processed in order to attenuate the residual effects of the disturbance. In such a configuration no reference signal is required, so that we have one less sensor and consequently the problem of acoustic feedback is eliminated.

When there is the possibility to have a reference signal, a feedforward system is generally preferred because of its potentially superior performance. However feedback systems are simpler to implement, that is why they are often used for noise and vibration attenuation applications. Another advantage of feedback systems is that they do not require the estimate of the dynamics of the secondary path. A general

block diagram of feedback control is shown in Figure 4.3, with the following notation:

- the System block represents the plant to be controlled, consisting of p outputs and m inputs;
- $r \in \mathbb{R}^m$: is the reference signal vector or in other words the constant values we want the measured signals to assume. We are dealing with the attenuation of vibrations so ideally r is a zero vector of length equal to the number of outputs;
- $u(n) \in \mathbb{R}^m$ is the control signal vector, the signals to be applied to the secondary sources so that the measured signals assume a value close to the reference vector;
- $y(n) \in \mathbb{R}^p$ are the output signals, or in other words the signals generated by the system when the inputs $u(n)$ are applied to the secondary sources;
- $d(n) \in \mathbb{R}^p$ are the disturbances acting on the sensors and that get summed with the outputs of the system;
- $e(n) \in \mathbb{R}^p$ are the residual errors or the measured signals, given by the sum of the disturbance signals with the output signals of the system;
- the Regulator is the system with p inputs and m outputs that, based on the measurements and on a control law, generates the control signals to be applied to the system in order to have as measured outputs constant signals close to the reference signals r .

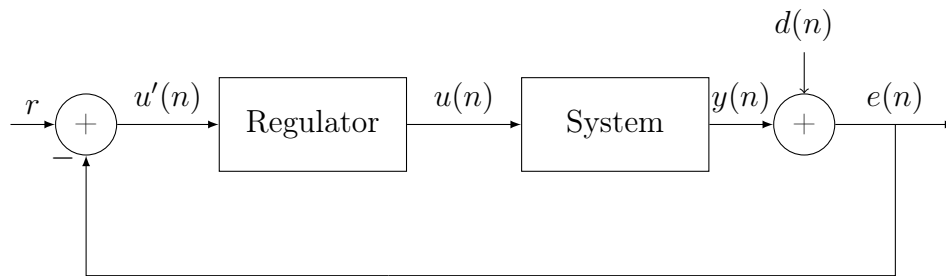


Figure 4.3: General block diagram of a feedback system.

As far as regarding our system the choice is to use a feedback system although in a rotorcraft the measurement of a signal strongly correlated with the periodic disturbance is not a problem. The choice was due to the simplicity since in the feedback problem no estimation of the secondary paths is needed.

4.1.2 Centralized versus decentralized control

When a system has more than one inputs and outputs the so called cross-talking phenomena arises. Basically in such cases each input affects each output so that it is not possible to design one controller for each input-output channel independently. If this is done then an actuator, used only to control the disturbance acting on a specific sensor, has some effects also on the other sensors controlled by other actuators, for which this signal is a disturbance to be attenuated.

The only case when this type of control, called decentralized control, can be applied to a MIMO system is when the transfer function matrix for the system is almost diagonal: in this case, considering for example a square system, the signal generated by an actuator has a significant effect only for an output so that it is possible to design different independent controllers for each input-output channel. Such a condition is desirable since it simplifies the multichannel system to many SISO systems that can be more easily controlled.

When this does not hold, then a centralized control must be adopted, meaning that the procedure to generate the control signals takes into account all the output signals. Such control laws are not easy to design and their complexity grows exponentially with the number of channels. For this reason some techniques have been developed to simplify a multichannel system so that many independent decentralized controllers can be employed to control the given plant.

In our case it is obvious that the design of a centralized control is too difficult due to the large number of channels. For this reason some ways to simplify the system were analysed. In the following sections some techniques used to deal with such systems are discussed. Particularly they aim at transforming a MIMO system to an equivalent one on which a decentralized control approach can be applied: this procedure is commonly referred as decoupling control and it allows to have an equivalent diagonal system.

4.2 Diagonalization

When the system has too many inputs and outputs a centralized controller becomes too difficult to be designed so that other methods are employed. Diagonalization is a way of transforming a non-diagonal multi channel system to a diagonal one. This is typically done by pairing, if the system is square, each input to an output. The assumption is that the majority of the effect of an input is mainly just on one sensor so that the effects on the other sensors can be completely neglected.

4.2.1 Relative Gain Array

One of the diagonalization technique is the Relative Gain array [15]. Consider a square multivariable process: the relative gain $\lambda_{i,j}$ between a controlled variable y_i and a manipulated variable u_j is defined as a dimensionless ratio of two steady state gains:

$$\lambda_{i,j} = \frac{\left(\frac{\partial y_i}{\partial u_j}\right)_{u_k=0, k \neq j}}{\left(\frac{\partial y_i}{\partial u_j}\right)_{y_k=0, k \neq i}} \quad (4.1)$$

where the numerator is called open-loop gain and it is evaluated by keeping all the manipulated variables constant except u_j . On the contrary the denominator is called closed-loop gain and it is evaluated with all the controlled variables except y_i maintained to the set-point. Defining G as the steady state response of the square system, the *RGA* can be easily calculated with the equation (4.2):

$$\Lambda = G \odot (G^{-1})^T \quad (4.2)$$

where the symbol \odot indicates element by element multiplication. The *RGA* matrix gives information on how to pair each input with an output in order to obtain the best possible diagonal system. The pairing rules are the following:

- select input-ouput pairings that results with an element close to 1;
- avoid pairing negative elements;
- large *RGA* elements are not appropriate for input-output pairings.

Then the system must be reorganized to obtain an almost diagonal matrix; the *RGA* of the redefined system in this way is close to the identity matrix. After that the pairings have been performed then it is like having many independent SISO systems for which the controllers can be designed independently. However such method can be employed only if each input has effects only on one output and vice versa. Even in this case, there are nevertheless some problems: considering especially our system, we are interested in some specific frequencies that are far from the steady state and the transfer functions can vary a lot in the frequency range. This problem is solved by the Dynamic Relative Gain Array (DRGA), that is calculated in a similar manner of equation (4.2); now the matrix G is the frequency response of the system calculated at the considered frequency. The pairing rule is now the following:

- the pairing should be such that, over the frequency range of interest, the magnitude of the diagonal elements is close to one and the magnitude of the off diagonal elements is small [1].

Also an extension of the RGA in order to deal with non-square plants exists and it is called the Non-Square Relative Gain Array (NSRGA) which works exactly in the same way.

A dynamic non-squared RGA analysis was performed to the system and it showed that a pairing between input and outputs can not be performed, due to the large number of off-diagonal elements.

4.2.2 Singular Values Decomposition

The SVD (singular value decomposition) is a matrix decomposition algorithm that allows to express a rectangular matrix A as a product of three matrices:

$$A = U\Sigma V^H \quad (4.3)$$

where V^H is the Hermitian of the matrix V since the SVD algorithm can be also applied to complex matrices. If matrix A is real then the Hermitian simplifies to the transpose. Considering the so called economy SVD, if $A \in \mathbb{C}^{p \times m}$ with $m > p$ then $\Sigma \in \mathbb{R}^{+p \times p}$ is a non-negative diagonal matrix, $U \in \mathbb{C}^{p \times p}$ is a unitary matrix, $V \in \mathbb{C}^{m \times p}$ is a unitary matrix too. On the contrary, if $p > m$ then $\Sigma \in \mathbb{R}^{+m \times m}$ is still diagonal, $U \in \mathbb{C}^{p \times m}$ is a unitary matrix, $V \in \mathbb{C}^{m \times m}$ is also a unitary matrix. In the easiest case, when $m = p$, all the matrices are square and have the same dimensions. The columns of U are called left singular vectors, the columns of V are called the right singular vectors and the elements of Σ that are in decreasing order so that $\sigma_1 \geq \sigma_2 \geq \dots \geq \sigma_i \geq 0$, $i = \min(m, p)$ are called singular values.

Let us consider for simplicity that $A \in \mathbb{R}^{p \times m}$. The matrices for the economy SVD are built in the following way: if $p \geq m$ the columns of U are the first m eigenvectors of the matrix AA^T while the columns of V are the eigenvectors of the matrix $A^T A$. On the contrary if $p < m$ the columns of U are the eigenvectors of the matrix AA^T while the columns of V are the first p eigenvectors of the matrix $A^T A$. The (positive) singular values forming the diagonal matrix Σ are the eigenvalues of $A^T A$ (that are the same eigenvalues of $A^T A$).

Also the full SVD exists, that allows to retrieve all the eigenvectors of the matrices AA^T and $A^T A$: the matrix Σ has in this case the same size of the matrix A with non-negative diagonal elements in the decreasing order, the matrix U is of size $p \times p$ and it is built with all the p eigenvectors of the matrix AA^T while the matrix V is of size $m \times m$ and it is built with all the m eigenvectors of the matrix $A^T A$.

Since the full SVD does not supply any further information, from now on the economy SVD is considered.

Consider a matrix multiplication such as $y = Ax$ and the SVD of $A = U\Sigma V^T$ then the multiplication can be written as $y = U\Sigma V^T x$. Basically the columns of V form an orthonormal basis for the input so that the multiplication $V^T x$ rewrites the inputs according to this base. On the contrary the columns of U form an orthonormal basis for the output. The multiplication by the matrix Σ represents just a scaling factor.

The state space system with m inputs and p outputs with $m > p$ can be equivalently represented in terms of the frequency response matrix $G(j\omega)$ of size $p \times m$. If in the considered application we are interested in just one frequency, then the frequency response reduces to a complex numerical matrix of the same size that we call $G(j\bar{\omega})$, on which SVD can be applied.

The decomposition of the complex matrix gives a lot of information: it tells us which are the most significant inputs and outputs in terms of amplitude and if there are some inputs that can be piloted by the same signal so that they can be grouped together. Also, in a similar manner of the RGA, it can be used to pair inputs and outputs with the following pairing rule: the measurement variable corresponding the largest element of the first column of the matrix U is taken and it is paired with the control variable corresponding to the largest element of the first vector of the matrix V . The same is done for the other columns.

However all these pieces of information are limited to the specific frequency considered, and different results may be obtained for different frequencies.

4.3 Decoupler

Sometimes the previous approaches can not be adopted because the the cross-talking between the channels can not be neglected. In these cases the concept of decoupler is introduced. The decoupler is a block inserted typically between the regulator and the plant. It basically compensates for process interactions and thus reduce control loop interactions so that each output can be controlled only by one input. Typically, decoupling controllers are designed using a simple process model such as a steady state model or a transfer function model.

Consider as example a 2×2 system as the one shown in Figure 4.4 where a decoupler was inserted. Let us call the outputs of the regulator $u'_1(t)$ and $u'_2(t)$. Equations (4.4a) and (4.4b) represent the output signals. Without the decoupler we

would have only the first two terms of equations (4.4a) and (4.4b):

$$Y_1(s) = P_{11}(s)U'_1(s) + P_{21}(s)U'_2(s) + P_{11}(s)D_{12}(s)U'_2(s) + P_{21}(s)D_{21}(s)U'_1(s) \quad (4.4a)$$

$$Y_2(s) = P_{22}(s)U'_2(s) + P_{12}(s)U'_1(s) + P_{22}(s)D_{21}(s)U'_1(s) + P_{12}(s)D_{12}(s)U'_2(s) \quad (4.4b)$$

Now we want to eliminate from the first (second) output equation the contribution of the second (first) input. So setting to zero the sum of the terms containing the undesired inputs we get:

$$D_{12}(s) = -\frac{P_{21}(s)}{P_{11}(s)} \quad (4.5a)$$

$$D_{21}(s) = -\frac{P_{12}(s)}{P_{22}(s)} \quad (4.5b)$$

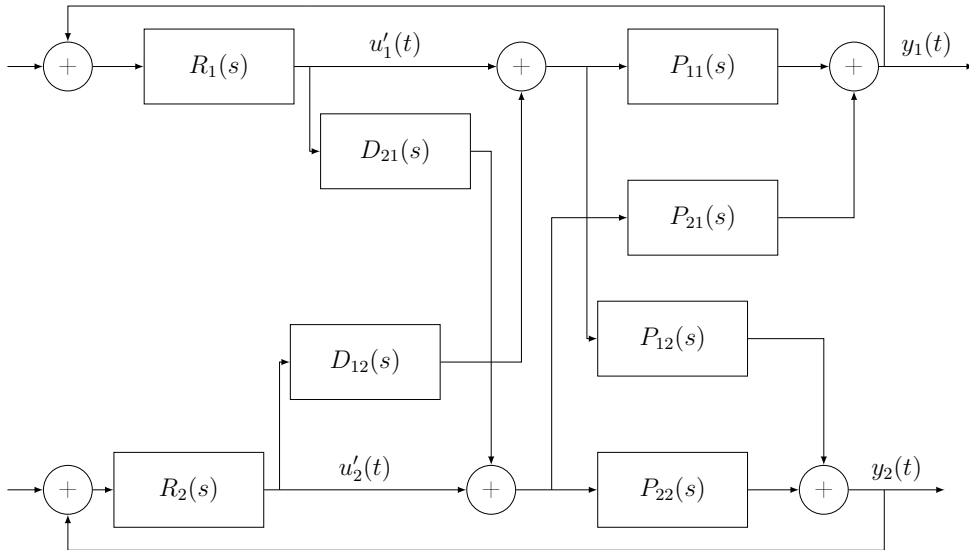


Figure 4.4: Block diagram of the system with a decoupler.

In this case the decoupler is a 2×2 transfer matrix whose diagonal terms are 1 and the other elements are the ones shown above. The regulator and the decoupler have been treated as separated blocks but in general they are represented together as a unique regulator block.

When the system is of bigger size the decoupler can not be designed in this manner. Fortunately other techniques exist that overcome these difficulties. Especially in the next section a SVD decoupler is considered.

4.3.1 SVD decoupling and control

A much more elegant way to implement a decoupler is with the SVD algorithm. Again consider just one frequency component of the disturbance and the feedback system in Figure 4.3. The regulator, according to the measured signals, generates a set of control signals applied to the system.

From the block diagram it is obvious that the following relationships hold:

$$Y(j\bar{\omega}) = G(j\bar{\omega}) U(j\bar{\omega}) \tag{4.6a}$$

$$E(j\bar{\omega}) = D(j\bar{\omega}) + Y(j\bar{\omega}) \tag{4.6b}$$

$$U(j\bar{\omega}) = R(j\bar{\omega}) U'(j\bar{\omega}) \tag{4.6c}$$

The state space system with m inputs and p outputs with $m > p$ can be equivalently represented in terms of the frequency response matrix $G(j\omega)$ of size $p \times m$. If in the considered application we are interested in just one frequency, then the frequency response reduces to a complex matrix of the same size that we call $G(j\bar{\omega})$, on which the SVD can be applied.

Suppose we rewrite the regulator of Figure 4.3 as $R(j\bar{\omega}) = V R_2(j\bar{\omega}) U^H$ where $R_2(j\bar{\omega})$ is a $m \times p$ frequency response matrix evaluated at $\bar{\omega}$. Then we can rewrite the block diagram of Figure 4.3 as shown in Figure 4.5:

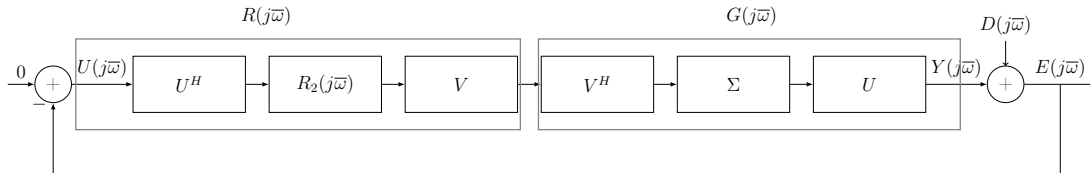


Figure 4.5: SVD expansion of the general feedback block diagram.

Now exploiting the fact that $U^H U = I_{m \times m}$ and $V^H V = I_{m \times m}$ the system simplifies to the one showed in Figure 4.6.

This holds for every frequency but the SVD can be calculated only on a numeric matrix so before computing the decomposition, the transfer function must be calculated at the frequency we are interested in (in our case $\bar{\omega}$). For $R_2(j\bar{\omega})$ the plant to be controlled is a diagonal system hence it can be designed as a diagonal controller:

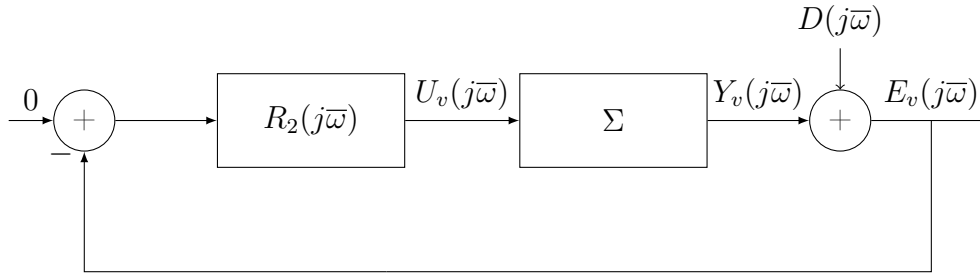


Figure 4.6: Block diagram after the SVD simplification.

in this way the problem becomes that of designing p independent regulators. Note that now the control signals and measured signals are $U_v(j\bar{\omega})$ and $E_v(j\bar{\omega})$: this is the effect of the simplification of the SVD. In fact it remaps the real input and measured signals in a smaller number of virtual input and measured signals. The latter are obtained as a linear combination of the former and the mapping is described by the matrices V and U . In this way the matrices U and V of the SVD has been used to define a decoupler that transforms the MIMO system to a smaller diagonal MIMO system.

Being the procedure limited to one frequency, different regulators must be designed, one for each frequency of the disturbance to be controlled.

4.4 Higher Harmonic Control Algorithm

The algorithm used in this work for noise vibration reduction in helicopters, described in [2] and in [10], is called Higher Harmonic Control and has had great success for vibration reduction applications in helicopters due to its simplicity. It is a frequency domain method whose basic idea is to attenuate the vibratory components at the blade-passing frequency in the fuselage accelerations or in the rotor hub loads by adding suitably phased harmonic components to the rotor controls. The HHC algorithm is based on the assumption that the system of the helicopter, in terms of input and output signals can be represented by a linear model, at least in a fixed state flight condition. Calling N the number of blades and Ω the rotor frequency, assumed to be constant, the algorithm isolates the components at the frequency $N\Omega$ from the previous cycle of the measured residual disturbance. This is done with the expressions in equation (4.7) where $\psi = \Omega t$.

$$e_{Nc}^{(i)} = \frac{2}{T} \int_0^T e^{(i)}(\psi) \cos(N\psi) d\psi \quad (4.7a) \quad e_{Ns}^{(i)} = \frac{2}{T} \int_0^T e^{(i)}(\psi) \sin(N\psi) d\psi \quad (4.7b)$$

$$u_{Nc}^{(i)} = \frac{2}{T} \int_0^T u^{(i)}(\psi) \cos(N\psi) d\psi \quad (4.7c) \quad u_{Ns}^{(i)} = \frac{2}{T} \int_0^T u^{(i)}(\psi) \sin(N\psi) d\psi \quad (4.7d)$$

From these we define the relations in (4.8a) and (4.8b).

$$e_N = \begin{bmatrix} e_{Nc}^{(1)} \\ e_{Ns}^{(1)} \\ \vdots \\ e_{Nc}^{(m)} \\ e_{Ns}^{(m)} \end{bmatrix} \quad (4.8a) \quad u_N = \begin{bmatrix} u_{Nc}^{(1)} \\ u_{Ns}^{(1)} \\ \vdots \\ u_{Nc}^{(p)} \\ u_{Ns}^{(p)} \end{bmatrix}. \quad (4.8b)$$

At the steady state conditions u_N and y_N are related by the following linear equation:

$$e_N = T_{N,N} u_N + w \quad (4.9)$$

where $T_{N,N}$ is a $2p \times 2m$ constant coefficient matrix and w represents the component of the vibration affecting the system at the frequency $N\Omega$.

The matrix $T_{N,N}$ can be calculated from the system frequency response matrix $G(j\omega)$ of size $p \times m$, evaluated at the frequency $N\Omega$:

$$T_{N,N} = \begin{bmatrix} T_{N,N}^{(1,1)} & \cdots & T_{N,N}^{(1,m)} \\ T_{N,N}^{(p,1)} & \cdots & T_{N,N}^{(p,m)} \end{bmatrix} \quad (4.10)$$

$$T_{N,N}^{(i,j)} = \begin{bmatrix} \Re \{G^{(i,j)}(jN\Omega)\} & \Im \{G^{(i,j)}(jN\Omega)\} \\ -\Im \{G^{(i,j)}(jN\Omega)\} & \Re \{G^{(i,j)}(jN\Omega)\} \end{bmatrix}. \quad (4.11)$$

Then, the discrete time algorithm for the attenuation of the effect of w on y_N , known in the rotorcraft literature as the T-matrix algorithm, can be derived by minimizing at each discrete-time step k the LQ-like cost function. Generally such a function is the sum of two terms: one term associated to the residual error to be minimized, and the other associated with the input signal in order to avoid big input signals that might saturate the actuator. The cost function is defined as:

$$J(k) = e_N(k)^T Q e_N(k) + u_N^T(k) R u_N(k) \quad (4.12)$$

where k is the current iteration, $Q = Q^T \geq 0$, $Q \in \mathbb{R}^{2p \times 2p}$, $R = R^T > 0$, $R \in \mathbb{R}^{2m \times 2m}$ are weighting factors.

R and Q are design parameters that must be set carefully since they affect the maximum attenuation that can be achieved. Particularly, if R is close to the zero matrix, all the effort of the algorithm will be on minimizing the error, with no regard for the control effort. On the contrary, the bigger R , the more attention is put in not generating big control signals that might saturate the actuator. Typically Q and R are chosen diagonal.

To derive the control law the cost function must be minimized as in equation (4.13):

$$\frac{\partial J(k)}{\partial u(k)} = 0 = 2R u_N + 2 \left(\frac{\partial e_N(k)}{\partial u(k)} \right)^T Q e_N. \quad (4.13)$$

Substituting equation (4.9) and considering that $\frac{\partial e_N(k)}{\partial u(k)} = T_{N,N}$:

$$R u_N(k) = -T_{N,N}^T Q T_{N,N} u_N(k) - T_{N,N}^T Q w(k) \quad (4.14)$$

so that

$$(Q T_{N,N} N + R) u_N(k) = -T_{N,N}^T Q w(k) \quad (4.15)$$

and calling $(Q T_{N,N} N + R) = D$ we get:

$$u_N(k+1) = -D^{-1} T_{N,N}^T Q w(k). \quad (4.16)$$

We can rewrite this equation in an recursive form using again equation (4.9):

$$u_N(k+1) = -D^{-1} T_{N,N}^T Q (e_N(k) - T_{N,N} u_N(k)) \quad (4.17a)$$

$$u_N(k+1) = -D^{-1} T_{N,N}^T Q e_N + D^{-1} T_{N,N}^T Q T_{N,N} u_N. \quad (4.17b)$$

Let us call $K_N = -D^{-1} T_{N,N}^T Q$ and $K_M = -K_N T_{N,N}$ so that the update equation for the control signal can be written as:

$$u_N(k+1) = K_N e_N(k) + K_M u_N(k). \quad (4.18)$$

In this way a recursive form for the control law has been found. To get the signal back in the time domain the following operation is performed:

$$u(t) = u_{Nc} \cos(\bar{\omega}t) + u_{Ns} \sin(\bar{\omega}t). \quad (4.19)$$

4.5 Modified HHC algorithm

Now let us consider a specific frequency $\bar{\omega}$ of the disturbance. The relations in (4.7) can be rewritten in the following way:

$$e_{Nc} = \frac{2}{T} \int_0^T e(t) \cos(\bar{\omega}t) dt \quad (4.20a) \quad e_{Ns} = \frac{2}{T} \int_0^T e(t) \sin(\bar{\omega}t) dt \quad (4.20b)$$

$$u_{Nc} = \frac{2}{T} \int_0^T u(t) \cos(\bar{\omega}t) dt \quad (4.20c) \quad u_{Ns} = \frac{2}{T} \int_0^T u(t) \sin(\bar{\omega}t) dt \quad (4.20d)$$

where now T is a multiple of the period corresponding the frequency component to be attenuated.

Thanks to the SVD simplification now the system to be controlled is diagonal and its frequency response is represented by the matrix Σ , hence it is possible to design each regulator independently, so let us consider one SISO case. Based on the measured signal, which has a strong component at one frequency $\bar{\omega}$, the regulator generates a control signal so that the frequency component of the disturbance is reduced.

Since the considered system is diagonal, it can be treated as m independent single channel systems, and since we are interested in one frequency component, the transfer function reduces to a complex number in the most general case. From this complex number, the equation in (4.10) can be rewritten in the following way:

$$T_{N,N} = \begin{bmatrix} \Re \{G(j\bar{\omega})\} & \Im \{G(j\bar{\omega})\} \\ -\Im \{G(j\bar{\omega})\} & \Re \{G(j\bar{\omega})\} \end{bmatrix} \quad (4.21)$$

However notice that the frequency response of the considered single channel model is the corresponding singular value σ_i so that:

$$T_{N,N} = \begin{bmatrix} \sigma_i & 0 \\ 0 & \sigma_i \end{bmatrix}. \quad (4.22)$$

For each SISO system now the signals defined in (4.8b) and (4.8a) are $e_N \in \mathbb{R}^2$ and $u_N \in \mathbb{R}^2$. The cost function for each single channel system is defined as in equation (4.12). Now the weighting matrices are $Q = Q^T \geq 0$, $Q \in \mathbb{R}^{2 \times 2}$, $R = R^T > 0$, $R \in \mathbb{R}^{2 \times 2}$. Also the update equation is the the same one given in equation (4.18).

At this point before going back to the time domain, another operation must be performed: in fact the signals e_N and u_N are the measured and control signals for the virtual actuators and sensors obtained with the singular values decomposition. Hence, starting from $e_N^{(r)}$ obtained from the real measurements, $e_N^{(v)}$ corresponding to the virtual measurements must be calculated. From the latter, using the update equation in (4.18) the new $u_N^{(v)}$ is calculated. In the same way $u_N^{(r)}$ corresponding to the real system must be calculated.

To get the virtual measured signals from the real ones and the real control signals from the virtual ones, we have to exploit the matrices V and U^H , the matrices of the SVD. From these matrices two real matrices are defined as done in (4.21) for the transfer function:

$$V_N = \begin{bmatrix} V_N^{(1,1)} & \dots & V_N^{(1,p)} \\ \vdots & & \vdots \\ V_N^{(m,1)} & \dots & V_N^{(m,p)} \end{bmatrix} \quad (4.23a) \quad U_N^H = \begin{bmatrix} U_N^{H(1,1)} & \dots & U_N^{H(1,p)} \\ \vdots & & \vdots \\ U_N^{H(p,1)} & \dots & U_N^{H(p,p)} \end{bmatrix} \quad (4.23b)$$

This multiplication must be performed in the following way. For the i -th simplified single channel case we have two vectors $e_N^{(v,i)}$ and $u_N^{(v,i)}$ of size 2×1 , for the virtual measured and control signals. These vectors corresponding to different virtual single channel cases are collected in two vectors in the following way (remember that thanks to the SVD simplification, we have p virtual inputs and p virtual outputs):

$$e_N^{(v)} = \begin{bmatrix} e_N^{(v,1)} \\ e_N^{(v,2)} \\ \vdots \\ e_N^{(v,p)} \end{bmatrix} \quad (4.24a) \quad u_N^{(v)} = \begin{bmatrix} u_N^{(v,1)} \\ u_N^{(v,2)} \\ \vdots \\ u_N^{(v,p)} \end{bmatrix} \quad (4.24b)$$

so that $e_N^{(v)} \in \mathbb{R}^{2p \times 1}$ and $u_N^{(v)} \in \mathbb{R}^{2p \times 1}$. They are equivalent to the following:

$$e_N^{(v)} = \begin{bmatrix} e_{Nc}^{(v,1)} \\ e_{Ns}^{(v,1)} \\ \vdots \\ e_{Nc}^{(v,p)} \\ e_{Ns}^{(v,p)} \end{bmatrix} \quad (4.25a) \quad u_N^{(v)} = \begin{bmatrix} u_{Nc}^{(v,1)} \\ u_{Ns}^{(v,1)} \\ \vdots \\ u_{Nc}^{(v,p)} \\ u_{Ns}^{(v,p)} \end{bmatrix} \quad (4.25b)$$

The same can be applied for the real measured and control signals to get $e_N^{(r)} \in \mathbb{R}^{2p \times 1}$

and $u_N^{(r)} \in \mathbb{R}^{2m \times 1}$. Now we perform the following transformations:

$$e_N^{(v)} = U_N^H e_N^{(r)} \quad (4.26a) \quad u_N^{(r)} = V_N u_N^{(v)}. \quad (4.26b)$$

Summarizing, the following steps must be performed:

- from the (real) measured signal $e(t)$ calculate $e_N^{(r)}$ from equations in (4.20a) and (4.20b);
- once we have these coefficients, we need to calculate the coefficients corresponding to the virtual measurements. This is done by multiplying them by the matrix U_N^H and in this way we get $e_N^{(v)}$. Then from this vector whose structure is the same of equation (4.24a) we extract the coefficients $e_N^{(v,i)}$ for each i – th virtual single channel;
- for each virtual single channel the coefficients $u_N^{(v,i)}$ of the virtual control signals are calculated independently with the update equation in (4.18);
- from $u_N^{(v)}$ defined in (4.24b), we need to calculate the coefficients $u_N^{(r)}$ of the real system: this is done by multiplying it by the matrix V_N ;
- finally the control signals for the real actuators can be brought to the time domain thanks to equation (4.19) to get $u(t)$.

The procedure described above must be performed for each frequency component of the disturbance that must be attenuated. In this way, a set of control variables is obtained for each frequency. Thanks to the linearity assumption, the control variables are independent and they can be summed.

4.6 Simulation of the control technique on a small subsystem

To test the described procedure some simulations were performed on a small subsystem characterised by a limited number of channels. The frequency response matrix of the global model identified with the scaling procedure was calculated each time at one specific frequency. Then only the terms corresponding to the channels of the subsystem have been considered. On the resulting matrix the SVD was applied and the matrices V_N and U_N^H were calculated as in equations (4.23). In this way the control has been defined using the frequency response of the global model.

The same frequency response matrix was used to represent the subsystem to be controlled, on which the control was applied. However, to have a more realistic situation, for each simulation the control was also tested on the subsystem represented by the frequency responses of the SISO models, assumed to be a closer representation of the real subsystem. In both cases the frequency response of the subsystem was represented in the form of equation (4.10). The output generated by the model was calculated as in equation (4.27):

$$y_N = T_{N,N} u_N . \quad (4.27)$$

The disturbance acting on the sensors of the subsystem was assumed to be the same and to be given by equation (4.28):

$$d(t) = 10 \cos(\bar{\omega}t) \quad (4.28)$$

that can be rewritten using equation (4.8a) as $D_N = \begin{bmatrix} 10 \\ 0 \end{bmatrix}$.

In all the simulations the number of actuators was kept higher than the number of sensors and all the weighting matrices were defined as in equation (4.29):

$$Q = I_2 \quad (4.29a) \quad R = \rho I_2 \quad (4.29b)$$

where ρ is a setting parameter. In particular, with small values of ρ , the control signals generated are of large amplitudes while the number of iterations needed to reach the steady state increases. Although in these simulations no attention was put on the control signals, generally the weighting matrices must be chosen to avoid actuators saturation.

Despite the fact that the disturbance was assumed to have only a cosine component, when testing the control it was noticed that the sine component assumed a value different from zero in some cases. For this reason in the plots the residual disturbance has been represented in terms of the modulus, instead of representing the sine and cosine components separately.

4.6.1 First simulation: influence of the R weighting matrix

A first simulation was performed to show the influence of the weighting matrix R for varying values of ρ . The considered inputs are the actuators TS06, TS12, TD05, TD11 while the sensors are the accelerometers 3 and 11. The frequency of the disturbance was assumed to be 4250 Hz.

The results are shown in Figures 4.7 and 4.8. When the control is tested on the subsystem defined with the same frequency response, the steady state is reached at the first iteration. Moreover, in this case it is possible to make the disturbance arbitrarily small by using a sufficiently small value of ρ .

When the control is tested on the subsystem defined with the frequency response of the SISO models, for relatively high values of ρ the steady state is still reached in a few number of iterations. When ρ decreases, a larger attenuation is achieved but a higher number of iterations is needed to reach the final attenuation. However if the chosen value is too small, due to the differences between the two frequency response matrices, the output might diverge. Sometimes it happens that the levels of attenuation are even larger when the control is applied to the subsystem calculated from the SISO models (Figure 4.8). This might be due to the fact that the frequency responses of the SISO models have generally a bigger magnitude compared to the frequency responses of the same channels of the global model. For this reason, the generated control signal is able to attenuate more the disturbance.

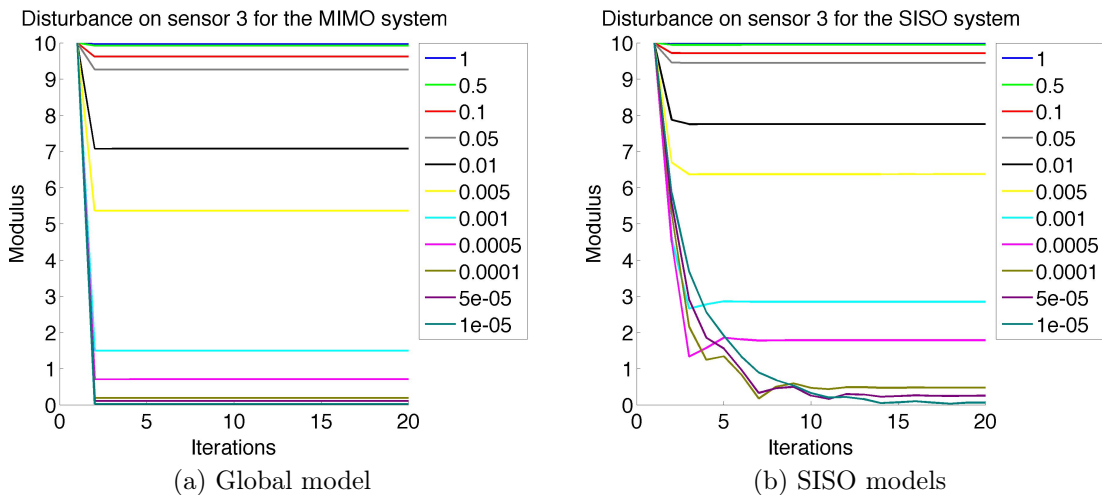


Figure 4.7: Module of the disturbance at the accelerometer 3 for the control applied to the subsystem defined with the frequency response of the global model (4.7a) and to the subsystem defined with the frequency response of the SISO models (4.7b) for different values of ρ .

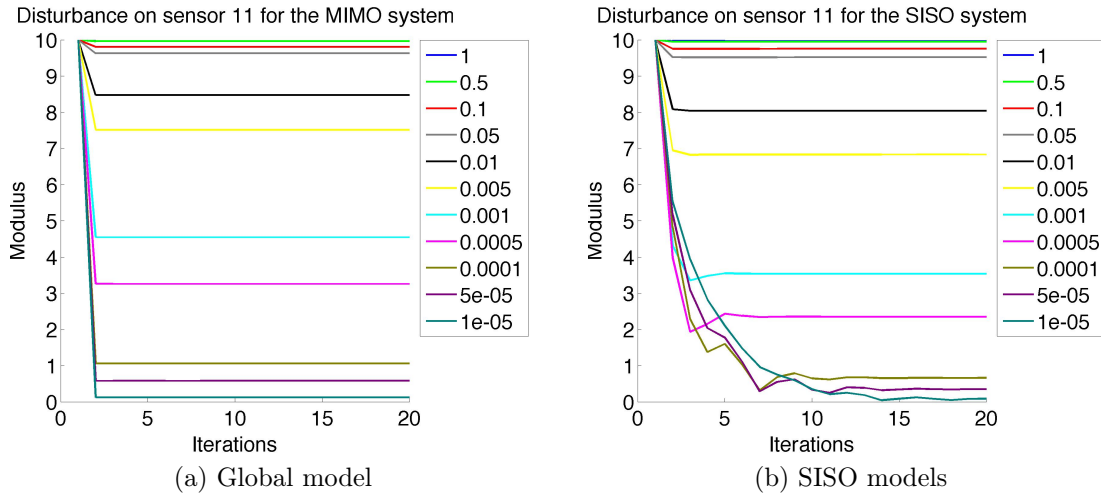


Figure 4.8: Module of the disturbance at the accelerometer 11 for the control applied to the subsystem defined with the frequency response of the global model (4.8a) and to the subsystem defined with the frequency response of the SISO models (4.8b) for different values of ρ .

4.6.2 Second simulation

Another simulation was performed on a different frequency of the disturbance (2400 Hz). The inputs employed are the same (TS06, TS12, TD05, TD11) while the outputs considered are now the accelerometers 2 and 11. The parameter ρ has been adjusted to 3×10^{-5} . The results are shown in Figure 4.9. In this case the attenuation obtained at the accelerometer 2 (Figure 4.9a) is almost equal for both of the subsystems. On the contrary for the accelerometer 11 the results are significantly different: a larger attenuation is achieved for the subsystem defined with the frequency response of the global model. This fact is caused by the differences in the two frequency response matrices used to define the subsystem. Setting a smaller value of ρ not only does not improve the levels of the attenuations but on the contrary might result in an increased disturbance or may cause the outputs to diverge.

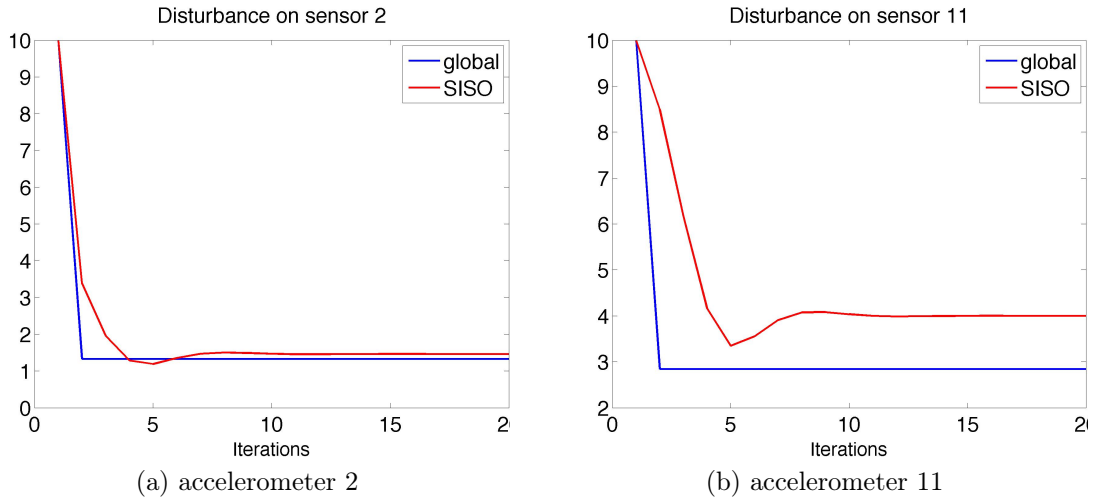


Figure 4.9: Module of the residual disturbance at the accelerometers 2 (4.9a) and 11 (4.9b) for the second simulation. The results obtained for the subsystem defined with the frequency response of the global model are in blue, the ones for the subsystem defined with the the frequency response of the SISO models are in red.

4.6.3 Third simulation

A third simulation was performed considering again the frequency 4250 Hz of the disturbance. In this case a larger number of inputs and outputs have been taken into account. In particular the inputs are the actuators TS05, TS06, TS11, TS12, TD05, TD06, TD11, TD12. The sensors are the accelerometers 3, 4, 12 and 16 and the parameter ρ was set to 2×10^{-4} .

The results are shown in Figure 4.10. Also in this case a significant attenuation is obtained at all the sensors. Again, in some cases a larger attenuation is obtained when testing the control on the subsystem defined with the SISO frequency responses.

Performing other simulations on a different set of channels with the same number of inputs and outputs showed that in this case the problem of control becomes more difficult. In particular it happens that no significant attenuation is obtained at some channels while for some others the disturbance is greatly reduced. Apart from the inaccuracy of the global model this might be related to the fact that some input channels might be important only for few accelerometers and vice versa. For this reason, only a subset of inputs and outputs might be needed to control the disturbance at one considered frequency, simplifying the problem a lot.

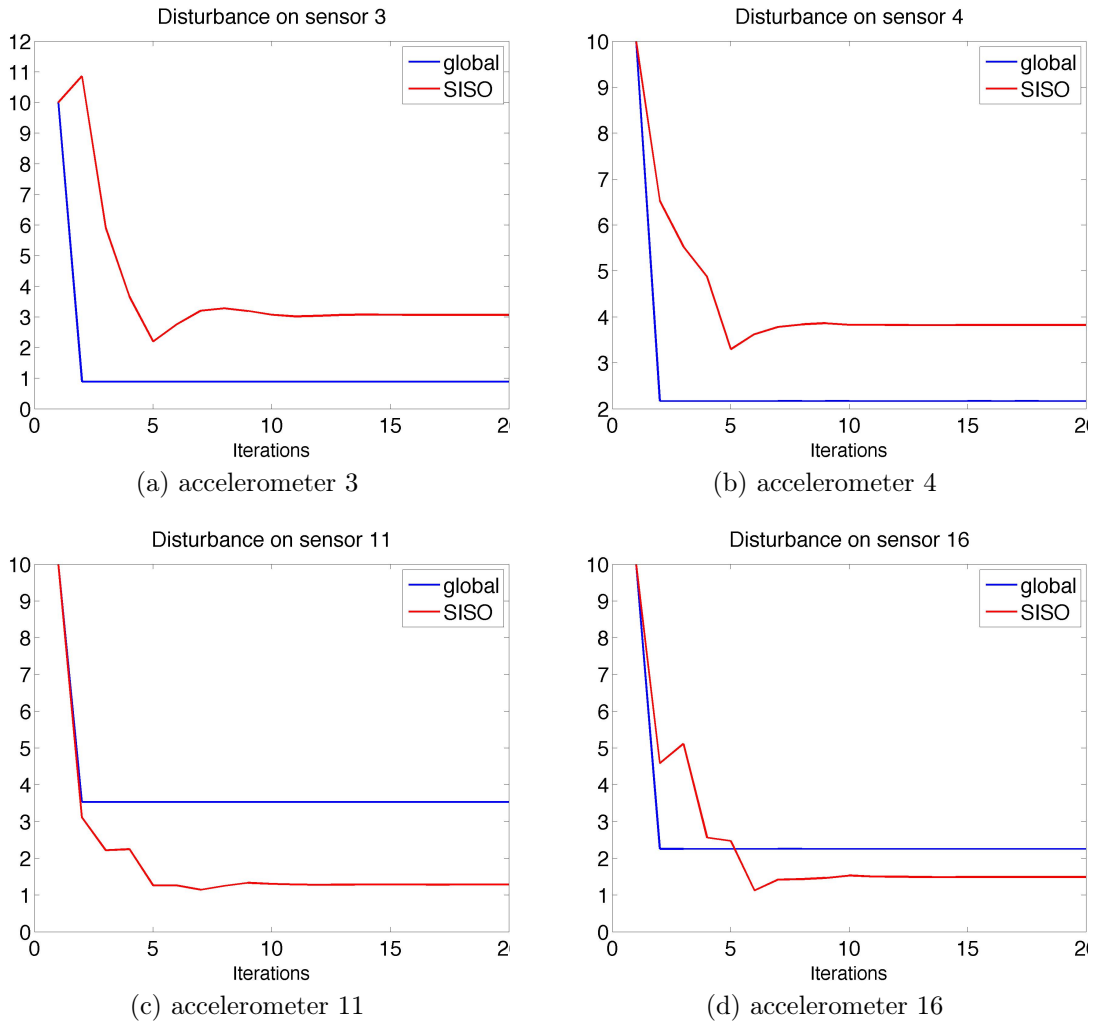


Figure 4.10: Module of the residual disturbance at the accelerometers 3 (4.10a), 4 (4.10b), 11 (4.10c) and 16 (4.10d) for the third simulation. The results obtained for the subsystem defined with the frequency response of the global model are in blue, the ones for the subsystem defined with the frequency responses of the SISO models are in red.

4.7 Comments on the results

These simulations were performed in order to understand if the SVD approach together with the adopted control technique can give good results in real applications, although the estimation of the global model is not accurate. From the results we can state that this method seems promising: despite the differences in the frequency responses, a significant attenuation is always achieved for a small subsystem, given a proper choice of the weighting matrices.

However, when testing the control technique on a larger subsystem, the attenuation becomes more difficult. First of all, higher values of ρ must be selected to avoid divergence. This fact reduces the maximum achievable attenuations and for this reason at some sensors no significant attenuation is achieved. This might be connected to the fact that for some channels the estimation of the global model is inaccurate. Probably, with a more reliable model better results can be achieved.

Chapter 5

Conclusions

In this chapter the results obtained with the identified models and the simulations of the control are commented and possible ways of improvement are discussed. Finally, possible further developments of the project are discussed.

5.1 Comments on the models estimated

This work represents an introductory study for active vibrations control applied to a helicopter cabin. The adopted control technique requires a model of the plant to be controlled and the identification of the system was the primary objective of this study.

Different models were estimated employing different techniques in order to achieve a better estimation. However the results were only partially satisfactory and the model can be considered reliable only for a limited number of channels. Nevertheless when using the identified model to design a simple control for a small subsystem, good levels of attenuations of the disturbance were achieved in the simulations.

Being the final objective of this class of projects the design of a full control system, a more reliable model might be needed. To achieve a better estimation, the following possibilities can be taken into account:

- improve the set-up (actuators, sensors, acquisition devices etc.): one of the problems seen is that the output signals have a very small amplitude and this is true especially when the actuators on the rear struts are excited. Changing the actuators and the acquisition devices enables to generate inputs of larger amplitudes so that also the amplitudes of the output signals are larger. In this way a better identification of the model should be obtained;

- increase the number of samples for the identification and the value of the parameter s (see Section 2.6.2): due to the limited computing power, it was not possible to set these parameters to higher values. However increasing them might result in significant improvements in the estimated model. To do this two possibilities are available: use a more powerful computer or reduce the number of input and output channels. For the latter particularly, when estimating small MIMO models it has been noticed that as the number of channels was increased, the performances were degraded;
- perform an identification of the model at specific frequencies or identify a model for each frequency component of the disturbance: this can be achieved by filtering the data off-line with a narrow bandpass filter or using other types of excitation signals such as chirp signals. In this way the model should be more accurate at the frequencies of interest and even a lower order might be selected.

With these techniques a reliable model should be obtained on which the full design of the control system can be carried out.

5.2 Comments on the control system

As seen in Chapter 4, the problem of the control design was analyzed and some simulations were performed on a small subsystem. To have a more realistic situation, the control was designed using the frequency response of the global model identified with the scaling procedure, and it was applied to the subsystem defined by the SISO models previously identified, assumed to be a closer representation of the real system.

The control law based on the HHC algorithm, together with the SVD decoupler, showed encouraging results for small subsystems. The attenuation of the disturbance becomes more difficult for larger subsystem, more likely due to the differences between the frequency responses. Although the design of the control system must be further analyzed, possibly exploiting a more reliable model, the results obtained with the simulations together with its simplicity and ease of implementation, make this innovative control technique appealing for noise vibration control in helicopters.

5.3 Further developments

Apart from the already discussed improvements for the identification of the model, the main development for this work regards the design of the control system.

The design of an active system for vibration control in helicopters is generally a challenging task requiring many years of studies and experiments. Among the numerous steps to be performed, once the technique of control is defined, the control algorithm must be implemented and on-ground experiments must be performed, in order to test the ability of the system to reduce the vibrations induced by the main rotor. When good results are achieved for these tests, then the active system must be prepared for flight tests.

During the flight, many problems can arise depending on the different flight conditions. First of all the tones of the disturbance are not constant but can shift in the frequencies: this might require an additional step in which the frequency of the disturbance must be determined. Consequently, the identified model is required to be accurate at least in a neighborhood of the frequencies of the disturbance. Secondly, particular non-stationary aerodynamic conditions can arise during the flight. The unsteady conditions decrease the achievable attenuations and varying flight conditions produces uncertainties in the estimation of the T-matrix, that might require an on-line estimation [13].

For these reasons, the design of an efficient control system for active vibrations control in helicopters is a demanding objective and being this thesis a first study, still much work must be performed.

Appendices

Appendix A

Numerical results for the simulation of the global model

	AS01	AS02	AS03	AS04	AS05	AS06	AS07	AS08
A1	-120.84	-58.35	-105.64	-124.76	-13.07	-29.76	10.33	15.28
A2	-30.24	-17.43	-144.15	-84.07	-87.88	-70.23	-16.77	-43.50
A3	37.10	32.88	38.95	45.69	53.08	44.90	45.21	46.71
A4	25.38	29.36	59.91	42.23	43.71	56.72	39.95	47.20
A5	4.47	-0.84	-3.03	2.06	-8.10	-15.32	-14.40	-16.81
A6	31.26	41.36	67.58	48.10	58.99	75.17	57.49	57.12
A7	5.10	14.33	21.63	17.57	29.71	18.18	25.82	21.89
A8	5.87	3.06	-7.24	-18.64	13.76	50.59	31.66	49.54
A9	4.30	4.98	9.97	10.76	20.87	18.89	22.66	23.71
A10	-115.58	-79.82	-207.72	-231.63	-268.61	-380.81	-369.17	-399.64
A11	-179.94	-125.19	-122.28	-258.51	-287.35	-364.50	-479.34	-290.22
A12	33.02	-0.35	-18.99	40.32	16.31	0.07	6.79	-6.32
A13	2.46	-3.73	12.85	-15.86	-22.50	-103.13	-107.84	-16.46
A14	-36.97	-23.84	-35.91	-27.89	-25.07	-77.44	-52.44	-46.71
A15	1.94	-54.81	-19.10	-61.53	-24.77	-8.83	-41.21	22.93
A16	-39.54	-51.84	-0.40	18.72	32.89	15.36	27.52	-1.04
A17	9.45	10.49	-25.11	-11.25	-3.77	-19.96	-3.37	-3.23
A18	-5.35	-13.95	-24.92	-6.56	-25.40	-42.24	-42.45	-52.29

Table A.1: Simulation results of the global model for the actuators on the left rear strut in terms of the *vaf* criterion.

Appendix A: Numerical results of the global model

	TS01	TS02	TS03	TS04	TS05	TS06	TS07	TS08	TS09	TS10	TS11	TS12
A1	60.57	62.90	55.03	58.55	50.52	17.99	29.95	52.82	63.68	38.70	53.83	58.47
A2	27.08	27.21	47.38	36.42	38.75	30.24	34.19	41.79	52.37	46.51	51.59	45.67
A3	61.20	77.43	84.31	69.34	62.02	64.89	44.95	62.91	73.22	64.03	71.78	71.09
A4	47.29	67.25	55.67	47.68	61.93	33.11	3.80	-11.27	21.19	23.73	30.63	6.01
A5	11.73	20.68	6.25	12.48	6.37	1.73	-0.01	15.56	26.74	14.91	1.36	7.28
A6	27.18	43.59	33.47	35.76	22.72	31.44	55.51	72.56	51.66	39.15	66.10	63.25
A7	3.11	27.60	26.21	22.82	22.53	-42.46	4.20	20.71	21.71	-0.82	1.97	1.03
A8	9.68	31.92	36.79	6.68	15.15	13.29	-8.23	30.95	26.44	14.46	-22.27	19.80
A9	0.52	-44.02	-17.23	-7.20	-2.56	-33.82	-32.45	-89.49	-1.27	8.21	-22.30	-13.93
A10	-37.91	-16.95	-34.93	-27.08	1.79	-17.13	-32.94	-55.48	-69.79	-47.06	-85.08	-45.04
A11	9.79	-46.07	-75.81	-4.52	-1.14	-30.98	-151.56	-219.15	-199.42	-91.37	-138.85	-145.69
A12	36.04	-14.74	42.13	60.31	51.74	45.84	-22.84	-15.78	11.03	3.94	20.13	37.56
A13	25.73	22.72	23.68	34.69	47.98	30.21	-43.31	-56.35	-34.63	-13.08	-8.37	-29.84
A14	-3.26	-47.97	-62.09	-4.49	13.87	5.90	-8.42	-26.17	-8.66	-5.31	9.38	6.27
A15	42.23	22.41	19.67	57.44	69.53	55.35	-12.38	-47.57	0.55	-8.01	-4.45	5.48
A16	37.61	-0.63	31.36	49.19	58.76	25.08	15.79	38.10	24.22	20.72	17.91	24.98
A17	-6.49	-15.73	-3.50	-6.10	-12.92	-7.98	2.87	-1.56	2.69	-2.43	-5.12	-6.09
A18	9.89	-11.07	-14.76	12.21	27.74	18.38	-8.64	-69.30	9.62	10.14	-36.77	0.61

Table A.2: Simulation results of the global model for the actuators on the left side of the anti-torque plate in terms of the *vaf* criterion.

	AD01	AD02	AD03	AD04	AD05	AD06	AD07	AD08
A1	-153.53	-135.48	-59.50	-115.41	-217.84	-180.07	-496.47	-552.51
A2	-256.17	-225.96	-83.41	-152.85	-329.92	-243.76	-484.59	-298.39
A3	1.65	-30.46	-60.96	-29.21	-138.45	-65.56	-141.14	-154.46
A4	-107.06	-105.54	3.69	-41.04	18.68	39.24	6.24	32.07
A5	-16.55	-10.44	-24.43	-50.32	-50.84	-46.34	-50.25	-38.36
A6	-37.79	-36.51	-43.58	4.56	-23.78	-53.49	-56.59	-49.45
A7	-9.34	9.62	-78.55	-102.05	-83.13	-73.37	-44.45	-42.81
A8	-17.21	-13.41	-37.16	-86.28	-177.23	-68.94	-125.86	-121.53
A9	-2.62	1.63	-14.75	3.20	-29.82	-43.49	-17.63	-42.64
A10	-11.53	-53.03	-194.47	-268.43	-338.77	-189.36	-252.59	-276.76
A11	-9.38	-7.79	-129.90	-16.05	-51.10	-168.57	-103.05	-84.90
A12	28.34	13.86	-15.47	0.78	-2.73	-4.47	4.91	7.70
A13	28.72	41.04	13.25	15.23	71.35	61.72	68.33	68.14
A14	4.59	-5.45	-8.67	-10.67	39.24	22.69	25.35	37.85
A15	51.72	61.84	55.23	52.88	82.07	81.93	85.86	85.88
A16	-9.14	11.42	53.45	58.39	58.59	54.24	56.74	36.94
A17	8.48	7.43	-11.90	-12.40	-8.77	16.84	23.33	28.28
A18	-3.79	-3.52	28.62	17.99	38.76	39.71	34.34	42.70

Table A.3: Simulation results of the global model for the actuators on the right rear strut in terms of the *vaf* criterion.

	TD01	TD02	TD03	TD04	TD05	TD06	TD07	TD08	TD09	TD10	TD11	TD12
A1	-7.41	-0.46	-40.99	-19.98	-36.95	-73.71	-8.16	-20.35	-34.57	-59.73	-24.80	-7.41
A2	13.54	12.02	-85.64	-34.09	-19.70	-68.72	-52.12	-105.50	-256.57	-175.24	-112.92	-118.22
A3	40.88	47.41	59.77	49.83	38.81	43.74	-41.51	-77.04	13.70	17.87	31.16	24.00
A4	-4.91	-27.43	-20.25	2.93	5.03	-89.84	-10.62	-31.20	-9.63	-8.59	-23.29	-9.21
A5	-0.01	7.24	8.07	3.92	8.27	3.45	0.42	-8.73	2.11	16.16	0.45	4.44
A6	14.74	-9.37	-16.05	7.74	22.28	18.92	-23.05	-2.69	-5.21	-12.97	-25.02	-9.14
A7	-1.07	10.43	9.01	7.48	25.20	7.62	15.34	10.46	15.73	14.12	-1.63	7.87
A8	-34.66	-26.36	-44.84	-26.48	-26.52	-14.60	2.99	6.14	7.50	5.66	-35.01	-18.24
A9	-8.43	-2.17	19.06	5.04	-4.40	-3.26	-9.65	-41.34	6.35	15.90	3.60	4.18
A10	43.10	54.23	21.98	35.32	39.87	-3.22	30.19	56.18	47.81	27.28	48.80	51.35
A11	16.55	17.99	25.67	24.33	18.20	26.04	16.39	18.07	25.63	21.80	17.48	18.89
A12	30.58	57.68	74.23	59.14	49.06	54.18	34.53	49.28	62.76	48.50	46.83	50.54
A13	-8.41	3.56	7.22	16.62	30.71	-27.97	18.70	20.19	-1.70	-1.44	13.69	12.36
A14	26.64	-21.06	4.52	36.89	13.40	13.86	10.13	20.97	21.44	15.46	20.55	14.48
A15	63.95	54.87	60.80	62.83	60.75	57.22	13.67	30.59	29.56	13.31	26.64	38.71
A16	81.16	55.52	61.74	83.69	50.02	60.84	22.90	18.48	38.53	20.61	37.53	43.68
A17	3.81	4.61	6.76	6.20	5.70	7.57	14.40	2.33	-2.74	5.06	-2.46	2.98
A18	36.28	33.37	33.42	28.66	43.58	39.92	18.20	13.11	6.70	9.76	12.34	19.47

Table A.4: Simulation results of the global for the actuators on the right side of the anti-torque plate in terms of the vaf criterion.

Appendix B

Numerical results for the simulation of the global model identified with normalized measurements

	AS01	AS02	AS03	AS04	AS05	AS06	AS07	AS08
A1	-7.48	-0.97	30.17	14.89	26.86	25.18	26.24	29.79
A2	13.41	20.70	-3.66	7.41	29.14	15.81	38.55	28.80
A3	28.21	27.47	35.05	32.06	32.98	38.46	28.30	26.28
A4	44.13	40.52	77.00	59.86	60.91	63.55	42.37	59.16
A5	12.13	-1.44	44.66	37.22	35.48	39.13	24.07	28.61
A6	28.96	37.49	59.65	50.23	65.64	74.06	67.87	57.18
A7	6.55	27.12	13.60	26.55	51.49	19.93	44.39	34.04
A8	5.30	9.93	8.83	-12.11	21.73	52.61	37.18	47.30
A9	12.68	8.93	10.72	25.12	43.40	35.87	50.17	36.36
A10	-0.39	4.25	-8.42	-20.34	-21.71	-10.26	-5.21	-21.54
A11	-7.26	-1.14	-15.17	-19.15	-20.87	-18.68	-7.28	-14.25
A12	27.25	11.82	4.26	17.71	19.08	14.44	25.84	25.18
A13	4.14	23.61	17.46	1.09	39.93	21.45	37.82	57.57
A14	24.79	46.05	40.69	30.57	40.58	31.27	34.54	44.60
A15	0.12	-5.48	-0.81	-17.32	-9.22	-1.38	-2.01	19.19
A16	-0.55	-2.93	12.52	18.80	15.02	24.81	26.67	-2.36
A17	19.09	21.76	24.40	32.16	31.62	31.75	39.88	41.21
A18	0.95	-8.68	5.68	18.89	11.73	-0.99	-4.87	-7.23

Table B.1: Simulation results of the global model identified with the scaled output signals for the actuators on the left rear strut in terms of the *vaf* criterion.

	TS01	TS02	TS03	TS04	TS05	TS06	TS07	TS08	TS09	TS10	TS11	TS12
A1	40.93	35.53	43.71	36.29	39.24	35.65	18.41	9.75	54.24	42.58	44.41	44.19
A2	44.03	57.98	66.52	54.89	71.22	56.70	50.03	65.01	58.40	53.00	58.36	67.71
A3	37.97	34.22	57.91	51.21	49.84	52.19	15.78	21.05	25.59	27.81	23.74	29.87
A4	43.14	69.65	68.54	52.12	56.92	44.28	30.33	24.89	27.28	12.46	29.99	29.08
A5	39.68	19.38	32.60	23.00	25.51	28.11	36.54	60.73	35.26	26.91	39.14	35.30
A6	13.64	12.22	14.84	19.56	23.60	19.44	39.41	47.15	33.95	11.59	41.79	49.82
A7	28.14	19.12	21.78	33.83	30.95	-17.75	15.11	14.69	20.54	26.74	18.43	15.20
A8	15.09	38.77	36.47	9.98	18.10	26.60	11.99	15.15	23.80	18.83	-1.21	23.57
A9	26.76	30.95	28.44	23.70	33.59	12.50	15.93	21.79	41.57	22.55	19.51	24.99
A10	8.05	7.96	13.12	12.96	9.11	6.25	-10.77	-13.96	1.61	12.91	-0.17	0.36
A11	38.61	43.07	51.93	40.33	45.79	52.42	-3.12	3.99	-1.17	7.37	-5.75	-0.75
A12	22.03	18.36	30.79	30.10	26.65	27.33	-1.28	2.11	17.25	15.22	13.77	20.13
A13	36.48	34.41	50.39	44.01	55.60	48.31	-3.88	1.19	22.30	13.96	18.83	3.53
A14	25.61	27.55	36.14	13.44	-2.73	31.23	1.90	-13.68	9.64	6.29	0.60	-6.36
A15	39.15	17.49	27.80	50.11	56.89	43.51	-2.82	-7.23	-4.43	8.63	16.09	6.04
A16	16.50	-11.46	11.24	33.03	34.89	14.62	4.27	-0.26	15.16	12.82	10.03	13.33
A17	33.89	39.00	40.56	33.24	35.94	31.04	31.00	42.54	20.88	4.09	20.07	14.74
A18	23.21	20.67	21.58	17.26	30.59	34.53	-1.83	-10.18	9.61	12.64	-10.27	5.22

Table B.2: Simulation results of the global model identified with the scaled output signals for the actuators on the left side of the anti-torque plate in terms of the vaf criterion.

	AD01	AD02	AD03	AD04	AD05	AD06	AD07	AD08
A1	-16.16	-7.52	8.40	5.06	-8.99	2.72	-5.29	-10.82
A2	-1.19	2.77	14.41	5.85	10.25	10.61	16.37	20.58
A3	19.79	-0.61	5.92	6.96	5.78	14.93	4.98	9.67
A4	8.45	15.16	27.76	15.89	22.88	33.43	35.64	28.52
A5	19.07	2.80	12.49	16.48	28.46	33.89	37.60	38.68
A6	-18.89	-11.44	-3.38	5.76	0.35	-2.98	1.24	-12.06
A7	6.22	10.34	-3.88	0.75	-2.19	7.09	11.39	2.26
A8	10.06	16.14	-5.28	-1.35	-0.91	-7.09	5.40	0.41
A9	-1.77	8.23	-0.13	3.05	-0.70	-1.95	0.05	-9.03
A10	35.57	19.80	23.83	12.09	24.15	31.66	41.75	47.68
A11	9.98	15.51	11.90	24.49	34.03	25.95	37.85	29.78
A12	27.65	22.65	5.57	14.95	34.32	25.79	34.51	39.77
A13	70.23	52.07	34.54	30.41	70.51	81.49	77.88	84.68
A14	40.91	14.48	29.54	42.65	73.50	69.45	70.32	78.68
A15	24.70	31.40	50.72	47.75	76.56	77.58	79.47	80.22
A16	-5.02	14.50	33.59	36.63	52.03	36.79	43.69	47.87
A17	48.04	37.64	10.04	22.04	-9.73	7.24	26.03	29.74
A18	-15.12	-2.65	36.98	33.55	50.36	48.48	53.58	55.03

Table B.3: Simulation results of the global model identified with the scaled output signals for the actuators on the right rear strut in terms of vaf criterion.

	TD01	TD02	TD03	TD04	TD05	TD06	TD07	TD08	TD09	TD10	TD11	TD12
A1	-5.44	17.44	9.52	-11.15	-0.70	17.69	5.51	-10.23	8.74	3.37	2.35	18.14
A2	23.13	30.12	25.50	18.71	37.53	33.72	-1.63	-0.38	5.70	2.35	-3.13	0.15
A3	16.29	22.64	27.06	30.48	33.37	17.21	3.89	-9.90	33.18	36.42	29.63	25.81
A4	24.22	12.25	10.26	31.08	23.57	14.18	0.95	11.02	8.39	3.78	10.01	5.05
A5	28.82	38.84	37.36	25.97	23.29	29.16	11.27	20.79	5.38	7.43	11.93	-0.74
A6	24.46	-10.27	6.52	18.71	10.40	9.70	0.92	8.98	16.70	8.69	5.20	10.29
A7	5.79	14.51	7.42	13.46	36.76	16.25	8.32	-0.49	6.03	6.62	-7.95	-1.00
A8	-7.68	-8.33	-9.47	-9.61	-16.60	-6.32	-7.28	-4.67	-0.71	1.79	-12.69	-22.11
A9	17.48	24.33	14.36	12.97	25.36	17.16	-1.74	-1.09	-1.49	6.31	-3.53	-0.31
A10	30.88	13.14	-1.96	17.71	18.45	0.34	33.84	15.33	35.98	40.81	24.69	35.91
A11	24.25	40.51	52.80	42.79	33.15	48.00	40.97	50.91	35.30	29.40	28.81	31.79
A12	24.74	42.86	56.17	42.15	32.61	41.99	31.07	30.25	45.74	37.86	30.96	38.22
A13	21.08	4.06	20.53	30.14	39.97	-0.17	46.57	49.31	16.08	11.19	23.27	27.92
A14	48.10	18.13	41.53	44.61	30.77	37.13	29.21	46.15	35.38	31.23	34.63	41.82
A15	61.75	39.38	58.84	62.73	57.65	46.45	16.87	14.55	9.02	-7.98	15.63	31.79
A16	59.70	25.97	34.72	61.49	49.86	51.85	33.45	18.53	11.91	2.68	36.76	35.98
A17	8.84	58.77	19.92	-7.45	34.27	27.59	21.04	31.11	10.45	12.05	2.80	15.20
A18	45.04	43.46	39.23	38.42	46.82	53.71	39.96	23.67	25.19	29.30	26.50	35.29

Table B.4: Simulation results of the global model identified with the scaled output signals for the actuators on the right side of the anti-torque plate in terms of the *vaf* criterion.

Appendix C

Numerical results for the simulation of the global model identified with filtered data

	AS01	AS02	AS03	AS04	AS05	AS06	AS07	AS08
A1	35.42	53.91	50.77	63.05	48.50	74.55	37.71	30.88
A2	23.30	15.75	41.04	78.27	26.00	19.79	86.75	53.78
A3	47.47	73.48	52.39	9.67	68.96	4.23	17.89	29.35
A4	24.03	4.04	30.57	19.12	12.49	52.43	4.59	15.22
A5	49.98	-3.08	50.34	68.24	-8.56	18.62	63.65	72.88
A6	51.02	1.25	46.77	85.05	4.91	33.09	84.20	71.61
A7	16.12	13.15	48.35	70.53	23.21	30.34	70.61	67.60
A8	66.20	-6.82	21.87	69.79	18.22	61.74	59.43	22.78
A9	24.34	88.64	48.79	26.79	84.36	17.02	29.92	20.55
A10	7.98	40.75	10.41	38.77	53.94	44.84	55.46	46.18
A11	15.59	65.77	75.95	48.43	60.84	32.45	36.16	65.58
A12	21.98	27.24	37.68	53.44	55.58	70.57	57.00	54.69
A13	20.20	41.21	61.31	51.00	44.42	16.54	50.51	58.86
A14	8.66	2.81	48.22	45.69	8.06	62.25	51.61	50.41
A15	64.13	26.16	42.47	33.39	26.48	80.51	30.22	15.93
A16	36.18	66.20	47.00	44.31	70.50	50.87	47.85	33.39
A17	59.43	29.27	14.26	52.44	7.92	74.06	48.03	17.16
A18	75.17	33.96	22.96	61.17	36.92	79.40	48.93	-3.49

Table C.1: Simulation results of the global model estimated with the filtered signals for the actuators on the left rear strut in terms of the *vaf* criterion.

Appendix C: Numerical results of the model identified with filtered data

	TS01	TS02	TS03	TS04	TS05	TS06	TS07	TS08	TS09	TS10	TS11	TS12
A1	40.39	43.26	25.37	17.64	32.02	41.69	34.73	39.07	73.84	60.55	61.79	45.42
A2	63.25	9.66	76.90	82.99	53.14	77.08	55.69	64.03	21.16	25.62	45.44	58.76
A3	61.30	57.24	4.57	89.13	39.33	57.62	80.89	79.84	56.99	32.76	81.97	71.63
A4	67.80	92.30	82.21	57.93	90.00	77.90	86.61	59.14	54.09	47.87	62.12	89.32
A5	94.98	83.36	78.70	76.91	71.55	91.38	91.16	86.09	62.66	0.14	68.19	89.17
A6	84.67	78.04	49.97	30.74	58.58	75.47	21.69	15.59	50.17	30.24	45.13	51.79
A7	69.02	86.13	85.60	53.91	90.11	91.91	53.49	56.82	28.97	19.91	60.44	59.65
A8	62.71	85.02	90.10	-6.56	87.25	88.04	74.75	75.57	26.69	73.07	38.59	89.83
A9	40.72	21.45	42.95	3.41	19.52	45.91	48.14	34.76	46.85	81.31	34.45	47.38
A10	39.12	38.92	38.63	14.17	27.93	55.95	35.08	24.98	75.08	-15.76	56.48	59.28
A11	46.59	58.20	-24.97	67.78	54.58	77.54	-4.83	27.47	15.69	12.70	14.11	66.64
A12	0.60	66.36	-18.46	69.42	38.22	-34.33	44.54	23.39	8.42	54.80	63.09	35.92
A13	64.75	64.15	14.77	42.93	34.55	17.24	24.45	23.16	50.06	67.71	59.58	62.02
A14	29.82	53.36	-2.07	46.41	41.18	-0.34	31.43	31.08	37.41	46.31	63.52	31.43
A15	32.61	21.04	52.62	36.46	60.05	47.43	50.40	64.41	44.31	76.24	68.25	29.90
A16	11.74	50.13	74.00	80.24	58.45	58.75	62.15	30.83	54.03	65.56	69.29	67.98
A17	61.22	32.72	76.68	62.00	13.62	80.20	64.18	45.87	9.02	88.82	66.33	86.43
A18	60.16	66.92	53.38	68.15	84.18	52.00	37.22	50.61	80.53	70.98	67.00	55.02

Table C.2: Simulation results of the global model estimated with the filtered signals for the actuators on the right side of the anti-torque plate in terms of the vaf criterion.

	AD01	AD02	AD03	AD04	AD05	AD06	AD07	AD08
A1	52.78	67.62	16.96	47.64	77.25	62.41	69.11	31.18
A2	41.44	76.70	60.80	56.22	79.54	51.00	55.74	57.96
A3	46.05	56.22	6.89	38.50	34.57	56.90	41.53	16.25
A4	46.63	72.34	72.02	54.49	52.48	35.48	35.08	57.28
A5	31.32	38.74	57.51	56.89	58.98	35.82	65.07	77.54
A6	50.03	76.60	38.17	46.81	78.90	71.54	49.81	43.73
A7	15.36	52.80	44.41	45.32	61.73	37.04	58.52	39.73
A8	63.45	23.55	40.34	64.35	51.45	44.05	65.56	47.22
A9	77.48	45.60	74.49	80.94	32.91	71.51	72.35	48.55
A10	42.09	56.46	24.25	44.28	58.28	15.21	60.02	31.31
A11	54.99	-3.29	30.69	68.00	-25.14	18.38	80.29	51.23
A12	16.75	90.12	68.02	26.72	75.03	6.81	64.66	57.46
A13	94.22	1.61	19.68	87.28	-27.79	88.60	34.43	41.13
A14	29.37	19.30	51.69	17.84	6.99	36.87	0.20	62.10
A15	29.01	23.65	16.72	30.21	31.38	4.92	39.84	21.11
A16	44.77	45.58	19.67	46.12	81.12	76.29	62.30	23.29
A17	96.47	43.89	16.86	73.31	57.70	84.08	60.16	-9.02
A18	11.67	89.28	61.07	42.29	66.17	-4.26	41.39	57.74

Table C.3: Simulation results of the global model identified with the filtered signals for the actuators on the right rear strut in terms of the vaf criterion.

	TD01	TD02	TD03	TD04	TD05	TD06	TD07	TD08	TD09	TD10	TD11	TD12
A1	65.03	47.03	1.13	5.40	40.81	43.66	44.41	68.88	61.01	60.90	9.63	39.74
A2	74.95	57.46	43.90	46.50	47.56	43.31	50.04	35.15	72.99	48.08	3.98	19.86
A3	46.14	49.80	76.23	22.50	52.34	75.24	64.33	79.20	67.90	75.96	50.10	60.64
A4	40.09	22.70	39.79	56.34	50.93	44.23	38.91	32.93	5.38	13.96	53.35	53.04
A5	45.45	50.34	85.45	69.91	81.37	82.72	66.65	70.60	9.35	49.78	34.43	63.75
A6	45.35	9.23	70.60	48.16	46.24	39.51	40.18	36.28	6.52	48.87	4.99	-13.36
A7	54.31	19.20	59.91	51.47	67.75	36.54	59.97	37.27	82.31	48.33	74.30	72.74
A8	54.53	28.65	37.72	27.13	46.34	46.80	40.88	45.79	28.15	82.12	28.85	5.92
A9	34.86	58.25	59.68	42.90	58.90	69.50	60.47	60.58	70.25	82.09	74.69	69.01
A10	45.46	43.34	12.97	13.81	26.07	14.33	11.06	12.70	66.34	16.57	59.48	11.21
A11	67.89	63.53	81.33	74.76	66.19	79.76	73.81	84.17	20.27	80.89	26.95	62.67
A12	26.76	51.80	28.50	14.22	61.81	24.75	61.63	52.92	63.24	56.81	81.40	92.29
A13	59.65	68.56	74.46	92.50	84.42	69.68	70.99	26.21	92.55	9.17	25.92	72.34
A14	58.40	62.62	9.06	73.42	29.01	24.72	-5.14	7.58	61.96	79.38	93.12	22.69
A15	36.23	48.42	78.12	87.37	89.78	87.63	22.12	44.82	38.74	-0.02	54.66	79.57
A16	9.98	14.25	76.87	45.03	74.92	71.74	89.51	93.37	53.08	-12.57	72.33	76.40
A17	38.91	59.65	84.57	34.49	64.86	76.88	81.43	75.20	35.40	77.48	35.73	67.20
A18	71.57	62.88	48.11	16.27	30.52	64.62	20.56	20.15	58.11	71.32	20.67	62.20

Table C.4: Simulation results of the global model identified with the filtered signals for the actuators on the right side of the anti-torque plate in terms of the *vaf* criterion.

Bibliography

- [1] B. Moaveni A. Khaki-Sedigh. *Control Configuration Selection for Multivariable Plants*. Springer, 2000.
- [2] Jaganath Chandrasekar Dannis S. Bernstein Perets P. Friedman Dan Patt, Li Liu. Higher harmonic control algorithm for helicopter vibration reduction revisited. 2005.
- [3] P. Jänker F. Hermle F. Hoffman, R. Maier. Helicopter interior noise reduction by using active gearbox struts. May 2006.
- [4] Terry Ford. Vibrations in helicopters - reduction and monitoring. *Aircraft engineering and aerospace technology*, 1997.
- [5] L.R.J. Haverkamp. State space identification: theory and practice, 2001.
- [6] I. Lyndon J. T. Pearson, R.M. Goodall. Active control of helicopter vibration. *Computing & control engineering journal*, Decembre 1994.
- [7] Ram JanakiRam The Boeing Company Marty Johnson Virginia Tech Dino J. Rossetti Lord Corporation James O'Connell, Gopal Mathur. Helicopter cabin noise reduction using active structural acoustic control.
- [8] Tohru Katayama. *Subspace Methods for System Identification*. Springer, 2005.
- [9] Lennart Ljung. *System Identification Toolbox: User's guide*, 2013.
- [10] Roberto Mura Marco Lovera. Baseline vibration attenuation in helicopters: robust mimo-hhc control.
- [11] Khanh Q. Nguyen. *Higher Harmonic Control Analysis for Vibration Reduction of Helicopter Rotor Systems*.
- [12] Luigi Piroddi. Active noise control and vibratio control. University Lecture, 2012/2013.

BIBLIOGRAPHY

- [13] Marco Lovera Roberto Mura, Amir Masoud Ghalamzan Esfahani. Robust harmonic control for helicopter vibration attenuation.
- [14] Miroslav Jovanovic Slobodan Stupar, Aleksandar Simonovic. Measurement and analysis of vibrations on the helicopter structure in order to detect defects of operating elements.
- [15] Furong Gao Tao Liu. *Industrial Process Identification and Control Design*. Springer, 2012.
- [16] William A. Welsh Charles A. Yoerkie Jr. Douglas G. MacMartin Mark W. Davis Thomas, A. Millott. Flight test of active gear-mesg noise control on the s-76 aircraft. 1998.
- [17] E. Vigoni G.L. Ghiringhelli W. Corbetta, A. Toso. Friendcopter internal report: Set-up of the A109 mock-up for vibration and acoustic tests, March 2005.